Impact of Fluids Distribution System on Bubble Column Hydrodynamics

Jacob Mach Marial

A dissertation submitted in partial fulfilment of
the requirements for the degree of
Doctor of Philosophy
in
Chemical Engineering

Department of Chemical & Biological Engineering
Faculty of Engineering
University of Ottawa

ABSTRACT

The performance of ebullated bed hydroprocessors depends on the fluids distribution system and liquid recycle pan. Given that bubbles do not readily coalesce in the bed, the original bubble size distribution generated at the bubble cap distributor likely impacts buoyancy-based phase separation at the recycle pan. Gas entrained in the liquid recycle increases bed gas holdup at the expense of liquid holdup and product yield. The aim of this work was to investigate the impact of gas-liquid distribution system on resulting bubble properties and dynamics and incorporate a distributor sub-model into an existing fluid dynamics model of the industrial hydroprocessor.

The size of initial bubbles formed in the plenum chamber was found to have negligible impact on phase holdups above the distributor. However, resulting bubble properties were found to depend on distributor geometry, distributor power dissipation and gas-liquid velocity ratio. In addition, a new set of scaling laws for gas-liquid distributors, based on dimensional analysis and similitude, was proposed. Geometric scaling was based on matching distributor fractional open area and ratios of critical dimensions. Dynamic similarity was based on matching three dimensionless groups and bubble coalescence behaviour. A bubble size distribution model was then developed. Both pressure and distributor were found to have an impact on individual bubble drag coefficients, as they both altered bubble size distribution. A novel drag model was thus also developed at industrially relevant conditions.

Finally, a new gas-liquid distributor sub-model, including bubble size distribution and drag models previously developed, was incorporated into an overall fluid dynamics model of the hydroprocessor. The bubble size distribution model was also coupled with existing gas-liquid separation sub-model to better predict recycled gas and liquid fractions. A sensitivity analysis performed with the overall model revealed distributor configurations with potential of improving the processing capacity of the hydroprocessor.

SOMMAIRE

Les performances des hydroprocesseurs à lit fluidisé dépendent du système de distribution des fluides et de la coupe de recyclage du liquide. Etant donné que les bulles ne coalescent pas facilement dans le lit, la distribution de taille de bulle d'origine générée au niveau des tuyères du distributeur a probablement un impact sur la séparation de phase basée sur la flottabilité au niveau de la coupe de recyclage. Le gaz entraîné dans le recyclage de liquide augmente la rétention de gaz du lit aux dépens de la rétention de liquide et du rendement du produit. Le but de ce travail était d'étudier l'impact du système de distribution gaz-liquide sur les propriétés et la dynamique des bulles résultantes et d'incorporer un sous-modèle de distributeur dans un modèle de dynamique des fluides d'un hydroprocesseur industriel.

On a constaté que la taille des bulles initiales formées dans le plénum avait un impact négligeable sur les rétentions de phases au-dessus du distributeur. Cependant, les propriétés des bulles résultantes se sont avérées dépendre de la géométrie du distributeur, de la dissipation de puissance du distributeur et du rapport de vitesse gaz-liquide. De plus, un nouvel ensemble de lois d'échelle pour les distributeurs gaz-liquide, basé sur l'analyse dimensionnelle et la similitude, a été proposé. La mise à l'échelle géométrique était basée sur la correspondance de la surface ouverte fractionnaire du distributeur et des ratios des dimensions critiques. La similarité dynamique était basée sur l'appariement de trois groupes sans dimension et le comportement de coalescence des bulles. Un modèle de distribution de la taille des bulles a ensuite été développé. On a constaté que la pression et la géométrie distributeur avaient un impact sur les coefficients de traînée des bulles individuelles, car ils modifiaient tous les deux la distribution de la taille des bulles. Un nouveau modèle de traînée a donc également été développé dans des conditions industrielles pertinentes.

Enfin, un nouveau sous-modèle de distributeur gaz-liquide, comprenant la distribution de la taille des bulles et les modèles de traînée précédemment développés, a été incorporé dans un modèle global de dynamique des fluides de l'hydroprocesseur. Le modèle de distribution de la taille des bulles a également été couplé au sous-modèle existant de séparation gaz-liquide pour mieux prédire les fractions de gaz et de liquide recyclés. Une analyse de sensibilité réalisée avec le modèle global a révélé des configurations de distributeur avec un potentiel d'amélioration de la capacité de production de l'hydroprocesseur.

STATEMENT OF CONTRIBUTIONS

I declare that I am the sole author of this document. I have conducted the experiments, performed data analysis and prepared the resulting manuscripts for publication. I also wrote the Python code for simulating the fluid dynamics of the LC-Fining Unit.

My supervisor, Dr. Arturo Macchi, collaborators from Dalhousie University, Dr. Adam Donaldson and Dr. Jan Haelssig, and collaborators from Syncrude Canada Ltd., Craig McKnight, Dr. John Adjaye and Dr. Jason Wiens, provided continual guidance and/or contributed with editorial comments and corrections.

Experiments related to the perforated plate gas-liquid distributor in chapter 2 were performed by Valois Parisien; he is a co-author to the paper in chapter 2.

ACKNOWLEDGEMENTS

I would like to thank my supervisor, Dr. Arturo Macchi, for giving me the opportunity to work on this project and for his support during my studies.

I would also like to thank Syncrude Canada Ltd., Natural Sciences and Engineering Research Council, and Ontario's Ministry of Colleges and Universities for funding this project and providing me with financial support. I would also like to acknowledge the help of Dr. Graeme Norval and Dr. Jules Thibault in writing reference letters for the scholarship applications.

I am also greatly indebted to the technical staff, Franco Ziroldo, James McDermaid and Gérard Nina, for their assistance with the construction and installation of bubble cap distributors as well as setup of the data acquisition systems.

Last but not least, I would like to thank World University Service of Canada and the University of Toronto for sponsoring my post-secondary studies and relocation to Canada. This would not be possible without their initial support.

CONTENTS

LIST OF FIGURES

LIST OF TABLES

1

INTRODUCTION

1.1 UPGRADING OF NON-CONVENTIONAL CRUDE OIL

Non-conventional crude oil, such as oil sands bitumen, is distinguishable from conventional crude oil by its higher viscosity, lower hydrogen to carbon ratio, and higher levels of impurities (e.g., sulphur, nitrogen, and heavy metals). To enable pipeline transport and subsequent refining, it must be upgraded to lower the viscosity and remove the impurities. There are numerous upgrading technologies and processes, some of which are discussed in Rana et al. [1] and Sahu et al. [2] However, Figure 1.1 shows an upgrading process for oil sands bitumen at Syncrude Canada Ltd. The process begins with the extraction of bitumen from recovered oil sands in froth floatation tanks. The oil sands are crushed and conveyed into the tanks, where heavy materials, such as clay and sand, settle to the bottom, and lighter materials, including bitumen, rise to the surface as a froth. The froth is skimmed off the surface and topped with a diluent to lower the viscosity. The resulting mixture is distilled at atmospheric pressure to produce virgin light gas oil (LGO) and atmospheric tower bottoms (ATB). A fraction of the ATB is then distilled at vacuum pressures to produce light gas oil, heavy gas oil (HGO) and vacuum tower bottoms (VTB). The remaining ATB and VTB is split between fluid cokers and LC-Fining hydroprocessors. Fluid cokers attempt to increase the hydrogen to carbon ratio by rejecting excess carbon, while the LC-Fining units achieve the same goal by thermal cracking and hydrogenation. The products from the distillation units, fluid cokers, and the LC-Fining units are hydrotreated in fixed bed reactors and blended to produce synthetic crude oil (Syncrude sweet blend), which is then transported to the refinery for final processing and transformation.

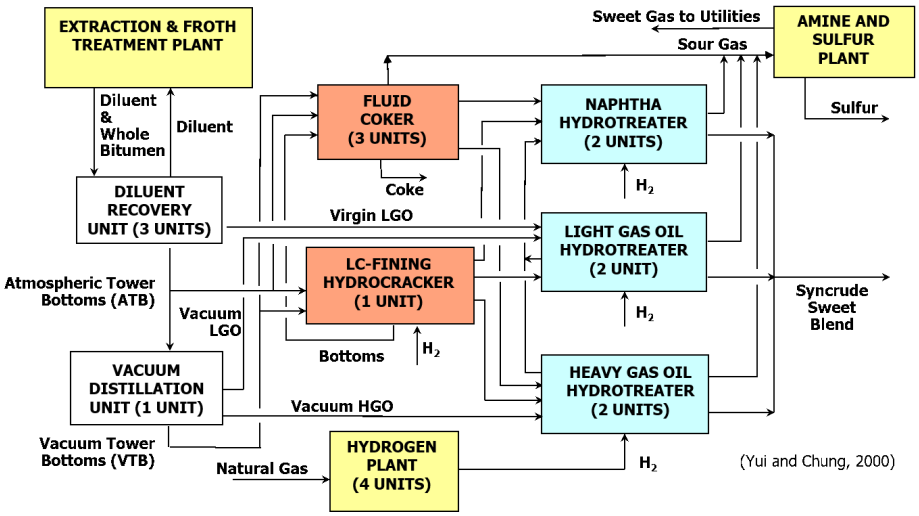

Figure 1.1: Block process diagram of bitumen upgrading at Syncrude Canada Ltd.[3,4]

1.2 LC-FINING UNIT

A schematic of the LC-Fining unit is shown in Figure 1.2. Fresh hydrogen and bitumen residue are separately heated, combined in static mixers and injected into the plenum chamber using a ring-shroud distributor. The fresh feed mixes with internally recycled fluids before passing through the bubble cap risers on the grid. In the bed, liquid hydrocarbons are thermally cracked and hydrogenated in the presence of a solid catalyst. A fraction of the liquid is separated from the gas and recycled back to the plenum via the recycle line to keep the bed fluidized and increase liquid residence time and conversion. The rest of the fluids leave the unit as an effluent for further processing.

The LC-Fining unit processes a mixture of atmospheric and vacuum residue at elevated pressures ($\sim$ 11.7 MPa) and temperatures ($\sim$ 440 °C). There is a need to increase the fraction of vacuum residue in the feed to approach design conditions. Past studies have thus considered the effect of viscosity increase, due to greater vacuum residue fraction, on bed fluid dynamics and gas-liquid separation at the recycle pan. Pjontek et al.[5] observed greater gas recirculation and bed gas holdups with an increase in liquid viscosity. Under similar conditions, Parisien et al.[6] found that over 90% of the bubbles generated with perforated plate distributor had chord lengths less than 1 mm.

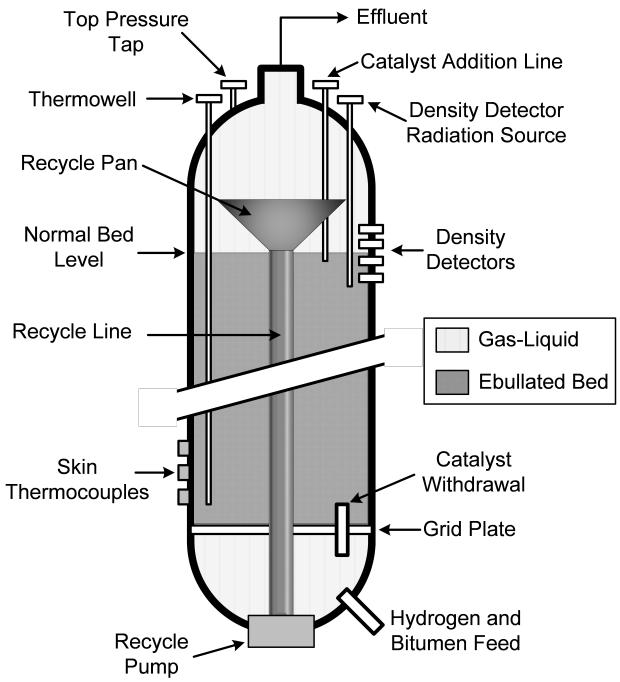

Figure 1.2: Schematic of the LC-Fining unit.[5]

Bubbles belonging to that size range are at the border of Stokes and intermediate flow regimes. As a result, relatively small increases in liquid viscosity can render gas-liquid separation more difficult and promote greater gas entrainment in the liquid recycle – as observed in Pjontek et al.[5] This implies that solely employing buoyancy-based gas-liquid separation processes may not be optimally effective. The original bubble size distribution generated at the grid likely impacts phase separation at the recycle pan since bubbles do not readily coalesce in the bed.[7] Gas entrained in the liquid recycle, as a result of sub-optimal separation at the recycle pan, increases bed gas holdup at the expense of liquid holdup and product yield.[8]

1.3 PLENUM CONDITIONS AND GRID DYNAMICS

Figure 1.3 shows a schematic of the plenum chamber and the bubble cap grid. Figure 1.4 shows the picture and schematic of one bubble cap element. During the start up of the unit, the gas-liquid mixture flows past the tails of the bubble cap risers since the pressure drop through the risers is

greater than the pressure drop through the rest of the plenum. Eventually, the gas-liquid mixture stops at the bottom of the plate, and bubbles begin to accumulate and coalesce at the solid surface. As a result, a gas pocket is formed below the plate. The size of the pocket grows over time until a sufficient fraction of the vertical riser slit is exposed to gas entry from the pocket. The size of the exposed slit is dictated by a balance between the pressure drop of the gas entering through the exposed slit area and that of the gas-liquid mixture entering through the remaining open area of the riser. This ensures both phases enter the riser at the same pressure. At steady state and when there is no swirl in the plenum, the free surface formed is horizontal (dotted lines in Figure 1.3), resulting in uniform distribution of the fluids into the bed.

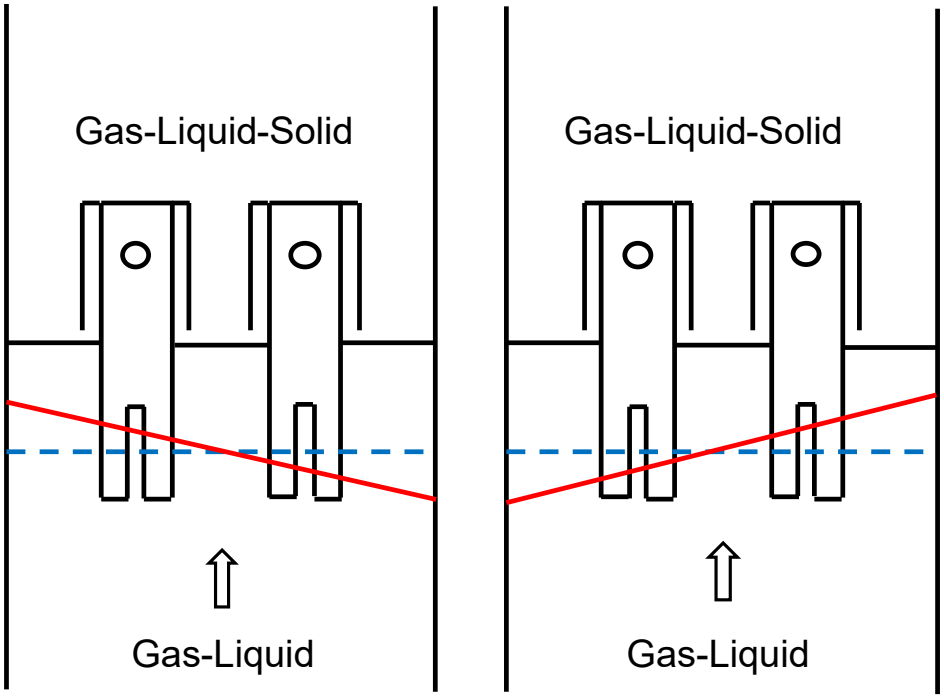

Figure 1.3: Schematic of plenum chamber and bubble cap grid.

In reality, the liquid recycle pump positioned at the bottom of the plenum induces swirl, resulting in a tilted free surface (slanting lines in Figure 1.3). Due to the tilt, risers at the centre of the plenum have greater exposed slit areas than risers closer to the plenum walls. This results in non-uniform radial distribution of the fluids into the bed. To rectify this, Song et al.[9] proposed the use of lateral opening (s) that are strategically sized and placed above the vertical riser slits in order to ideally

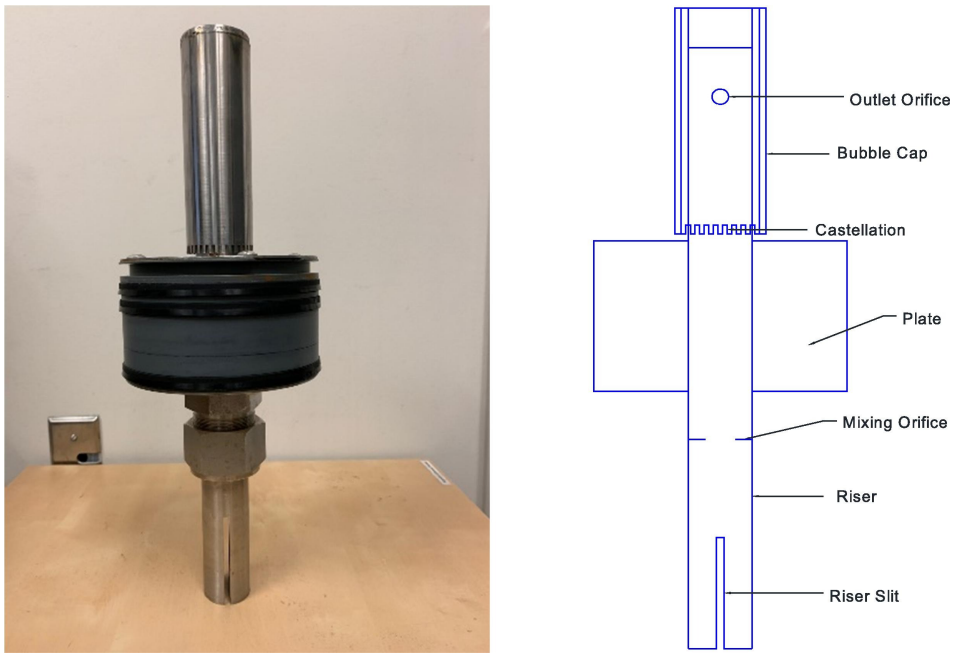

Figure 1.4: Picture and schematic of one bubble cap element

position the inclined free surface above the slit, but below the opening (s). The design requires knowledge of the steady-state free surface position and robustness towards process dynamics (e.g., adjustment in recycle pump speed during catalyst addition and withdrawal), which is not accurately known.

As a result, the impact of a free surface tilt and ensuing gas and liquid flow rates in an individual bubble cap on the bubble properties exiting the grid is not clearly known. Moreover, smaller bubbles entering the bubble cap along with the liquid stream may readily coalesce with the gas entering from the pocket and/or further split due to increased fluids velocities inside the risers. Lastly, the internal geometry of the bubble cap itself may influence the resulting bubble properties. In any case, this gas-liquid mixture with its morphology ultimately flows through the outlet orifices of the bubble cap, creating the final bubble size distribution entering the bed. In turbulent static mixers, the inlet bubble properties are typically not considered while the outlet bubble Sauter mean diameter is modelled as a fraction of the maximum stable diameter, which is deemed proportional to the energy

dissipation rate to the power of -0.4 according to theory on isotropic turbulent bubble breakup.[10–12]

Previous studies on bubble columns and three phase fluidized beds utilized single phase gas injectors,[13–21] which are primarily bubble formation devices. In contrast, two phase gas-liquid distributors such as the bubble cap grid in the LC-Fining unit promote simultaneous bubble breakage and coalescence. Ouyang and Tatterson[22] studied air-water and air-water-solid flows through bubble cap distributor and static mixers, measuring distributor pressure drops and resulting phase holdups. The bubble cap distributor was determined to be better than static mixers due to its higher ratio of gas holdup to pressure drop. Other complementary works[23–26] investigated gas-liquid flow through orifices of different sizes and geometries, measuring pressure drops and, in some cases, gas holdup.

Pjontek et al.[7] measured local bubble characteristics in the freeboard, including gas holdups, bubble rise velocities and chord lengths, using a monofibre optical probe capable of withstanding elevated pressures. Fluidized bed and freeboard measurements demonstrated that flow through the bed of particles enhanced bubble breakage for a water (bubble coalescing) system but had a negligible impact with an added surfactant (0.5 wt. % ethanol). Thus, for the aqueous ethanol solution, local and global holdups in the freeboard region were similar to data obtained in the bubble column at matching operating conditions. These results informed the decision to investigate the impact of fluids distribution system in a bubble column, which happens to be desirable as it minimizes the risk of damaging the optical probe from the impact of rogue particles.

1.4 FLUID DYNAMICS SCALING OF THE LC-FINING UNIT

Previous research on the fluid dynamics scaling of the LC-Fining unit focused on the bed region. Safoniuk et al.[27] proposed a scaling approach based on a cold flow unit, relaxing certain geometrical parameters and matching five dimensionless groups (eqs. 1.1 – 1.5). Freeboard gas holdups

measured in Safoniuk's cold flow unit were found to be significantly lower than those measured in the industrial unit at matching dimensionless groups.[8] The discrepancy was attributed to a number of potential issues including gas entrainment in the liquid recycle, inaccurate measurement of physical properties and holdups in the industrial unit, and/or missing dimensionless groups.

$$Mo = \frac{g\left(\rho_l - \rho_g\right)\mu_l^4}{\rho_l^2 \sigma^3} \tag{1.1}$$

$$Eo = \frac{g\left(\rho_l - \rho_g\right)d_p^2}{\sigma} \tag{1.2}$$

$$Re_{l-s} = \frac{\rho_l U_l d_p}{\mu_l} \tag{1.3}$$

$$\beta_d = \frac{\rho_p}{\rho_l} \tag{1.4}$$

$$\beta_U = \frac{U_g}{U_l} \tag{1.5}$$

Macchi et al.[28] investigated the effect of liquid composition on phase holdups in a gas-liquid-solid fluidized bed. They reported greater gas holdups in multicomponent liquids than in single component liquids due to bubble coalescence inhibition by the surface active compounds in the former. Macchi et al.[29] also investigated the effect of gas density on phase holdups in bubble column and gas-liquid-solid fluidized bed. They reported higher gas holdups for denser gases in both experimental units. These two works demonstrated that the scaling of industrial fluid dynamics must also consider bubble coalescence behavior and enhanced bubble breakage at elevated pressures.

Pjontek et al.[5] later proposed a new set of scaling laws, incorporating previous findings in Macchi et al.[28,29] The new scaling laws were also based on dimensional analysis and similitude, and a new cold flow unit. The proposed scaling laws required matching of five dimensionless groups (eqs. 1.6 – 1.10) and bubble coalescence behaviour to ensure similitude.

$$Re_{l-s} = \frac{\rho_l U_l d_{sv}}{\mu_l} \tag{1.6}$$

$$Ar_{l-s} = \frac{\rho_l g d_v^3 \left(\rho_p - \rho_l\right)}{\mu_l^2} \tag{1.7}$$

$$\beta_\rho = \frac{\rho_g}{\rho_l} \tag{1.8}$$

$$\beta_d = \frac{\rho_p}{\rho_l} \tag{1.9}$$

$$\beta_U = \frac{U_g}{U_l} \tag{1.10}$$

Although the effects of the gas-liquid distribution system were considered in all these studies,[5,27–29] a detailed dimensional analysis was never performed. A combination of porous pipe and perforated plate, which are geometrically different from the industrial fluids distribution system, were used.

1.5 EFFECT OF PRESSURE ON BUBBLE DRAG

Reduced-order fluid dynamics modeling of the industrial unit relies on empirical correlations for drag coefficient to predict bubble slip velocities and freeboard gas holdups. Drag coefficient models are also necessary to close momentum balance equations in Multiphase Computational Fluid Dynamics (MCFD). In literature, drag coefficient models for dense bubbly flows, which are often encountered in industrial applications, are extended from single bubble drag models using a swarm correction factor. The single bubble drag coefficient is reported to be dependent on Reynolds number, Eötvös number and level of interfacial contamination.[30] However, terminal rise velocities predicted with various single bubble drag models show significant discrepancies among themselves, due to differing levels of interfacial contamination and initial bubble detachment conditions.[31]

The swarm correction factor is reported to be a function of gas holdup raised to some coefficient.[32–34] Similar to single bubble drag models, swarm correction models also show significant discrepancies among themselves. Moreover, contradicting results have been reported for the de-

pendence of swarm correction factor on gas holdup. One group of researchers[32,34,35] reported an increase in the correction factor with gas holdup, attributing the dependence to the hindrance effect of the swarm. A second group of researchers[36,37] reported reduction in swarm correction factor with gas holdup, suggesting that the effect of the swarm is assistive. Simonnet et al.[33] reported both hindering and assistive effects and determined a critical gas holdup of $\sim$ 15%, above which the assistive effect dominates and below which the hindrance effect dominates. They attributed the hindrance effect to bubble induced turbulence and assistive effect to the aspiration of smaller bubbles into the wakes of leading larger bubbles. Below the critical gas holdup, the population of larger bubbles was considered negligible, and becomes significant above the critical gas holdup due to enhanced bubble coalescence.

Except for McClure et al.[36] and Rabha and Buwa,[37] the above studies dealt with mono-disperse bubble size distributions. Moreover, all these studies were conducted at atmospheric pressure and thus do not account for the effect of pressure on bubble drag. Lane et al.[38] investigated the effect of bubble swarm on drag coefficient at atmospheric pressure and elevated pressure of 6.5 MPa. At atmospheric pressure, their rise velocities were relatively well predicted by the single bubble drag model of Tomiyama et al.[30] and the swarm correction model of Lockett and Kirkpatrick.[32] At 6.5 MPa, they argued that the swarm correction factor was not needed as the single bubble drag model of Tomiyama et al.[31] provided the best fit to their experimental bubble rise velocities. This implies that the swarm correction factor decreases with pressure and there exists a critical pressure beyond which the swarm has no effect. It is not clear why the swarm correction factor would decrease with pressure and why it would eventually become zero, even at elevated gas holdups. More experiments were needed to shed light on the underlying mechanism and to quantify the effect of pressure on bubble drag without resorting to existing single bubble and swarm correction models that show large discrepancies among themselves.

1.6 FLUID DYNAMICS MODELING OF THE LC-FINING UNIT

Lane et al.[39] developed an MCFD model to simulate the gas-liquid separation efficiency of the first generation recycle pan (recycle cup). Previous studies[8] had suggested presence of effervescent foam in the freeboard region. A bubble-bubble packing limiter was implemented to investigate the effect of foam generation. Significant reductions in gas separation efficiency were reported when disengaged gas exceeded the packing limiter. A sensitivity analysis of gas separation to fluids flowrates, freeboard gas holdup, liquid recycle fraction and bubble diameter revealed that the liquid residence time is sufficient to estimate the separation efficiency.

Lane et al.[40] later leveraged previously developed separation model[39] to investigate the performance of the second generation recycle pan (flow through pan). The flow through pan performed slightly better than the recycle cup. Although both pans exhibited significant liquid short-circuiting, the flow through pan reduced the amount of liquid with low residence time, resulting in better separation of larger bubbles and slightly better overall performance.

Lane et al.[41] incorporated bed[5] and recycle pan sub-models[39,40] into an overall model of the LC-Fining unit. Due to the lack of reliable bubble size estimate at the time, they iteratively manipulated the mean bubble size to match commercial freeboard gas holdups and gas separation efficiency. This resulted in a model that is quite suitable for the particular operating conditions and reactor geometry, but that may not be extensible to other ebullated bed hydroprocessors. Other studies[42–44] that attempted to model the overall fluid dynamics faced similar challenges.

A distributor sub-model with the ability to predict resulting bubble size and rise velocity distributions is necessary to decouple reaction kinetics and phase equilibria from fluid dynamics. Such a sub-model could also eliminate the reliance on commercial operating data for tuning, and thus enable the extension of the overall model to other operating conditions and reactor geometries.

This sub-model could also be explicitly coupled with the existing recycle pan sub-model to provide better estimates of recycle flow rates. Once the distributor sub-model has been developed, verified, and integrated into the overall fluid dynamics model, reaction kinetics and phase equilibria can be explicitly re-coupled with fluid dynamics to provide a comprehensive tool for design, training, and simulating the effects of operating conditions on reactor performance.

1.7 RESEARCH OBJECTIVES

The primary objective of this project was to investigate the impact of fluids distribution system on bubble dynamics and properties as well as incorporate the resulting fluids distribution sub-model into the overall fluid dynamics model of the industrial unit. More specific objectives are summarized below.

1. Investigate the impact of plenum conditions and gas-liquid distributor on bubble column hydrodynamics.
2. Develop and experimentally validate scaling laws for gas-liquid distributors.
3. Determine the effect of pressure on the drag coefficient of individual bubbles in a contaminated polydisperse swarm.
4. Explicitly incorporate the impact of fluids distribution system into the overall fluid dynamics model of the industrial unit.

1.8 BUBBLE CHARACTERIZATION TECHNIQUES

Bubble properties such as the overall gas holdup, bubble size and rise velocity were measured using a differential pressure transducer and a custom monofibre optical probe. The differential pressure transducer was used to measure the dynamic pressure loss along the vertical axis of the

experimental column. The slope of this axial dynamic pressure loss can be related to the overall gas holdup as shown in equation 1.11, which is derived from Bernouli's equation assuming negligible wall frictional losses and no phase acceleration.

$$\varepsilon_g = \frac{-dP/dz}{g\left(\rho_l - \rho_g\right)} \tag{1.11}$$

The optical probe was used to measure both bubble size and rise velocity. There are three generations of monofibre optical probes: 1C, 3C and 1C–3C. Pictures of 1C and 3C probe are shown in Figure 1.5. 1C probes tend to be less precise but better suited to measurement of bubbles with diameters less than 0.5 mm. On the other hand, 3C probes are more precise but better suited to the measurement of larger bubbles. 1C–3C probe, which was used in this work, combines the benefits of 1C and 3C tip geometries.

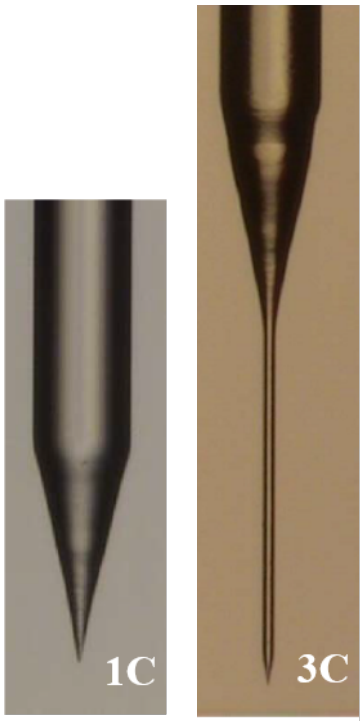

(a) (b)

Figure 1.5: Pictures of (a) 1C and (b) 3C monofibre optical probes.[7]

The probe relies on changes in refractive index at its tip to distinguish the bubble phase from the liquid phase. Given that the gas has a lower refractive index than the liquid, more light is internally reflected when the tip is occupied by the bubble. The internally reflected light is converted to a voltage signal by an optoelectronic module. A lower and upper voltage threshold can be set to aid data analysis (see Figure 1.6). The time it takes for the signal to transition from the lower to the upper threshold is called the signal rise time and it is inversely proportional to bubble rise velocity (see equation 1.12). The time it takes for the signal to transition to and stay above the upper threshold is known as the bubble residence time and it is directly proportional to the bubble size (see equation 1.13).

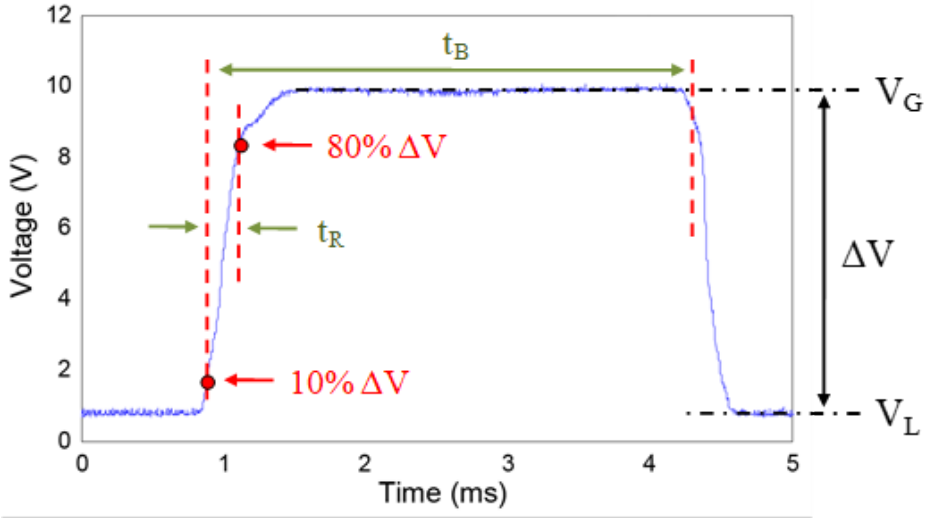

Figure 1.6: Representation of typical optical probe signal.[7]

$$u_{b,i} = \frac{L_s}{t_R} \tag{1.12}$$

$$c_{b,i} = u_{b,i}.t_B \tag{1.13}$$

1.9 OVERVIEW

As mentioned, the main goal of this work was to investigate the impact of fluids distribution system on resulting bubble properties and dynamics and incorporate a distributor sub-model into an existing fluid dynamics model of the industrial hydroprocessor. The performance of industrial ebullated bed hydroprocessors is likely dependent on the fluids distribution system since the final bubble size and rise velocity distribution generated at the distributor can impact gas-liquid separation at the recycle pan. Gas entrained in the liquid recycle, as a result of sub-optimal separation at the recycle pan, increases bed gas holdup at the expense of liquid holdup and product yield.[8]

Chapter 2 deals with the impact of initial bubbles sparged into the plenum, the effect of distributor geometry, and the modeling of resulting mean bubble diameters using Kolmogorov-Hinze theory. Although the gas-liquid distributor can be scaled using Kolmogorov-Hinze theory, it requires prior knowledge of distributor pressure drops and fluids residence times, which can be challenging to accurately predict. In addition, the pressure drops and resulting power dissipations can be unevenly distributed through the distributor, which is an additional challenge to both scaling and experimental modeling. Lastly, Kolmogorov-Hinze theory is based on isotropic turbulence, which may not always be the case, such as for more viscous hydrocarbon feeds.

In chapter 3, an alternate scaling approach using dimensional analysis and similitude is proposed. This approach is not limited to isotropically turbulent flows and the resulting dimensionless groups can be estimated beforehand given phase physical properties, fluids velocities and system parameters. Chapter 4 details the effect of pressure on the drag force acting on a bubble in a contaminated polydisperse swarm. In chapter 5, a gas-liquid distributor sub-model, comprising of bubble size distribution and drag coefficient model, developed in chapter 3 and 4, is incorporated into the overall fluid dynamics model of the industrial unit. The bubble size distribution and drag coefficient models are used to estimate freeboard gas holdups, from which bed gas and

liquid holdups are estimated. The bubble size distribution model is also coupled with the existing gas-liquid separation sub-model to provide better estimates of recycle flow rates.

NOMENCLATURE

ATB	atmospheric tower bottom
Eo	Eötvös number
g	gravitational acceleration, m/s^2
LGO	light gas oil
MCFD	multiphase computational fluid dynamics
Mo	Morton's number
VTB	vacuum tower bottom
Ar_{l-s}	particle-liquid Archimedes number
d_p	particle diameter, m
dP	dynamic pressure drop, Pa
dz	vertical distance between pressure ports, m
L_s	probe sensing length, μm
Re_{l-s}	particle-liquid Reynolds number
t_R	signal rise time, ms
t_B	bubble residence time, ms
U_g	gas superficial density, m/s
U_l	liquid superficial velocity, m/s
β_d	particle-liquid density ratio
β_ρ	gas-liquid density ratio
β_U	gas-liquid velocity ratio
ε_g	overall gas holdup, $m^3_{bubbles}/m^3_{reactor}$

μ_l	liquid viscosity, $Pa.s$
ρ_g	gas density, kgm^{-3}
ρ_l	liquid density, kgm^{-3}
ρ_p	particle density, kgm^{-3}
σ	surface tension, N/m

REFERENCES

[1] Mohan S. Rana, Vicente Sámano, Jorge Ancheyta, and J. A.I. Diaz. A review of recent advances on process technologies for upgrading of heavy oils and residua. *Fuel*, 86(9 SPEC. ISS.):1216–1231, 2007. ISSN 00162361. doi: 10.1016/j.fuel.2006.08.004.

[2] Ramakanta Sahu, Byung Jin Song, Ji Sun Im, Young Pyo Jeon, and Chul Wee Lee. A review of recent advances in catalytic hydrocracking of heavy residues. *J. Ind. Eng. Chem.*, 27:12–24, 2015. ISSN 22345957. doi: 10.1016/j.jiec.2015.01.011.

[3] S. Yui and Keng Chung. Processing oilsands bitumen is syncrude's r & d focus. *Oil and Gas Journal*, 99:46–53, 2001.

[4] Sok Yui. Producing quality synthetic crude oil from canadian oil sands bitumen. *Journal of the Japan Petroleum Institute*, 51(1):1–13, 2008.

[5] Dominic Pjontek, Craig A. McKnight, Jason Wiens, and Arturo Macchi. Ebullated bed fluid dynamics relevant to industrial hydroprocessing. *Chem. Eng. Sci.*, 126:730–744, 2015. ISSN 00092509. doi: 10.1016/j.ces.2015.01.002.

[6] Valois Parisien, Alixia Farrell, Dominic Pjontek, Craig A. McKnight, Jason Wiens, and Arturo Macchi. Bubble swarm characteristics in a bubble column under high gas holdup conditions. *Chem. Eng. Sci.*, 157:88–98, jan 2017. ISSN 00092509. doi: 10.1016/j.ces.2016.04.051.

[7] Dominic Pjontek, Valois Parisien, and Arturo Macchi. Bubble characteristics measured using a monofibre optical probe in a bubble column and freeboard region under high gas holdup conditions. *Chem. Eng. Sci.*, 111:153–169, 2014. ISSN 00092509. doi: 10.1016/j.ces.2014.02.024.

[8] Craig A. McKnight, Larry P. Hackman, John R. Grace, Arturo Macchi, Darwin Kiel, and Jonathan Tyler. Fluid Dynamic Studies in Support of an Industrial Three-Phase Fluidized Bed Hydroprocessor. *Can. J. Chem. Eng.*, 81(3-4):338–350, jun 2008. ISSN 0008-4034. doi: 10.1002/cjce.5450810302.

[9] Steven Xuqi Song, Donald Leroy Kuehne, Abdenour Kemoun, and Bruce Edwards Reynolds. Apparatus and method for hydroconversion, 2016.

[10] J. O. Hinze. Fundamentals of the hydrodynamic mechanism of splitting in dispersion processes. *AIChE J.*, 1(3):289–295, sep 1955. ISSN 15475905. doi: 10.1002/aic.690010303.

[11] Stanley Middleman. Drop Size Distributions Produced by Turbulent Pipe Flow of Immiscible Fluids through a Static Mixer. *Ind. Eng. Chem. Process Des. Dev.*, 13(1):78–83, jan 1974. ISSN 01964305. doi: 10.1021/i260049a015.

[12] Neima Brauner. The prediction of dispersed flows boundaries in liquid-liquid and gas-liquid systems. *Int. J. Multiph. Flow*, 27(5):885–910, may 2001. ISSN 03019322. doi: 10.1016/S0301-9322(00)00056-2.

[13] E. Camarasa, C. Vial, S. Poncin, G. Wild, N. Midoux, and J. Bouillard. Influence of coalescence behaviour of the liquid and of gas sparging on hydrodynamics and bubble characteristics in a bubble column. *Chem. Eng. Process. Process Intensif.*, 38(4-6):329–344, 1999. ISSN 02552701. doi: 10.1016/S0255-2701(99)00024-0.

[14] Bimal Gandhi, Anand Prakash, and Maurice A. Bergougnou. Effects of sparger height and orifice orientation on solids dispersion in a slurry bubble column. *Can. J. Chem. Eng.*, 77(2):383–391, apr 1999. ISSN 00084034. doi: 10.1002/cjce.5450770226.

[15] D. Geldart and J. Baeyens. The design of distributors for gas-fluidized beds. *Powder Technol.*, 42(1):67–78, apr 1985. ISSN 00325910. doi: 10.1016/0032-5910(85)80039-5.

[16] Lu Han and Muthanna H. Al-Dahhan. Gas-liquid mass transfer in a high pressure bubble column reactor with different sparger designs. *Chem. Eng. Sci.*, 62(1-2):131–139, jan 2007. ISSN 00092509. doi: 10.1016/j.ces.2006.08.010.

[17] Anand V. Kulkarni and Jyeshtharaj B. Joshi. Design and selection of sparger for bubble column reactor. Part I: Performance of different spargers. *Chem. Eng. Res. Des.*, 89(10):1972–1985, 2011. ISSN 02638762. doi: 10.1016/j.cherd.2011.01.004.

[18] Anand V. Kulkarni and Jyeshtharaj B. Joshi. Design and selection of sparger for bubble column reactor. Part II: Optimum sparger type and design. *Chem. Eng. Res. Des.*, 89(10):1986–1995, oct 2011. ISSN 02638762. doi: 10.1016/j.cherd.2011.01.014.

[19] Raymond Lau, Wei Shan Beverly Sim, and Rujuan Mo. Effect of gas distributor on hydrodynamics in shallow bubble column reactors. *Can. J. Chem. Eng.*, 87(6):847–854, 2009. ISSN 00084034. doi: 10.1002/cjce.20224.

[20] Fereshteh Rahimpour, Reza Zarghami, and Navid Mostoufi. Effect of distributor on fluidized bed hydrodynamics. *Can. J. Chem. Eng.*, 95(11):2221–2234, 2017. ISSN 1939019X. doi: 10.1002/cjce.22895.

[21] Safa Sharaf, Maria Zednikova, Marek C. Ruzicka, and Barry J. Azzopardi. Global and local hydrodynamics of bubble columns - Effect of gas distributor. *Chem. Eng. J.*, 288:489–504, 2016. ISSN 13858947. doi: 10.1016/j.cej.2015.11.106.

[22] C. J.P. Ouyang and G. B. Tatterson. The Effect of Distributors on Two-Phase and Three-Phase Flows in Vertical Columns. *Chem. Eng. Commun.*, 49(4-6):197–215, 1987. ISSN 15635201. doi: 10.1080/00986448708911803.

[23] Claudio Alimonti, Gioia Falcone, and Oladele Bello. Two-phase flow characteristics in multiple orifice valves. *Exp. Therm. Fluid Sci.*, 34(8):1324–1333, 2010. ISSN 08941777. doi: 10.1016/j.expthermflusci.2010.06.004.

[24] Ammar Zeghloul, Abdelwahid Azzi, Faiza Saidj, Barry J. Azzopardi, and Buddhika Hewakandamby. Interrogating the effect of an orifice on the upward two-phase gas-liquid flow behavior. *Int. J. Multiph. Flow*, 74:96–105, 2015. ISSN 03019322. doi: 10.1016/j.ijmultiphaseflow.2015.04.013.

[25] Ammar Zeghloul, Abdelwahid Azzi, Faiza Saidj, Abdelkader Messilem, and Barry James Azzopardi. Pressure Drop Through Orifices for Single- and Two-Phase Vertically Upward Flow - Implication for Metering. *J. Fluids Eng. Trans. ASME*, 139(3):1–12, 2017. ISSN 1528901X. doi: 10.1115/1.4034758.

[26] Ammar Zeghloul, Abdelwahid Azzi, Abbas Hasan, and Barry James Azzopardi. Behavior and pressure drop of an upwardly two-phase flow through multi-hole orifices. *Proc. Inst. Mech. Eng. Part C J. Mech. Eng. Sci.*, 232(18):3281–3299, 2018. ISSN 20412983. doi: 10.1177/0954406217736081.

[27] Mike Safoniuk, John R. Grace, Larry Hackman, and Craig A. McKnight. Use of dimensional similitude for scale-up of hydrodynamics in three-phase fluidized beds. *Chem. Eng. Sci.*, 54 (21):4961–4966, 1999. ISSN 00092509. doi: 10.1016/S0009-2509(99)00218-3.

[28] Arturo Macchi, Hsiaotao Bi, John R. Grace, Craig A. McKnight, and Larry Hackman. Dimensional hydrodynamic similitude in three-phase fluidized beds. *Chem. Eng. Sci.*, 56(21-22): 6039–6045, 2001. ISSN 00092509. doi: 10.1016/S0009-2509(01)00207-X.

[29] Arturo Macchi, Hsiaotao Bi, John R. Grace, Craig A. McKnight, and Larry Hackman. Effect of Gas Density on the Hydrodynamics of Bubble Columns and Three-Phase Fluidized Beds. *Can. J. Chem. Eng.*, 81(3-4):846–852, jun 2008. ISSN 0008-4034. doi: 10.1002/cjce.5450810368.

[30] Akio Tomiyama, Isao Kataoka, Iztok Zun, and Tadashi Sakaguchi. Drag coefficients of single bubbles under normal and micro gravity conditions. *JSME Int. Journal, Ser. B Fluids Therm. Eng.*, 41(2):472–479, 1998. ISSN 13408054. doi: 10.1299/jsmeb.41.472.

[31] A. Tomiyama, G. P. Celata, S. Hosokawa, and S. Yoshida. Terminal velocity of single bubbles in surface tension force dominant regime. *Int. J. Multiph. Flow*, 28(9):1497–1519, 2002. ISSN 03019322. doi: 10.1016/S0301-9322(02)00032-0.

[32] M. J. Lockett and R. D. Kirkpatrick. Ideal Bubbly Flow and Actual Flow in Bubble Columns. *Trans. Inst. Chem. Eng.*, 53(4 (OCTOBER, 1975)):267–273, 1975.

[33] M. Simonnet, C. Gentric, E. Olmos, and N. Midoux. Experimental determination of the drag coefficient in a swarm of bubbles. *Chem. Eng. Sci.*, 62(3):858–866, 2007. ISSN 00092509. doi: 10.1016/j.ces.2006.10.012.

[34] I. Roghair, Y. M. Lau, N. G. Deen, H. M. Slagter, M. W. Baltussen, M. Van Sint Annaland, and J. A.M. Kuipers. On the drag force of bubbles in bubble swarms at intermediate and high Reynolds numbers. *Chem. Eng. Sci.*, 66(14):3204–3211, 2011. ISSN 00092509. doi: 10.1016/j.ces.2011.02.030.

[35] C. Garnier, M. Lance, and J. L. Marié. Measurement of local flow characteristics in buoyancy-driven bubbly flow at high void fraction. *Exp. Therm. Fluid Sci.*, 26(6-7):811–815, 2002. ISSN 08941777. doi: 10.1016/S0894-1777(02)00198-X.

[36] Dale D. McClure, John M. Kavanagh, David F. Fletcher, and Geoffrey W. Barton. Experimental investigation into the drag volume fraction correction term for gas-liquid bubbly flows. *Chem. Eng. Sci.*, 170:91–97, 2017. ISSN 00092509. doi: 10.1016/j.ces.2016.12.066.

[37] Swapna S. Rabha and Vivek V. Buwa. Experimental investigations of rise behavior of monodispersed/polydispersed bubbly flows in quiescent liquids. *Ind. Eng. Chem. Res.*, 49(21):10615–10626, nov 2010. ISSN 08885885. doi: 10.1021/ie1006454.

[38] C. D. Lane, V. Parisien, A. Macchi, and A. A. Donaldson. Investigation of bubble swarm drag at elevated pressure in a contaminated system. *Chem. Eng. Sci.*, 152:381–391, 2016. ISSN 00092509. doi: 10.1016/j.ces.2016.06.017.

[39] C. D. Lane, C. A. McKnight, J. Wiens, K. Reid, and A. A. Donaldson. Parametric analysis of internal gas separation within an ebullated bed reactor. *Chem. Eng. Res. Des.*, 105:44–54, 2016. ISSN 02638762. doi: 10.1016/j.cherd.2015.10.043.

[40] Chris D. Lane, Arturo Macchi, Craig A. Mcknight, Jason Wiens, and Adam A. Donaldson. Internal Gas-Liquid Separation in Industrial Ebullated Bed Hydroprocessors. *Ind. Eng. Chem. Res.*, 58(40), 2019. ISSN 15205045. doi: 10.1021/acs.iecr.9b02201.

[41] Chris D. Lane, Arturo Macchi, Dominic Pjontek, Craig A. McKnight, Jason Wiens, and Adam A. Donaldson. Modeling the Fluid Dynamics of a Commercial Ebullated Bed Hydroprocessor. *Ind. Eng. Chem. Res.*, 58(39):18387–18396, 2019. ISSN 15205045. doi: 10.1021/acs.iecr.9b02779.

[42] Richard M. Eccles. Residue hydroprocessing using ebullated-bed reactors. *Fuel Process. Technol.*, 35(1-2):21–38, 1993. ISSN 03783820. doi: 10.1016/0378-3820(93)90083-G.

[43] Jean Marc Schweitzer and Stéphane Kressmann. Ebullated bed reactor modeling for residue conversion. *Chem. Eng. Sci.*, 59(22-23):5637–5645, 2004. ISSN 00092509. doi: 10.1016/j.ces.2004.08.018.

[44] Eduard Manek and Juma Haydary. Investigation of the liquid recycle in the reactor cascade of an industrial scale ebullated bed hydrocracking unit. *Chinese J. Chem. Eng.*, 27(2):298–304, 2019. ISSN 10049541. doi: 10.1016/j.cjche.2018.06.023.

2

IMPACT OF PLENUM CONDITIONS AND GAS-LIQUID DISTRIBUTOR ON BUBBLE COLUMN HYDRODYNAMICS

ABSTRACT

In an LC-Fining™ hydroprocessor, the orientation of the free surface in the plenum chamber and the efficiency of the internal gas-liquid separator impact the amounts of the gas and the liquid passing through individual bubble cap risers in the grid. Various gas and liquid flowrates were thus passed through a single bubble cap riser to determine resulting bubble properties. Bubble sizes correlated well with energy dissipation rate and gas-to-liquid velocity ratio to the power of -0.4 and 0.6, respectively, in agreement with theory on the turbulent breakup of dense dispersions. Bubbles were also influenced by the gas-liquid distributor geometry, where the bubble cap produced larger bubbles than a perforated plate. Finally, the size of bubbles sparged in the plenum marginally affected overall gas holdup, suggesting that a bubble cap distributor redesign should be prioritized over upstream gas introduction equipment to optimize the performance of the hydroprocessor.[1]

1 This chapter has been published in Chemical Engineering Science: doi.org/10.1016/j.ces.2019.115296

2.1 INTRODUCTION

The performance (e.g., space-time yield) of industrial ebullated bed hydroprocessors greatly depends on the fluids distribution system and the liquid recycle pan. In an LC-Fining™ unit, the inlet hydrogen and liquid hydrocarbons are heated separately, combined in a static mixer and then fed into the plenum chamber below the grid plate using a perforated ring/shroud distributor assembly. The feed mixes with the recycled fluids before flowing through the risers and bubble caps located in the grid plate. A uniform spatial distribution of fluids into the fluidized bed is essential for proper hydrogenation and to prevent the formation of mesophase and coke, which foul the grid and further hinder the fluids distribution. Moreover, since bubbles do not readily coalesce in the bed, the original bubble size distribution likely impacts phase separation in the recycle pan, and gas entrained with the recycled liquid increases the gas flow through the distribution system resulting in greater bed gas holdups at the expense of the liquid holdup and ultimately product yield.[1]

Upon start-up, the gas-liquid mixture in the plenum chamber primarily flows past the tail of the bubble cap risers since the pressure drop through them is much greater than continuing upwards. The flow stops at the grid and bubbles begin to accumulate and coalesce at the solid surface. As a result, a gas pocket is formed below the grid plate (Fig. 2.1). For the bubble cap geometrical configuration described in Colvert,[2] the size of the pocket grows over time until the pressure drop of the gas entering through the upper portion of the slits on the side of the riser is equal to the pressure drop of the liquid entering through the remaining open area of the riser, thus ensuring both phases enter at the same pressure. At steady-state and under ideal conditions, the free surface formed is horizontal (dotted line in Fig. 2.1), leading to uniform distribution of the fluids into the fluidized bed.

In reality, the free surface is tilted (slanting lines in Fig. 2.1) due to the rotational action of the liquid recycle pump stationed at the bottom of the plenum chamber.[1] The pump applies a fictitious

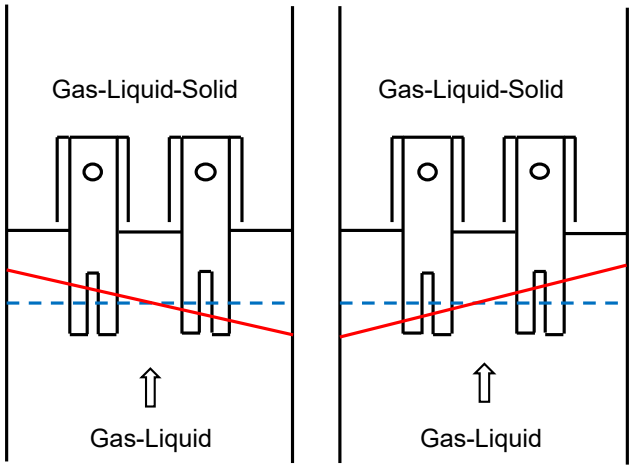

Figure 2.1: Simplified schematic of LC-Fining™ unit's plenum chamber and a bubble cap grid.[2] Fluids are uniformly distributed into the catalyst bed when the plenum liquid level is ideally horizontal (dotted horizontal line). However, the recycle pump causes a tilt in the plenum liquid level (slanted continuous line) which can lead to fluid maldistribution.

centrifugal force on the fluid particles inside the plenum, while the plenum wall applies a counter-acting centripetal force, thus maintaining the fluids in a circular path. The applied centripetal force is a result of pressure increase from the center of the column to the wall. Given that the gas in the pocket is compressible, the radial pressure gradient creates a concave free surface, which results in less open slit area on the risers near the wall. This in turn causes different gas flow rates through the slit, with bubble cap risers near the wall receiving less gas since their openings are smaller. In order to circumvent this problem, Song et al.[3] proposed the use of lateral opening(s) that are strategically sized and placed above the vertical slit in order to ideally position the inclined free surface above the slit but below the opening(s). This design requires knowledge of the steady-state free surface position and robustness towards process dynamics (e.g., adjustment in recycle pump speed during catalyst addition/removal), which are not accurately known.

As a result, the impact of a free surface tilt and ensuing gas and liquid flow rates in an individual bubble cap on the bubble properties exiting the grid is not clearly known. Moreover, smaller bubbles entering the bubble cap along with the liquid stream may readily coalesce with the gas entering from the pocket or further split due to increased fluid velocities inside the risers. Lastly,

the internal geometry of the bubble cap itself may influence the resulting bubble properties. In any case, this gas–liquid mixture with its morphology ultimately flows through the outlet orifices of the bubble cap, creating the final bubble size distribution entering the bed. In turbulent static mixers, the inlet bubble properties are typically not considered while the outlet bubble Sauter mean diameter is modeled as a fraction of the maximum stable diameter, which is theoretically deemed proportional to the energy dissipation rate to the power of -0.4.[4–6]

There have been few studies on the effect of fluid distribution system on the hydrodynamic behavior of bubble columns and three phase fluidized bed reactors.[7–16] Except for Ouyang and Tatterson,[14] the fluid distribution system in this literature is usually a perforated plate, porous plate or porous pipe and with single fluid (gas) flowing. Ouyang and Tatterson measured distributor pressure drop and average gas holdups for air-water and air-water-solids systems flowing through a bubble cap or Koch static mixers. They found the bubble cap to be a better distributor, by comparing the ratio of average gas holdup and distributor pressure drop.

As mentioned, the bubble cap geometry and the horizontal free surface in the plenum ensure each riser receives similar gas and liquid flowrates hence uniform distribution of the fluids. This is not the case for the two-phase flow through each hole of a perforated plate, for example, due to the large phase density difference. Moreover, the power dissipation is relatively large compared to single phase gas spargers and results in relatively smaller bubbles. Further, the outlet of the bubble cap forces the flow to jet radially outwards, sweeping away particles resting on the grid. On the other hand, the bubble cap design is more complex to operate and costly to maintain, which is the case for distributors specifically designed for the co-injection of two fluids.[17,18] In the case of the LC-Fining™ unit, injection of hydrogen and oil mixture into the catalytic bed is necessary for safety since single phase injection of hydrogen could lead to excessive hot spots.

The objective of this study is thus to experimentally investigate the effect of plenum chamber conditions and grid distributor geometry in a bubble column under bubble coalescing and non-coalescing conditions. Given that the efficiency of the liquid recycle pan, the catalyst bed inventory and a free surface tilt can interdependently cause different amounts of gas and liquid to go through each bubble cap riser, various gas and liquid flow rates were passed through a single bubble cap plate (SBC) to determine the resulting impact on bubble properties. In addition, gas feed is sparged into the plenum chamber using a sintered porous pipe or a manifold of perforated pipes to investigate the effect of initial bubble size. Finally, the resulting bubble sizes exiting the bubble cap are correlated to the energy dissipation rate, considering bubble breakup under turbulent flow conditions and elevated dispersed phase holdups.

2.2 MATERIALS AND METHODS

2.2.1 *Experimental Setup*

Experiments were conducted in a clear polyvinyl chloride column with an internal diameter of 0.152 m and a height of 2.7 m (Fig. 2.2). Compressed air was delivered to the column through a sintered porous pipe (10 μm in diameter pores) or a manifold of perforated pipes (26 holes of 0.8 mm in diameter). The resulting gas-liquid mixture then flowed through a bubble cap distributor (Fig. 2.3) positioned approximately mid-way through the column. The mixing orifice volume is 8.42 cm^3 and outlet orifices volume is 1.43 cm^3; the sum is used to calculate the energy dissipation rate in the bubble cap. In an alternate set-up, the gas-liquid mixture generated by the sintered porous pipe was passed through a perforated plate (Fig. 2.4) with 16 to 80 holes of 4 mm in diameter in order to achieve different energy dissipation rates. Table 2.1 summarizes the three experimental configurations. The column was connected at the top to an overflow tank where the gas could disengage from the liquid. The residual gas-liquid mixture was then directed to a storage tank for secondary gas removal before the liquid was returned to the bottom of the column.

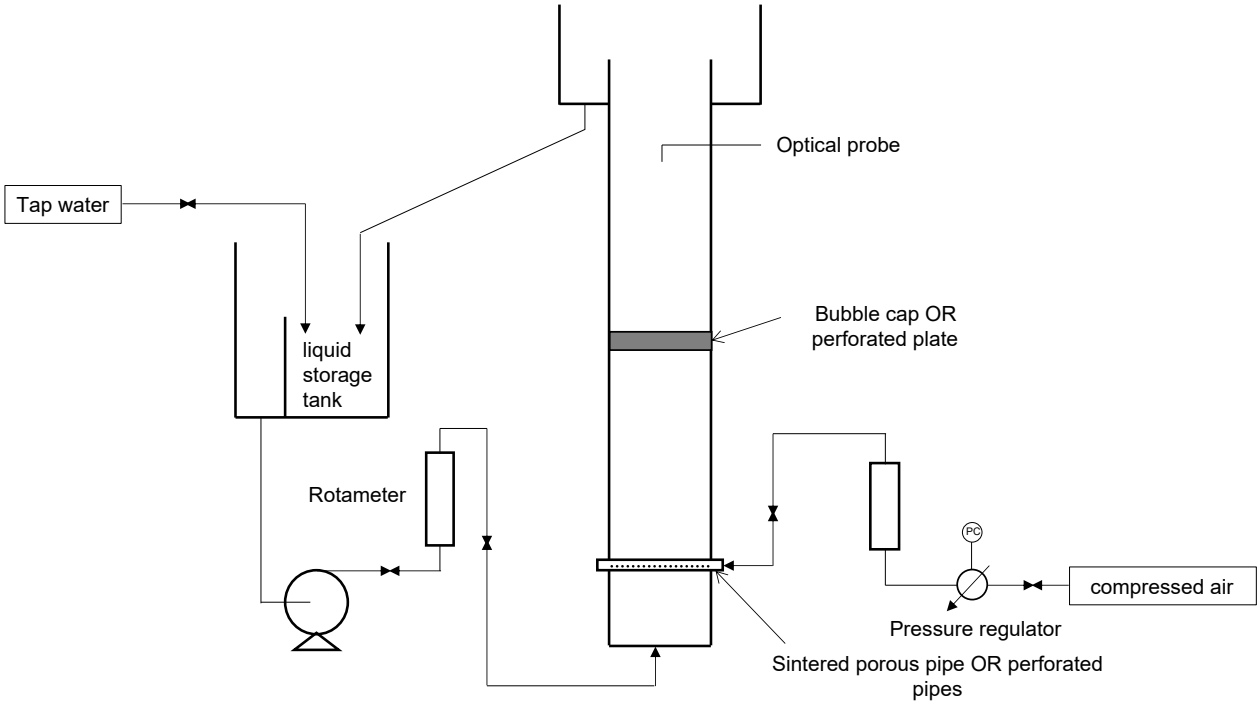

Figure 2.2: Simplified schematic of the experimental system

Table 2.1: Experimental set-ups

Setup	Sparger	Gas-liquid distributor
1	Sintered porous pipe	Bubble cap plate
2	Perforated pipes	Bubble cap plate
3	Sintered porous pipe	Perforated plate

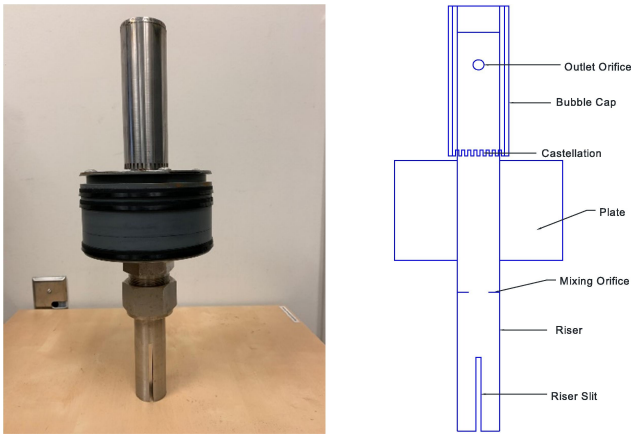

Figure 2.3: Picture and schematic of bubble cap distributor ; not to scale.[2]

Tap water was used to simulate “bubble coalescing” conditions while 0.5 wt% aqueous ethanol was used to suppress bubble coalescence. Gas superficial velocities were varied between 0.01 and

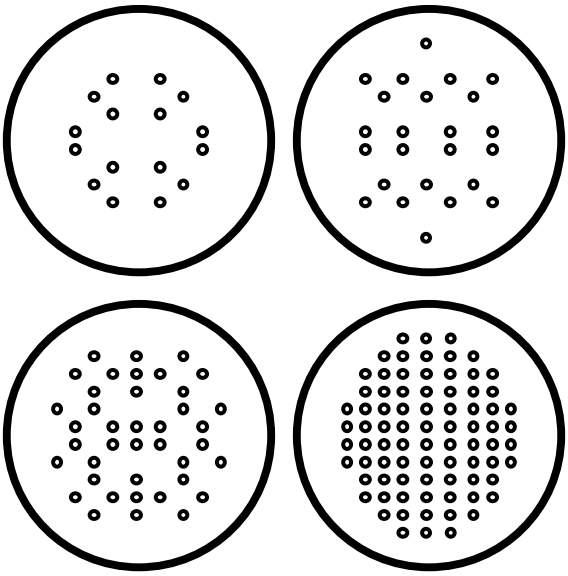

Figure 2.4: Perforated plates with various number (16, 24, 40, 80) of 4 mm holes.

0.11 m/s and liquid superficial velocities were varied between 0.015 and 0.047 m/s for the bubble cap plate, and 0.015 and 0.067 m/s for the perforated plate. The range of liquid flowrates for the bubble cap plate was limited by the head of the pump and elevated pressure drop through the bubble cap.

Overall gas holdups were determined from differential pressure measurements. For the first two set-ups, the reference port was located 0.18 m above the bubble cap while the measurement points were located 0.48, 0.70, and 0.89 m above the bubble cap plate. In the third set-up, the reference was located 0.05 m above the perforated plate while the measurement points were equally spaced by 0.1016 m. Bubble properties (local gas holdup, chord length and rise velocity) were measured with a monofibre optical probe located 0.83 m above the distributor plate. Previous work by Guan and Yang [19] showed that the radial gas holdup profile is fully developed above a height of 0.6 m and 0.2 m in the homogeneous and heterogeneous flow regime, respectively. The probe was positioned at five radial positions (r/R: 0, 0.26, 0.39, 0.52, and 0.64) to gather data for the evaluation of cross-sectional average of the measured properties.

2.2.2 *Measurement Techniques*

2.2.2.1 *Global Gas Holdup*

Axial pressure profiles were obtained with a pressure transducer manufactured by ABB Inc. (Model #: 266DSHHHSA2A1/V1E4L5). The axial pressure profile can be related to the overall gas holdup, as shown in Eq. 2.1, assuming frictional losses due to the wall and vertical phase acceleration are negligible.

$$\varepsilon_G = \frac{-\Delta P/\Delta z}{(\rho_L - \rho_G)g} \tag{2.1}$$

2.2.2.2 *Monofibre Optical Probe*

A custom 1C-3C monofibre optical probe previously validated by Parisien et al.[20] was used to obtain local gas holdups, bubble chord lengths and rise velocities. The probe exploits the difference in the refractive index of the gas and the liquid to determine these bubble properties. An opto-electronic module sends a laser through an optical fibre to the tip of the probe and depending on the phase occupying the tip, the laser is either reflected or refracted. More light is reflected when the tip is inside a bubble since the gas has lower refractive index than the liquid. The reflected light signal is detected and converted to a digital voltage signal by the optoelectronic module. The signal is then analyzed, by the SO6 software provided by the manufacturer (A2 Photonics Inc.), for signal rise time and bubble residence time. Prior to the collection of the data, lower and upper thresholds for signal rise must be set for the software to determine the rise time correctly. In this study, a lower and upper threshold of respectively 10% and 80% were used as recommended by the manufacturer. Data was sampled at a rate of 200 kHz for 180 s or until 10,000 bubbles were detected.

The local gas holdup is determined from the sum of bubble residence times and total measurement time, while the individual bubble rise velocity is calculated from signal rise time and probe sensing

length obtained from a calibration curve.[21] The bubble chord length is determined once the rise velocity and residence time are known.

$$\varepsilon_g(r) = \sum_i \frac{t_{b,i}}{t_T} \tag{2.2}$$

$$u_{b,i} = \frac{L_s}{t_{R,i}} \tag{2.3}$$

$$c_{b,i} = u_{b,i}\, t_{b,i} \tag{2.4}$$

Limitations of optical probes have been addressed by previous studies, where three sources of errors, due to "blinding", "crawling", and "drifting" effect, were identified.[22–24] Blinding and drifting effects result in the underestimation of bubble residence time, due to imperfect tip dewetting and a change in bubble trajectory at the tip, respectively. The crawling effect is caused by the deformation and deceleration of the bubble at the tip and leads to the overestimation of the residence time. These limitations cause a bias in average gas holdup of up to +35% and -35% for air-water and air-water-ethanol system, respectively.

2.3 RESULTS AND DISCUSSION

2.3.1 *Effect of fluids velocities and distributor type*

In Fig. 2.5, the overall gas holdup increases with both gas and liquid superficial velocities. For independent single phase injection and/or microbubbles with very small slip velocity, an increase in liquid velocity will impart additional momentum to the bubbles resulting in a lower residence time and gas holdup.[20,25,26] On the other hand, the two-phase bubble cap distributor produces progressively smaller bubbles as the liquid flow increases due to greater liquid phase turbulence

and enhanced bubble breakage. The decrease in bubble size and slip velocity increases the residence time and overall gas holdup.

Fig. 2.6 compares optical probe measurements of average bubble chord lengths for different gas and liquid superficial velocities in air-water and air-water-ethanol system, with sintered porous pipe feeding the bubble cap. Fig. 2.7 shows sample chord lengths distributions detected by the probe for a given operation condition. The probe measurements were limited to the dispersed flow regime (UG < 0.055 m/s), where the impact of the distributor is significant. The chord lengths decrease with liquid velocity due to enhanced bubble breakage. An opposite trend is observed for increasing gas velocities, and there are two possible reasons for this: (i) higher rate of bubble coalescence due to increasing number of bubbles and rate of bubble-bubble collision, and/or (ii) attenuation of liquid phase turbulence by the increasing number of micro-bubbles.[27] Moreover, the change in chord length with gas superficial velocity is more rapid in the air-water system than in the air-water-ethanol system due to bubble coalescence inhibition in the latter. As expected, the average rise velocities in Fig. 2.8 increase with gas superficial velocity and decrease with liquid superficial velocity.

It was theorized that, for a two-phase distributor, enhanced bubble breakage at higher liquid velocities is responsible for the increasing gas holdups in Fig. 2.5. Fig. 2.6, Fig. 2.8 confirm that the average bubble size and rise velocity decrease with liquid velocity, demonstrating the effect of the two-phase distributor on overall gas holdup is due to enhanced bubble breakage.

Fig. 2.9 compares overall gas holdups measured with different gas spargers feeding the bubble cap. The perforated pipe sparger produces larger initial bubbles than the sintered pipe since the former has larger openings (see Fig. 2.10). However, similar gas holdups were measured above the bubble cap at matching gas and liquid superficial velocities, suggesting that the effect of initial bubble size sparged in the plenum is negligible under these operating conditions.

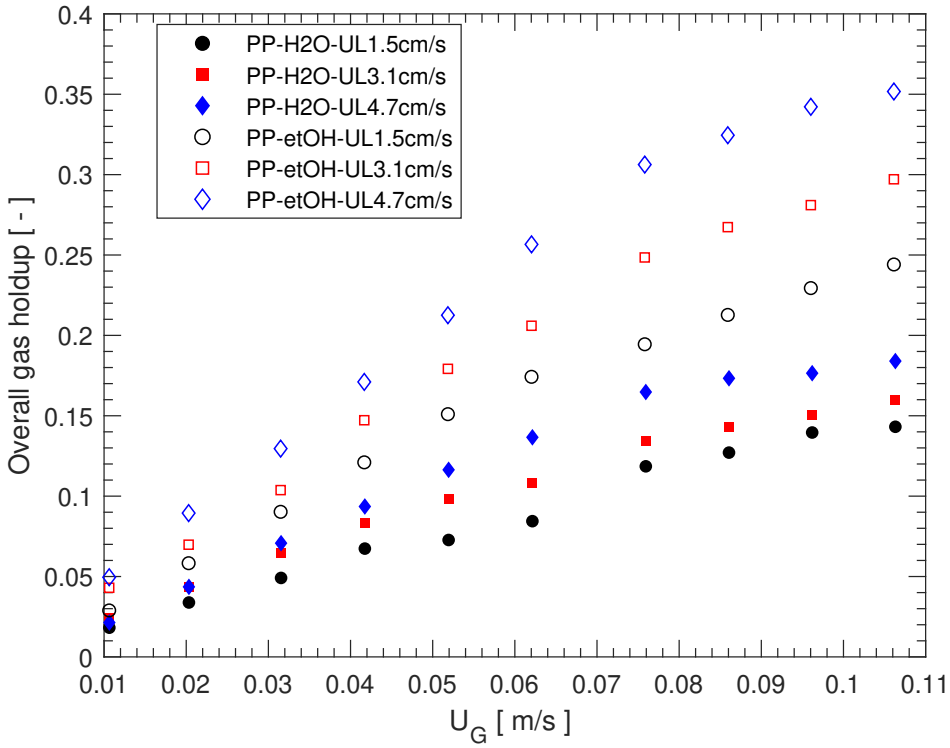

Figure 2.5: Overall gas holdups collected above the bubble cap plate, with perforated pipe (PP) as gas sparger.

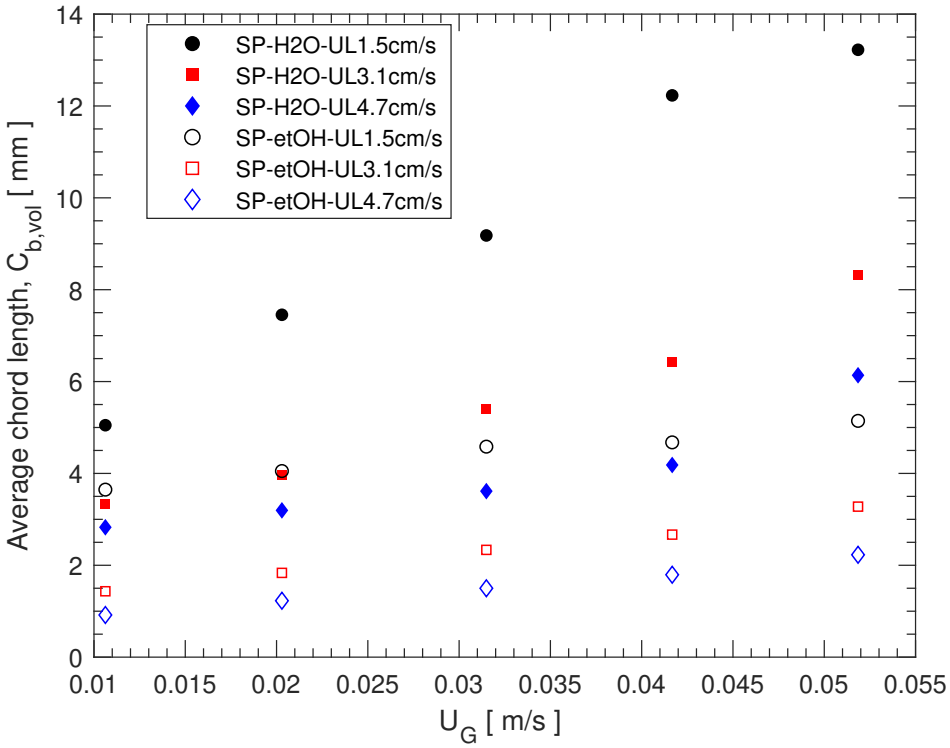

Figure 2.6: Bubble chord lengths in air-water and air-water-ethanol system with sintered porous pipe (SP) sparger in the plenum.

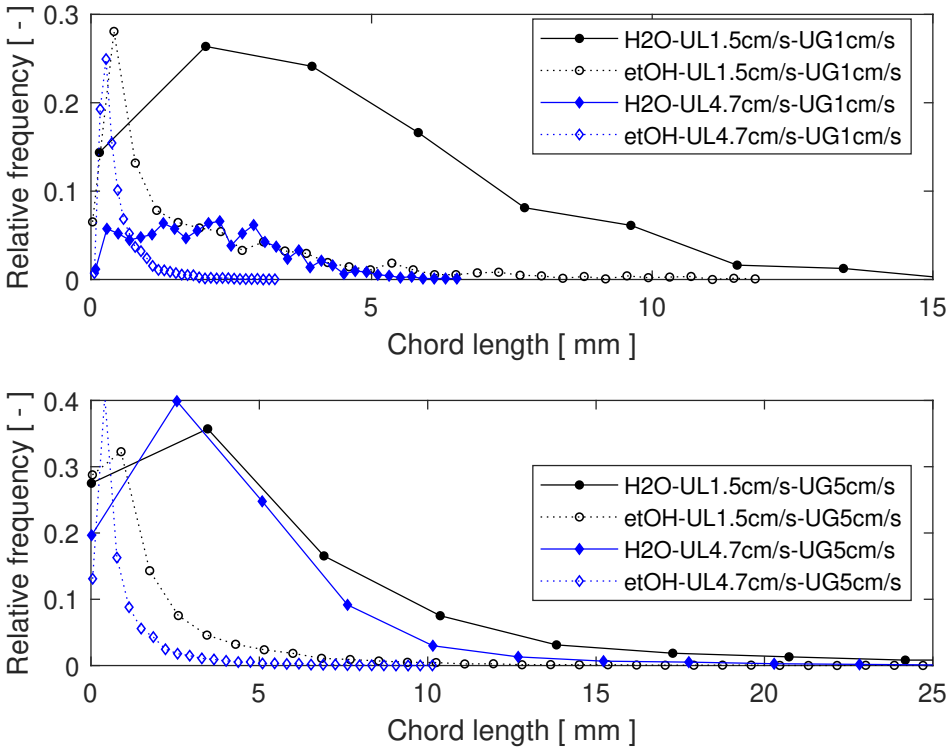

Figure 2.7: Chord Length Distributions measured in air-water and air-water-ethanol system with sintered porous pipe (SP) gas sparger and single bubble cap (SBC) gas-liquid distributor.

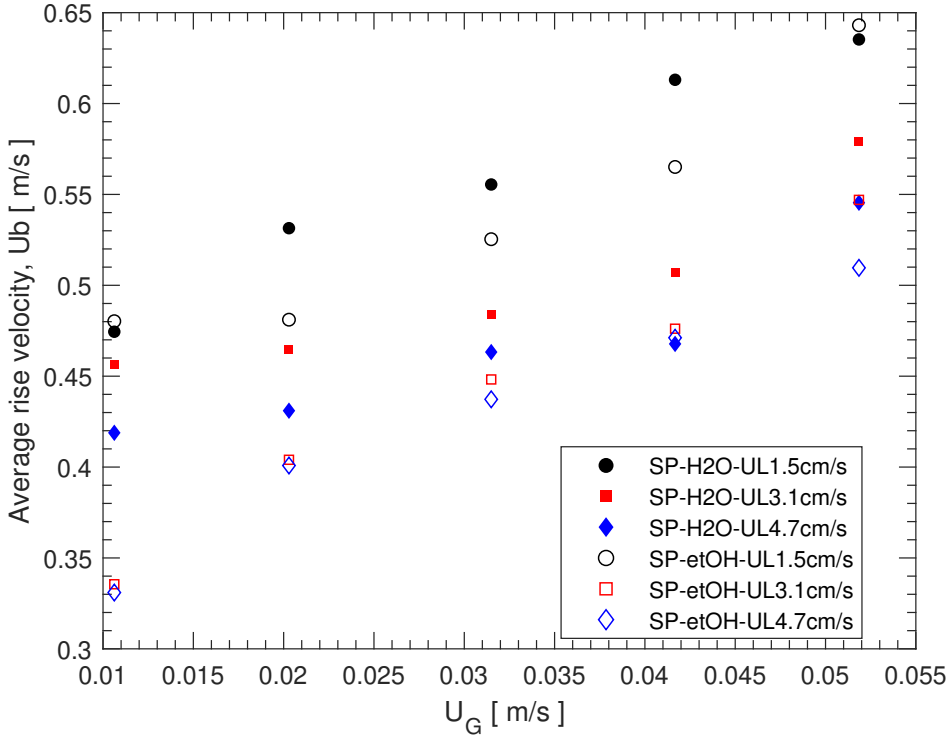

Figure 2.8: Bubble rise velocities in air-water and air-water-ethanol system with sintered porous pipe (SP) sparger in the plenum.

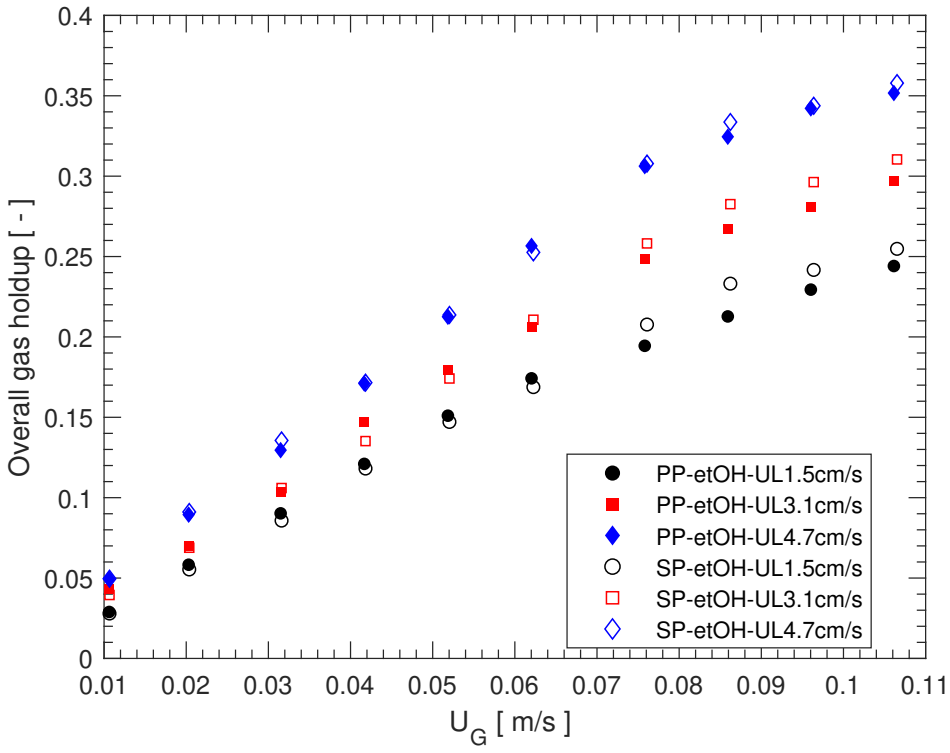

Figure 2.9: Comparison of gas hold ups measured with different gas spargers in air-water-ethanol system.

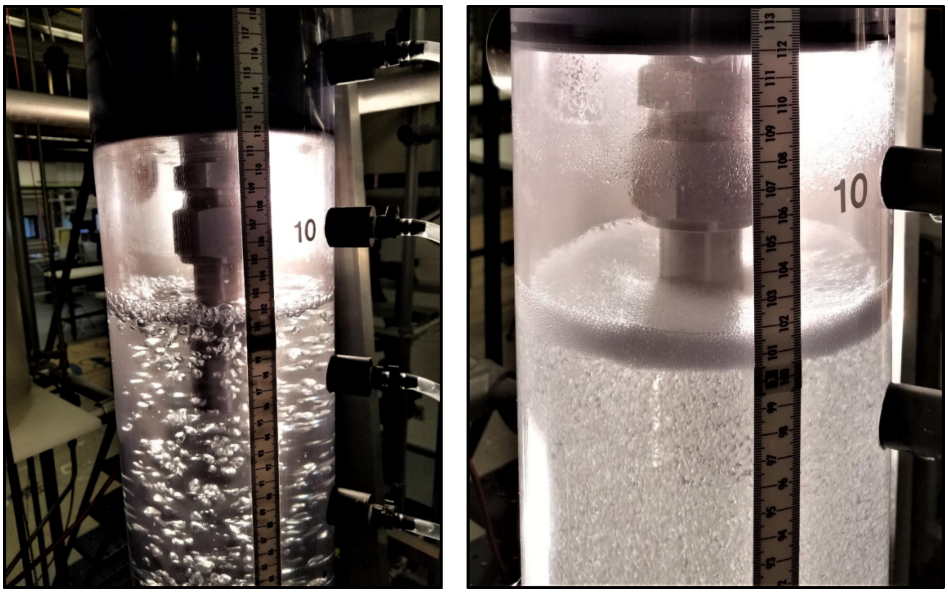

Figure 2.10: Comparison of bubble sizes generated by perforated pipe (left) and sintered porous pipe (right) in the plenum chamber (U_L = 0.015 m/s and U_G = 0.01 m/s, air-water-ethanol flow).

2.3.2 *Relationship between bubble size and energy dissipation rate*

To relate the measured bubble properties to the rate of energy dissipation by the bubble cap plate, single phase (0.5 wt% ethanol in water) and two-phase (air-water and air-water-ethanol) pressure drop through the bubble cap were collected. Fig. 2.11 is a plot of single-phase pressure drop and Euler number against Reynolds number. The single-phase pressure drop increases with Reynolds number as expected. However, the Euler number, which is proportional to the frictional factor, is relatively constant, implying that the flow through the bubble cap is turbulent at the liquid flowrates investigated. Note that the Reynolds number is based on the internal diameter of the riser, which is larger than the diameter of either orifices.

Fig. 2.12 is a plot of two-phase pressure drop against gas superficial velocity at various liquid flowrates. As gas velocity increases, the pressure drop initially increases, then plateaus and begin to rise again. With an increase in liquid velocity, the start of the plateau occurs at a greater gas velocity such that U_G/U_L remains around 1 at that point, whereas the plateau ends at a relatively constant gas velocity of around 7 cm/s. Generally, greater changes in pressure drop occur with an increase in liquid velocity than with gas velocity. Interestingly, similar pressure drops were measured in air-water and air-water-ethanol systems at matching gas and liquid superficial velocities.

The pressure drops in Fig. 2.12 were normalized by the fluid residence time (assuming no-slip between phases) in the high-power dissipation zones (volumes of mixing and outlet orifice), as shown in Eq. 2.5. The power dissipation is per unit mass of liquid, since it is where the turbulent eddies responsible for bubble breakup reside.

$$\varepsilon = \frac{\Delta P Q_{tot}}{\rho_L (V_m + V_o)} \tag{2.5}$$

Fig. 2.13 shows average bubble sizes against distributor energy dissipation rates for ethanol contaminated dispersed bubbly flow. At constant gas superficial velocity, the bubble size decreases monotonically with energy dissipation rate. Although larger bubbles were measured at higher gas velocities, a similar dependence on energy dissipation rate was observed. Considering an isotropic turbulent flow field where bubbles split when pressure fluctuations (associated with velocity fluctuations) overcome surface forces (e.g. surface tension) that tend to stabilize the bubble, Hinze [5] reasoned that the maximum stable bubble size in a dilute turbulent dispersion is proportional to the energy dissipation rate to the power of -0.4. According to Middleman, [6] the average bubble size is a fraction of the maximum stable bubble size and depends on the energy dissipation rate to the same power of -0.4, which partly explains the trend in Fig. 2.13. As mentioned, Hinze model is valid for dilute dispersions with little or no tendency for bubbles to coalesce but it can be extended to dense turbulent dispersions through an energy balance. The balance considers the minimal rate of surface energy formation and the rate of turbulent energy supply by the continuous phase to determine the maximum stable bubble size. [4]

$$\rho_L \left(\varepsilon d_{max}\right)^{\frac{2}{3}} Q_L = 6C_1 \frac{\sigma}{d_{max}} Q_G \tag{2.6}$$

$$d_{max} = \left(6C_1\right)^{0.6} \left(\frac{\sigma}{\rho_L}\right)^{0.6} \varepsilon^{-0.4} \left(\frac{Q_G}{Q_L}\right)^{0.6} \tag{2.7}$$

$$d_b = C_2 \left(6C_1\right)^{0.6} \left(\frac{\sigma}{\rho_L}\right)^{0.6} \varepsilon^{-0.4} \left(\frac{U_G}{U_L}\right)^{0.6} \tag{2.8}$$

Eq. 2.8 was further simplified to give Eq. 2.9, where the exponents and the pre-multiplication factor are originally assumed to be unknown.

$$d_b = \beta_1 \varepsilon^{\beta_2} \left(\frac{U_G}{U_L}\right)^{\beta_3} \tag{2.9}$$

Parameters in Eq. 2.9 were estimated using the data obtained with the three set ups to determine the effect of gas-liquid distributor geometry. The data was limited to air-water-ethanol flow and gas superficial velocities less than 0.055 m/s to limit the influence of bubble coalescence above the distributor. Table 2.2 shows results with the exponents fixed to their theoretical values (β_2 = -0.4; β_3 = 0.6). A relatively good fit was obtained for the two models as shown by $R^2 > 0.8$, an average absolute relative error (AARE) < 22%, and a bias factor (F_m) only slightly greater than unity (see Fig. 2.14). Considering a similar approach to active volume selection, β_1 differs for bubble cap (0.112) and perforated plate (0.044). This suggests that the effect of geometry may not be negligible here. Formation of a gas pocket inside the riser and bubble recoalescence in the annulus between the bubble cap and the riser are likely responsible for the larger bubbles observed with the bubble cap distributor.

Table 2.2: Bubble diameter model parameters

Gas-liquid distributor	β_1	β_2	β_3	R^2	AARE	F_m
Bubble cap	0.112 ± 0.011	-0.4	0.6	0.817	0.22	1.12
Perforated plate	0.044 ± 0.004	-0.4	0.6	0.72	0.18	1.19

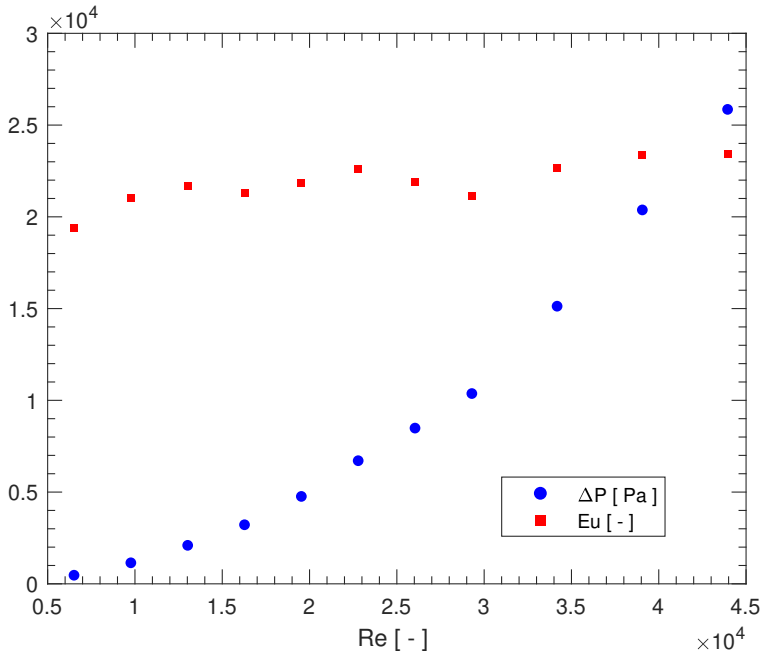

Figure 2.11: Single phase (liquid) pressure drop through the bubble cap.

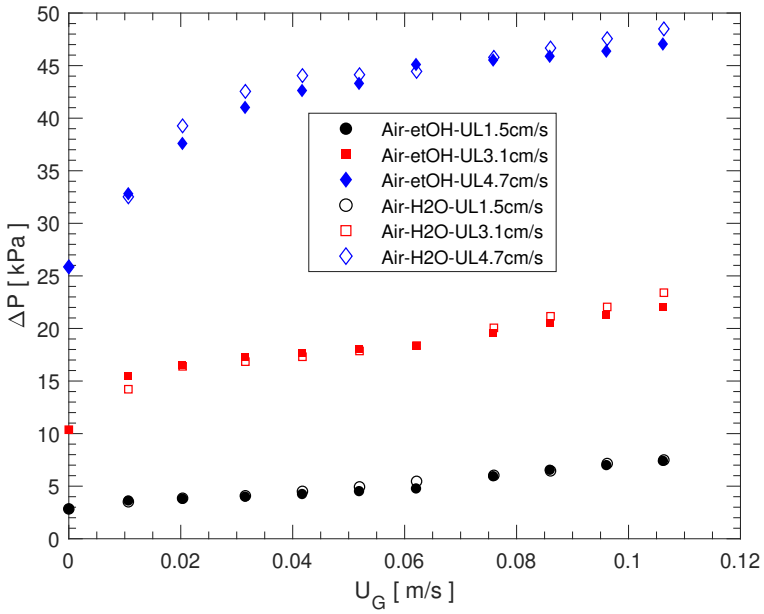

Figure 2.12: Two phase pressure drop through the bubble cap in air-water and air-water-ethanol system with sintered porous pipe in the plenum.

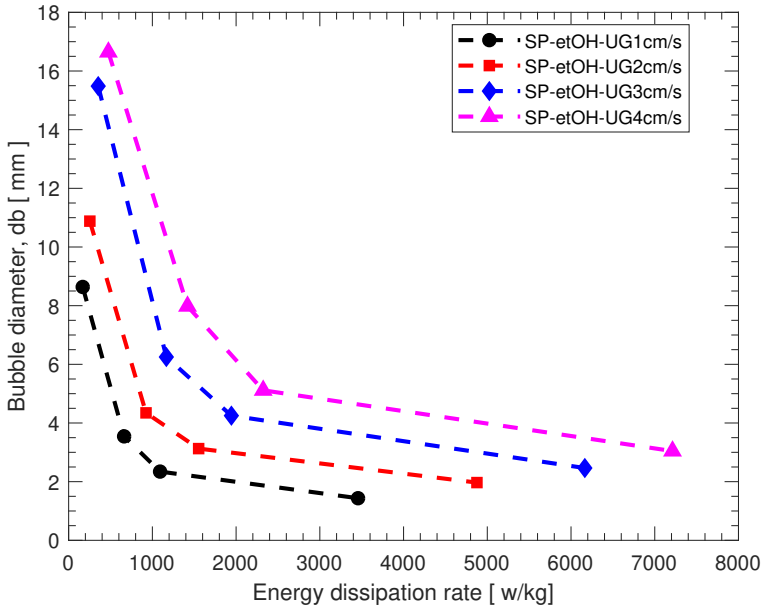

Figure 2.13: Bubble diameter against energy dissipation rate for air-water-ethanol flow with sintered porous pipe (SP) sparger in the plenum.

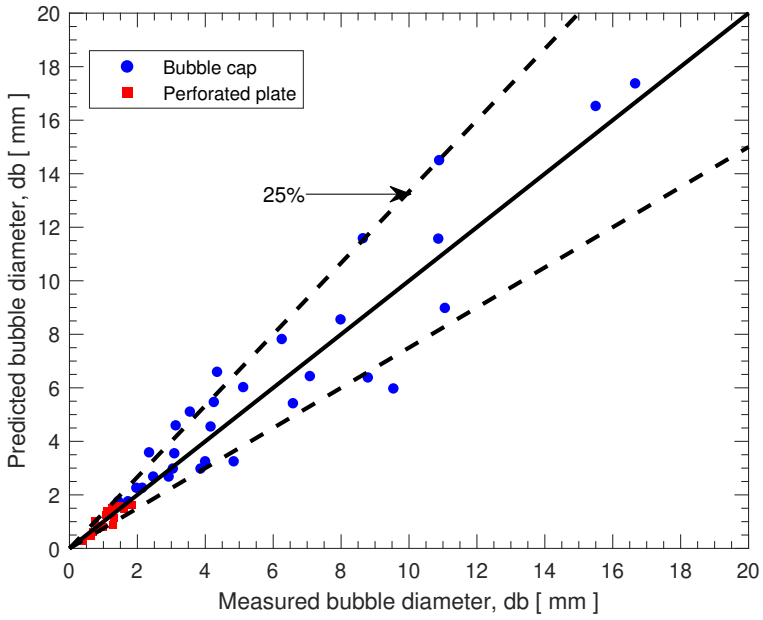

Figure 2.14: Parity plot for bubble size model developed for air-water-ethanol flow through perforated plate and bubble cap distributor.

2.3.3 *Plenum conditions and grid effects*

As previously mentioned, the free surface under ideal plenum conditions is horizontal. To confirm this was the case, three photographs of the plenum chamber were taken. The left-most photograph in Fig. 2.15 was taken before the gas was introduced, while the other two were taken after gas introduction. The gas pocket grows over time until a sufficient opening on the riser slit is available for gas entry and pressure equalization with the liquid.

In the industrial unit, the action of the recycle pump induces a swirling flow inside the plenum. The swirl causes a tilt in the free surface, which can result in risers closer to the wall receiving less gas than those at the center since a smaller open area may be exposed for gas entry. The previous section quantified the impact of different gas-liquid flow ratios and total fluid flow rates on the bubble properties. Here, the impact of gas and liquid superficial velocities as well as surface active compounds on the behavior of the free surface in the plenum is investigated qualitatively. Fig. 2.16 contains pictures of the free surface at two gas and two liquid superficial velocities for

air-water flow. The free surface is relatively sharp at low gas superficial velocities. At higher gas superficial velocities, it is less sharp and thicker. An increase in liquid superficial velocity has a stabilizing effect on the free surface. The bubble cap dampens fluctuations originating from the free surface, leading to little or no change in bubble frequency above (see attached video). As shown in Fig. 2.17, the presence of ethanol in the liquid increases the thickness of the interface due to foaming. The free surface fluctuates more with increasing gas velocities, but by comparing images in Fig. 2.16, Fig. 2.17, the magnitude of the fluctuations is lower with ethanol in tap water.

As shown in Fig. 2.18, bubbles emerging from the bubble cap are smaller than those in the plenum chamber. In addition, the bubble cap creates a wider range of bubble sizes relative to the ones in the plenum. The size distribution is even broader in air-water-ethanol system than in air-water system. This observation was further confirmed with optical probe measurements, which showed a 4.3% increase in mean normalized standard deviation (chord length distribution) when ethanol was added. This has possible implications for gas-liquid separation at the recycle pan, where small bubbles with low slip velocity are entrained in the liquid recycle since they cannot disengage fast enough. If this happens, the entrained gas would increase gas throughput and gas hold up in the bed at the expense of liquid hold up and product yield.

Figure 2.15: Plenum liquid level before and after switching the gas on (U_L = 0.015 m/s, U_G = 0.01 m/s, air-water flow). Left most picture was taken with liquid flow but before the gas was introduced through a sintered pipe. The two pictures to the right were taken shortly afterwards and with gas flowing. The gas pocket formed due to bubble coalescence at the free surface grows over time until enough slit area is open to ensure both phases enter at the same pressure.

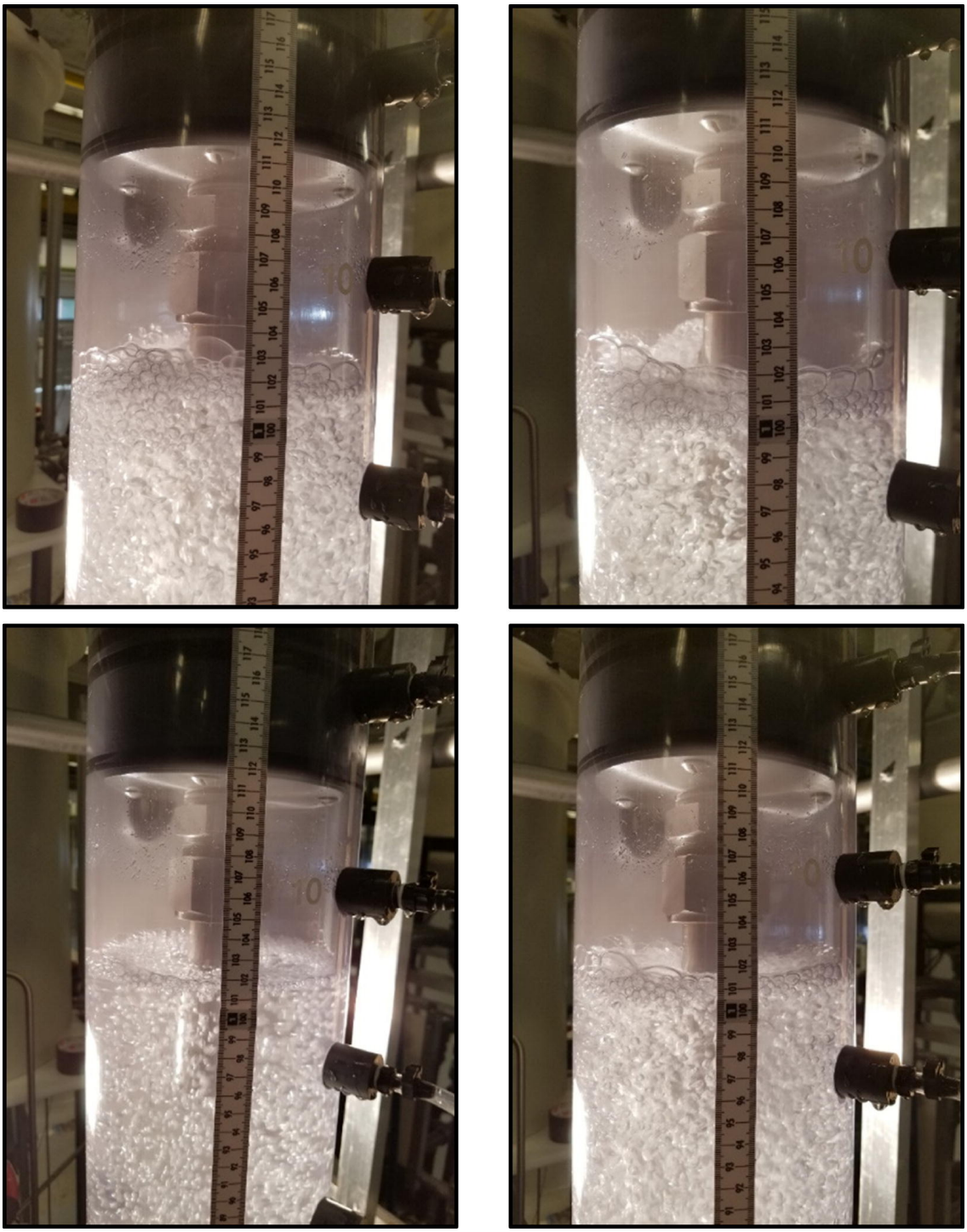

Figure 2.16: Plenum liquid level at various gas and liquid superficial velocities in air-water flow. Top left: $U_L = 1.5$ cm/s and $U_G = 1$ cm/s; top right: $U_L = 1.5$ cm/s and $U_G = 5$ cm/s; bottom left: $U_L = 3.1$ cm/s and $U_G = 1$ cm/s; bottom right: $U_L = 3.1$ cm/s and $U_G = 5$ cm/s.

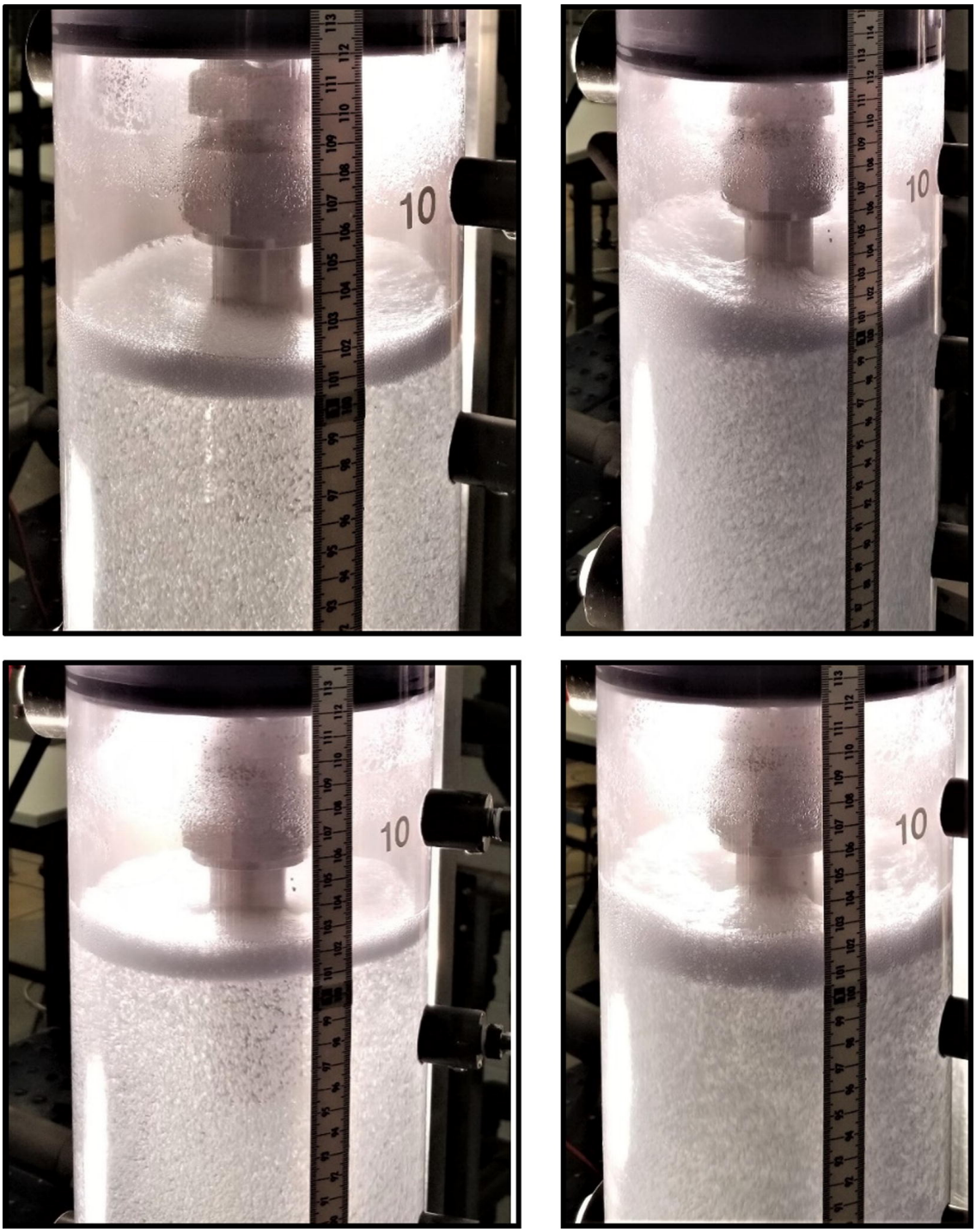

Figure 2.17: Plenum level at various gas and liquid superficial velocities in air-water-ethanol flow, with sintered porous pipe as sparger. Top left: U_L = 1.5 cm/s and U_G = 1 cm/s; top right: U_L = 1.5 cm/s and U_G = 5 cm/s; bottom left: U_L = 3.1 cm/s and U_G = 1 cm/s; bottom right: U_L = 3.1 cm/s and U_G = 5 cm/s.

Figure 2.18: Bubble cap inlet and outlet conditions for air-water and air-water-ethanol flow, with perforated pipe gas sparger (U_L = 0.015 m/s; U_G = 0.01 m/s). Top left: bubbles before entering the bubble cap, air-water flow; top right: bubbles emerging from the bubble cap, air-water flow; bottom left: bubbles before entering the bubble cap, air-water-ethanol flow; bottom right: bubbles emerging from the bubble cap, air-water-ethanol flow.

2.4 CONCLUSIONS

This study aimed to determine the effect of plenum conditions and gas-liquid distributor on bubble column hydrodynamics. In the context of LC-Fining™ hydroprocessors, the interdependent effects of liquid recycle pan efficiency, recycle pump speed and a free surface tilt in the plenum was investigated by passing various gas and liquid flow rates through a single bubble cap plate. The impact of gas-liquid distributor geometry was further investigated by comparing a bubble cap plate to a perforated plate. Finally, different gas spargers were used to deliver different bubble sizes in the plenum to investigate the resulting effect of initial bubble size.

Gas and liquid superficial velocities were found to influence the resulting bubble properties. Under ideal plenum conditions, a sharp horizontal free surface was observed at low gas superficial velocities. The position of the free surface fluctuated with increasing gas velocities, but the effect was attenuated by increasing liquid velocity and the addition of ethanol to the liquid phase. Visual observations showed that the bubble cap could dampen these fluctuations, resulting in little change in bubble frequency above.

The measured bubble sizes were found to correlate well with the energy dissipation rate and gas-liquid velocity ratio to the power of -0.4 and 0.6, respectively, in agreement with previous studies on the breakup of dense turbulent dispersion. The geometry of the gas-liquid distributor influenced the resulting bubble properties through the proportionality constant, for which the bubble cap had higher value than the perforated plate. Visual observations and optical probe measurements revealed that the bubble cap creates a broad distribution of bubble sizes, which has possible implications for gas-liquid separation at the recycle pan. Smaller bubbles with low slippage are likely to be entrained with the liquid recycle since they disengage slowly. This in turn could lead to increased gas throughput and gas holdup in the fluidized bed, thus limiting the

effective reactor volume and product yield.

The initial bubble size in the plenum chamber was found to have negligible effect on gas holdup above the bubble cap suggesting that more effort should be focussed on redesigning the grid, rather than upstream gas introduction equipment, to optimize bed holdups and product yield.

ACKNOWLEDGEMENTS

The authors are grateful to Stéphane Gluck and Nicolas Zuanon of A2 Photonic Sensors for their valuable insights and technical support. The authors would also like to thank the Natural Sciences and Engineering Research Council of Canada, Ontario's Ministry of Training, Colleges and Universities, and Syncrude Canada Ltd. for financial assistance.

NOMENCLATURE

$c_{b,i}$	Individual bubble chord length, m
$n_{b,i}$	Number of bubbles with chord length, $c_{b,i}$
n_b	Number of bubbles measured locally, $\sum_i n_{b,i}$
N_b	Total number of bubbles measured globally, $\sum n_b$
$c_{b,vol}$	Local volume average chord length, $\left(\frac{1}{n_b}\sum_i c_{b,i}^3 n_{b,i}\right)^{\frac{1}{3}}$, m
$C_{b,vol}$	Global average chord length, $\frac{1}{N_b}\sum c_{b,vol} n_b$, m
$u_{b,i}$	Individual bubble rise velocity, m/s
u_b	Local average rise velocity, $\frac{1}{n_b}\sum_i u_{b,i} n_{b,i}$, m/s
U_b	Global average rise velocity, $\frac{1}{\pi R^2 \varepsilon_G}\int_0^R u_b \varepsilon_g(r)\, 2\pi r dr$, m/s
d_b	Average bubble diameter, $\frac{3}{2} C_{b,vol} E^{-\frac{2}{3}}$, m
d_{max}	Maximum stable bubble size, m

E	Bubble aspect ratio, $\frac{1}{1+0.163Eo^{0.757}}$
Eo	Eotvos number, $\frac{g(\rho_L-\rho_G)d_b^2}{\sigma}$
L_s	Optical probe sensing length, μm
$t_{R,i}$	Signal rise time, ms
$t_{b,i}$	Bubble residence time, ms
ΔP	Dynamic pressure drop,Pa
V_m	Volume of the mixing orifice, m^3
V_o	Volume of the outlet orifice, m^3
U_G	Gas superficial velocity, m/s
U_L	Liquid superficial velocity, m/s
Q_G	Gas volumetric flow rate, m^3/s
Q_L	Liquid volumetric flow rate, m^3/s
Q_{tot}	Total volumetric flowrate, m^3/s
Δz	Vertical distance between differential pressure ports, m
g	Acceleration due to gravity, m/s^2
r	Probe radial position, m
R	Radius of the column, m
SP, PP	Sintered porous pipe, perforated pipe
SBC	Single bubble cap
ε	Energy dissipation rate, W/kg
$\varepsilon_g(r)$	local gas holdup, $m^3_{bubbles}/m^3_{reactor}$
ε_G	Global gas holdup, $\frac{1}{\pi R^2}\int_0^R \varepsilon_g(r)\,2\pi r dr$, $m^3_{bubbles}/m^3_{reactor}$
ρ_G, ρ_L	Gas and liquid density, kgm^{-3}
σ	surface tension, N/m

[1] Craig A. McKnight, Larry P. Hackman, John R. Grace, Arturo Macchi, Darwin Kiel, and Jonathan Tyler. Fluid Dynamic Studies in Support of an Industrial Three-Phase Fluidized Bed Hydroprocessor. *Can. J. Chem. Eng.*, 81(3-4):338–350, jun 2008. ISSN 0008-4034. doi: 10.1002/cjce.5450810302.

[2] James H. Colvert. Bubble cap assembly in an ebullated bed reactor, 1989.

[3] Steven Xuqi Song, Donald Leroy Kuehne, Abdenour Kemoun, and Bruce Edwards Reynolds. Apparatus and method for hydroconversion, 2016.

[4] Neima Brauner. The prediction of dispersed flows boundaries in liquid-liquid and gas-liquid systems. *Int. J. Multiph. Flow*, 27(5):885–910, may 2001. ISSN 03019322. doi: 10.1016/S0301-9322(00)00056-2.

[5] J. O. Hinze. Fundamentals of the hydrodynamic mechanism of splitting in dispersion processes. *AIChE J.*, 1(3):289–295, sep 1955. ISSN 15475905. doi: 10.1002/aic.690010303.

[6] Stanley Middleman. Drop Size Distributions Produced by Turbulent Pipe Flow of Immiscible Fluids through a Static Mixer. *Ind. Eng. Chem. Process Des. Dev.*, 13(1):78–83, jan 1974. ISSN 01964305. doi: 10.1021/i260049a015.

[7] E. Camarasa, C. Vial, S. Poncin, G. Wild, N. Midoux, and J. Bouillard. Influence of coalescence behaviour of the liquid and of gas sparging on hydrodynamics and bubble characteristics in a bubble column. *Chem. Eng. Process. Process Intensif.*, 38(4-6):329–344, 1999. ISSN 02552701. doi: 10.1016/S0255-2701(99)00024-0.

[8] Bimal Gandhi, Anand Prakash, and Maurice A. Bergougnou. Effects of sparger height and orifice orientation on solids dispersion in a slurry bubble column. *Can. J. Chem. Eng.*, 77(2):383–391, apr 1999. ISSN 00084034. doi: 10.1002/cjce.5450770226.

[9] D. Geldart and J. Baeyens. The design of distributors for gas-fluidized beds. *Powder Technol.*, 42(1):67–78, apr 1985. ISSN 00325910. doi: 10.1016/0032-5910(85)80039-5.

[10] Lu Han and Muthanna H. Al-Dahhan. Gas-liquid mass transfer in a high pressure bubble column reactor with different sparger designs. *Chem. Eng. Sci.*, 62(1-2):131–139, jan 2007. ISSN 00092509. doi: 10.1016/j.ces.2006.08.010.

[11] Anand V. Kulkarni and Jyeshtharaj B. Joshi. Design and selection of sparger for bubble column reactor. Part I: Performance of different spargers. *Chem. Eng. Res. Des.*, 89(10):1972–1985, 2011. ISSN 02638762. doi: 10.1016/j.cherd.2011.01.004.

[12] Anand V. Kulkarni and Jyeshtharaj B. Joshi. Design and selection of sparger for bubble column reactor. Part II: Optimum sparger type and design. *Chem. Eng. Res. Des.*, 89(10):1986–1995, oct 2011. ISSN 02638762. doi: 10.1016/j.cherd.2011.01.014.

[13] Raymond Lau, Wei Shan Beverly Sim, and Rujuan Mo. Effect of gas distributor on hydrodynamics in shallow bubble column reactors. *Can. J. Chem. Eng.*, 87(6):847–854, 2009. ISSN 00084034. doi: 10.1002/cjce.20224.

[14] C. J.P. Ouyang and G. B. Tatterson. The Effect of Distributors on Two-Phase and Three-Phase Flows in Vertical Columns. *Chem. Eng. Commun.*, 49(4-6):197–215, 1987. ISSN 15635201. doi: 10.1080/00986448708911803.

[15] Fereshteh Rahimpour, Reza Zarghami, and Navid Mostoufi. Effect of distributor on fluidized bed hydrodynamics. *Can. J. Chem. Eng.*, 95(11):2221–2234, 2017. ISSN 1939019X. doi: 10.1002/cjce.22895.

[16] Safa Sharaf, Maria Zednikova, Marek C. Ruzicka, and Barry J. Azzopardi. Global and local hydrodynamics of bubble columns - Effect of gas distributor. *Chem. Eng. J.*, 288:489–504, 2016. ISSN 13858947. doi: 10.1016/j.cej.2015.11.106.

[17] NG Deen, RF Mudde, JAM Kuipers, Peter Zehner, and Matthias Kraume. Bubble columns. *Ullmann's encyclopedia of industrial chemistry*, 2010.

[18] K D P Nigam. Three-Phase Sparged Reactors. In *Top. Chem. Eng.*, volume 8. Gordon and Breach Publishers, Netherlands, 1996.

[19] Xiaoping Guan and Ning Yang. Bubble properties measurement in bubble columns: From homogeneous to heterogeneous regime. *Chem. Eng. Res. Des.*, 127(1999):103–112, 2017. ISSN 02638762. doi: 10.1016/j.cherd.2017.09.017.

[20] Valois Parisien, Alixia Farrell, Dominic Pjontek, Craig A. McKnight, Jason Wiens, and Arturo Macchi. Bubble swarm characteristics in a bubble column under high gas holdup conditions. *Chem. Eng. Sci.*, 157:88–98, jan 2017. ISSN 00092509. doi: 10.1016/j.ces.2016.04.051.

[21] P. C. Mena, F. A. Rocha, J. A. Teixeira, P. Sechet, and A. Cartellier. Measurement of gas phase characteristics using a monofibre optical probe in a three-phase flow. *Chem. Eng. Sci.*, 63(16): 4100–4115, aug 2008. ISSN 00092509. doi: 10.1016/j.ces.2008.05.010.

[22] E. Barrau, N. Rivière, Ch Poupot, and A. Cartellier. Single and double optical probes in air-water two-phase flows: Real time signal processing and sensor performance. *Int. J. Multiph. Flow*, 25(2):229–256, mar 1999. ISSN 03019322. doi: 10.1016/S0301-9322(98)00042-1.

[23] Alain Cartellier. Optical probes for multiphase flow characterization: Some recent improvements. *Chem. Eng. Technol.*, 24(5):535–538, may 2001. ISSN 09307516. doi: 10.1002/1521-4125(200105)24:5<535::AID-CEAT535>3.0.CO;2-X.

[24] J. Enrique Juliá, Wouter K. Harteveld, Robert F. Mudde, and Harrie E.A. Van Den Akker. On the accuracy of the void fraction measurements using optical probes in bubbly flows. *Rev. Sci. Instrum.*, 76(3):035103, mar 2005. ISSN 00346748. doi: 10.1063/1.1862192.

[25] H. Chaumat, A. M. Billet-Duquenne, F. Augier, C. Mathieu, and H. Delmas. Mass transfer in bubble column for industrial conditions - Effects of organic medium, gas and liquid flow rates and column design. *Chem. Eng. Sci.*, 60(22):5930–5936, nov 2005. ISSN 00092509. doi: 10.1016/j.ces.2005.04.026.

[26] S. Kumar, R. A. Kumar, P. Munshi, and A. Khanna. Gas hold-up in three phase co-current bubble columns. *Procedia Eng.*, 42:782–794, jan 2012. ISSN 18777058. doi: 10.1016/j.proeng.2012.07.470.

[27] A. W. Vreman. Turbulence characteristics of particle-laden pipe flow. *J. Fluid Mech.*, 584: 235–279, aug 2007. ISSN 00221120. doi: 10.1017/S0022112007006556.

3

FLUID DYNAMICS SCALING OF A GAS-LIQUID DISTRIBUTOR APPLIED TO A COMMERCIAL EBULLATED BED HYDROPROCESSOR

ABSTRACT

A new scaling approach for a gas–liquid distributor is proposed and experimentally validated on a commercial bubble cap geometry. The geometric similarity was achieved by matching distributor fractional opening and ratios of various critical dimensions. The dynamic similarity was attained by matching three dimensionless groups (gas–liquid density ratio, liquid Reynolds number, and gas Froude number) and bubble coalescence behavior. Two geometrically similar distributors with one and three smaller bubble caps were experimentally compared through resulting bubble size distributions to test the scaling laws. A reasonably good agreement was found at various pressures, suggesting that the scaling approach could also work at industrially relevant conditions. New models for bubble size distribution and drag coefficient were developed to explicitly account for the effect of the gas–liquid distributor and thus improve the fluid dynamics modeling of commercial ebullated bed hydroprocessors.[1]

1 This chapter has been published in Industrial & Engineering Chemistry Research: doi.org/10.1021/acs.iecr.0c03224

3.1 INTRODUCTION

Oil sand bitumen is viscous and rich in impurities (sulfur, nitrogen, and heavy metals), making its direct transportation and refining impossible.[1] To overcome this, Syncrude Canada Ltd. partially upgrades its bitumen to synthetic crude oil, which is then transported to a refinery for final purification and transformation. At the production site, bitumen is first extracted and distilled at atmospheric and vacuum conditions. The atmospheric and vacuum residues are further processed using fluid bed cokers and ebullated bed hydroprocessors (LC-Fining units). The final products are hydrotreated and blended to form synthetic crude oil.

The LC-Fining unit, shown in Figure 3.1, is operated at elevated pressure ($\sim$ 11.7 MPa) and temperature ($\sim$ 440 °C), with multicomponent liquid that can foam.[2] By increasing gas density, elevated pressures enhance bubble breakage and create smaller bubbles with lower rise velocities.[3,4] Naturally occurring surface-active compounds further reduce the rise velocities of these smaller bubbles by inducing surface tension gradient and immobilizing the interface.[5] These two synergetic effects greatly increase gas holdup at the expense of liquid holdup and product yield. Moreover, the fluid distribution system and the liquid recycle pan affect the performance of the unit. A uniform spatial distribution of fluids ensures proper hydrogenation and prevents the formation of mesophase and coke, which deposit on the grid and further hinder the distribution. Given that bubbles do not readily coalesce through the bed,[6] the size of the bubbles formed at the distributor likely impacts gas–liquid separation at the recycle pan. The gas–liquid separation efficiency of the recycle pan is critical since gas entrained with the liquid recycle increases gas throughput and bed's gas holdup at the expense of liquid holdup and product yield.

A few researchers[7–10] have addressed the fluid dynamics scaling of industrial ebullated bed hydroprocessors. Safoniuk et al.[8] proposed a scaling approach based on using a cold flow unit, relaxing certain geometrical parameters and matching five dimensionless groups (Mo, Eo, Re_{l-s},

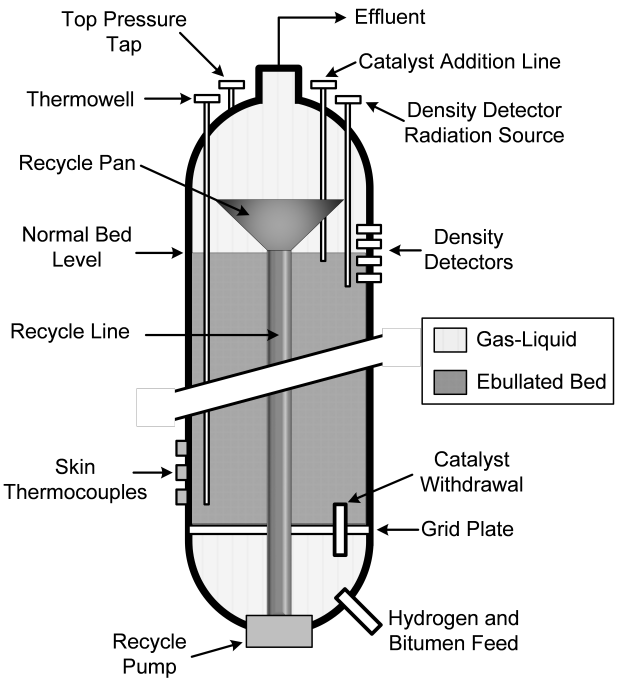

Figure 3.1: Simplified schematic of the LC-Fining unit (reprinted with permission from Pjontek et al.[7] Copyright 2015 Elsevier Ltd.)

ρ_s/ρ_l, U_g/U_l). Freeboard gas holdups measured in Safoniuk's cold flow unit were found to be significantly different from those measured in the LC-Fining unit at matching dimensionless groups.[2] The discrepancy was attributed to a number of potential issues including gas entrainment in the liquid recycle, inaccurate measurement of physical properties, and holdups in the industrial unit and/or missing dimensionless groups.

Macchi et al.[9] also tested the applicability of the scaling laws proposed by Safoniuk using single and multicomponent liquids in a gas–liquid–solid fluidized bed. Greater gas holdups were observed in multicomponent liquids than in single-component liquids due to bubble coalescence inhibition by surface-active compounds in the former. Macchi et al.[10] investigated the effect of gas density using a bubble column and gas–liquid–solid fluidized bed and reported higher gas holdups for denser gases in both cases. Both works demonstrated that the scaling of the industrial fluid dynamics must also consider bubble coalescence inhibition and enhanced bubble breakage at elevated pressures.

Following up on the works of Safoniuk et al.[8] and Macchi et al.,[9,10] Pjontek et al.[7] proposed a scaling strategy based on dimensional analysis and similitude to study local and global fluid dynamics in the bed and freeboard regions of the LC-Fining unit. Five dimensionless groups (Ar_{l-s}, Re_l, U_g/U_l, ρ_g/ρ_l, ρ_l/ρ_s) and bubble coalescence behavior were proposed to scale the industrial fluid dynamics. Pjontek et al.[6] measured local bubble properties in the freeboard, including gas holdups, bubble rise velocities, and chord lengths, using a monofiber optical probe capable of withstanding elevated pressures. Fluidized bed and freeboard measurements demonstrated that flow through the bed of particles enhanced bubble breakage for a water (bubble coalescing) system but had a negligible impact with an added surfactant (0.5 wt % ethanol). Thus, for the aqueous ethanol solution, local and global holdups in the freeboard region were similar to data obtained in the bubble column at matching operating conditions. Although the results for the aqueous ethanol solution suggest a negligible impact of particles on resulting bubbles, the particles may still break up the bubbles if they are smaller than the bubbles and/or if their holdup is significantly high. However, this is not the case since the particles were generally larger than the bubbles and solids holdup was significantly low ($\sim$ 20%). Further, bubble coalescence is likely insignificant due to the presence of a surface-active agent (i.e., ethanol). These results informed the decision to investigate the impact of a gas–liquid distribution system in a bubble column, which happens to be desirable as it minimizes the risk of damaging the optical probe from the impact of rogue particles.

Although the effects of fluid distribution system were considered in all of these studies, the goal was to understand bed fluid dynamics. As such, a detailed dimensional analysis and similitude of the fluid distribution system were not performed. A combination of sintered porous pipe (gas sparger) and perforated plate (gas–liquid distributor), which are geometrically different from the industrial fluid distribution system, were used.

A few other studies have been conducted to understand the effects of the fluid distribution system on bubble column and fluidized bed hydrodynamics.[11–20] With the exception of Ouyang and

Tatterson,[15] the fluid distribution system consisted of perforated plate, porous plate, or porous pipe(s) delivering a single fluid (gas). Ouyang and Tatterson[15] utilized a bubble cap plate to deliver gas–liquid and gas–liquid–solid mixtures and measured overall gas holdups and distributor pressure drops. A few other researchers[21–24] have also studied vertical gas–liquid flow through different orifice geometries, measuring pressure drops and, in some cases, void fraction. It is worth noting that scaling laws were not developed in these works.

Our previous work[25] investigated the interactions between plenum conditions and gas–liquid distributor at atmospheric conditions. Plenum conditions tested had a negligible impact on overall gas holdup above the distributor, and the resulting mean bubble size correlated to the gas–liquid velocity ratio, power dissipation, and distributor geometry. Although it is possible to scale the gas–liquid distributor based on power dissipation, it requires prior knowledge of pressure drop and fluids residence time through the distributor, which can be challenging to accurately predict. Moreover, scaling via power dissipation is based on isotropic turbulent bubble break-up through the risers of the bubble cap distributor, which may not always be the case such as for more viscous hydrocarbon feeds.

Although there is a plethora of published articles on bubble columns, there are less operated at high pressure with/without contaminated liquids, and even much fewer of these articles operate with a circulating liquid and a two-phase gas–liquid distribution system. The large majority of high-pressure articles is for a batch liquid and single-phase gas injection, which yields larger bubbles. Moreover, the bubble cap distributor geometry is unique to this study and it is preferable to not model the bubble size distribution as a function of power dissipation (i.e., bubble breakup based on isotropic turbulence) since the pressure drop and active volume and flow regimes are unknown a priori. Further, existing models typically provide the Sauter mean diameter, not the bubble size distribution, which is a more stringent dynamic similitude comparison. Thus, we propose a new alternative scaling approach via dimensional analysis and similitude for which

fluids velocities and phase properties are readily known beforehand. This scaling approach is not limited to highly turbulent flows and its validity will be demonstrated by matching of bubble size distributions at various pressures with a contaminated liquid, which are relevant to industrial operating conditions. Importantly, dimensionless bubble size distribution parameters are extracted and correlated to the relevant dimensionless groups. As mentioned, the bubble size and rise velocity distributions influence gas holdup in the hydroprocessor as well as the separation efficiency of the internal gas–liquid separator, which in turn affects liquid holdup and ultimately product yield. As such, this work will also propose a suitable drag coefficient model for conditions relevant to the LC-Fining unit.

3.2 GEOMETRIC CONSIDERATIONS

The industrial distributor is a circular plate with several bubble cap elements arranged in a triangular pattern. A schematic of a single bubble cap element is shown in Figure 3.2.[26] The bubble cap is connected to a riser which guides the gas–liquid mixture from the plenum chamber to the catalyst bed. The riser features two diametrically opposed rectangular slits to allow gas entry from the gas pocket formed in the plenum. The riser also features a ball check valve (not shown) above an orifice mixer to ensure unidirectional flow. The orifice mixer homogenizes the gas–liquid mixture to prevent alternating slugs of gas and liquid which would otherwise cause the ball to repeatedly beat against the seat and eventually cause premature wear. The end of the riser connected to the bubble cap features outlet orifices to further homogenize the flow before it exits the riser. After exiting the riser, the gas–liquid mixture flows down the annulus between the bubble cap and the riser, finally jetting radially outwards into the catalyst bed via the castellations and the clearance between the bubble cap and the plate. The flow through the castellations and the clearance ensures the final homogenization of the mixture and sweeps catalyst particles off the grid.

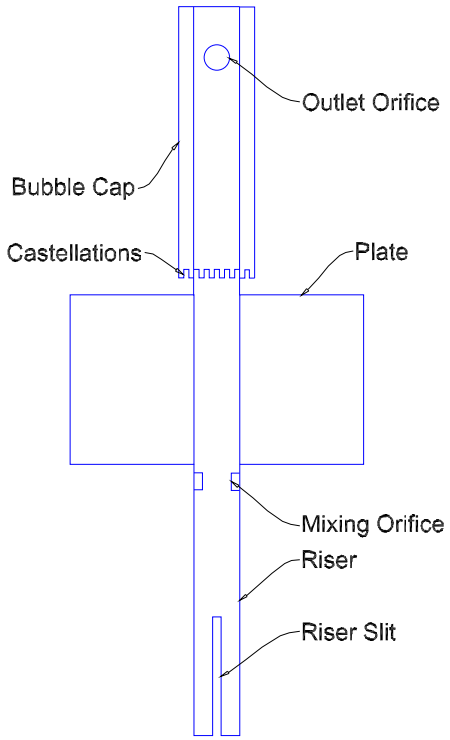

Figure 3.2: Riser and bubble cap configuration (adapted with permission from Mach et al.[25] Copyright 2020 Elsevier Ltd).

To ensure geometric similarity, the critical dimensions of the distributor needed to be identified. As mentioned, the industrial distributor is equipped with several bubble cap elements to ensure uniform fluids distribution. Therefore, the first task involves identifying an appropriate number of elements. Fractional open area (open area of outlet orifices per column's cross-sectional area) was chosen as a basis for selecting the number of elements. Initially, a single full-scale element was considered, but the fractional open area was found to be high for 0.1016 m i.d. column (Figure 3.3a). As a result, the size of the element was reduced to maintain fractional open area (Figure 3.3b). This scaling strategy assumes marginal interactions between gas–liquid dispersions emerging from neighboring bubble caps. This assumption could be valid if an appropriate pitch is maintained between elements and/or fluids velocities are not too high. To test this assumption, the number of elements is increased to three while maintaining the same fractional open area (Figure 3.3c). This resulted in smaller bubble caps with smaller orifice diameters. However, the pitch ratio (i.e., pitch per unit outlet orifice diameter) was still maintained from a single-scaled element in Figure

Table 3.1: Critical dimensions

Feature	Critical dimensions
Plate	Diameter, Thickness
Bubble cap	Internal diameter, height, number, height and width of castellations
Riser	Internal diameter, height below and above the plate
Riser slits	Number, height and width
Orifice mixer	Internal diameter and thickness
Outlet orifice	Number of orifices, area per orifice

3.3b. The second task in achieving geometric similarity involves identifying resulting critical dimensions (see Table 3.1) along with their respective values (not shown for proprietary reasons). First, a fractional open area was used to determine the diameter and number of outlet orifices that would maintain the same pitch ratio. Values of critical dimensions were then computed to maintain respective ratios of length to outlet orifice diameter. This naturally ensured constant ratios between critical length scales themselves.

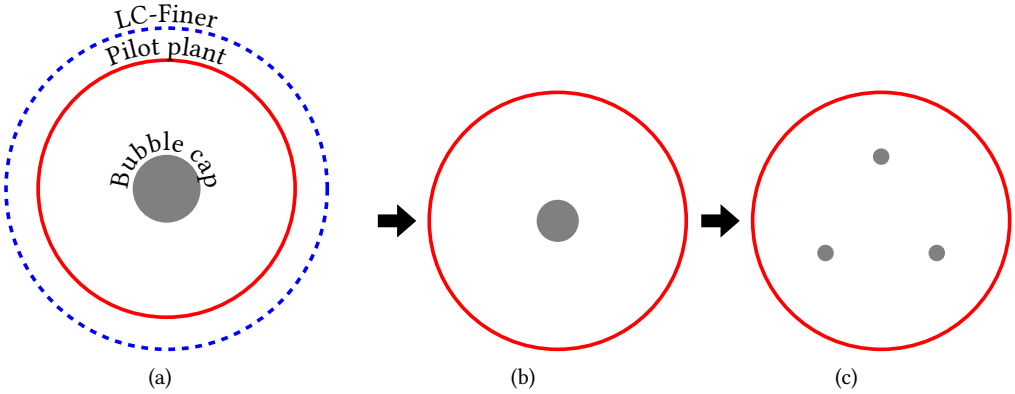

Figure 3.3: (a) Full scale bubble cap element in the laboratory unit vs. in the LC-Fining^{TM} unit; fractional opening is greater in the laboratory unit. (b) Size of the bubble cap is reduced to match fractional opening. (c) Number of elements further increased to three while maintaining fractional opening to test scaling laws.

3.3 DYNAMIC SIMILARITY

Nine parameters (ρ_l, ρ_g, μ_g, μ_l, σ, $U_{g,or}$, $U_{l,or}$, d_{or}, g), which potentially affect bubble properties and dynamics, were initially identified to evaluate dynamic similarity. Similar to Pjontek et al.,[7]

gas viscosity (μ_g) and surface tension (σ) were excluded from further analysis. Gas viscosity was excluded because it was deemed negligible (i.e., $\mu_g \ll \mu_l$). While surface tension impacts bubble size and rise velocity for pure liquid systems,[27] its use in scaling the fluid dynamics of liquids contaminated with surface-active compounds can be misleading. This is because small amounts of surface-active compounds can significantly reduce bubble rise velocity, inhibit bubble coalescence, and increase gas holdup.[28–33] The resulting change in surface tension due to the addition of surface-active compound does not always sufficiently explain the large changes in bubble properties and dynamics. Moreover, Dargar and Macchi[34] reported similar gas holdups for 0.5 and 5 wt % aqueous ethanol solution, suggesting that the effect of surfactant concentration on phase holdups ceases beyond a critical value. In this study, we employ 0.5 wt % aqueous ethanol to simulate the impact of surface-active compounds/bubble coalescence behavior.

The seven remaining parameters ($\rho_l, \rho_g, \mu_l, U_{g,or}, U_{l,or}, d_{or}$, g) were used to form four dimensionless groups (Re_l, Fr_l, $U_{g,or}/U_{l,or}$, ρ_g/ρ_l) using the Buckingham pi theorem. To further reduce degrees of freedom, $U_{g,or}/U_{l,or}$ and $Fr_l = \frac{U_{l,or}}{\sqrt{gd_{or}}}$ were combined to form $Fr_g = \frac{U_{g,or}}{\sqrt{gd_{or}}}$. The remaining dimensionless groups are shown in eqs 3.1 – 3.3.

$$Re_l = \frac{\rho_l U_{l,or} d_{or}}{\mu_l} \tag{3.1}$$

$$Fr_g = \frac{U_{g,or}}{\sqrt{g d_{or}}} \tag{3.2}$$

$$\beta_\rho = \frac{\rho_g}{\rho_l} \tag{3.3}$$

Reynolds number, which measures the relative importance of inertial to viscous forces, influences turbulent bubble breakage through the distributor. The effect of Froude number, which measures the relative importance of gas inertia to gravity, is less obvious for internal gas–liquid flows. However, Abdelsalam et al.[35] proposed a new dimensionless group known as the slippage number

for internal gas–liquid flows, defining it to be the ratio of the difference in gravitational forces between slip and no-slip conditions to the inertia of the gas. Based on the correlation developed, the slippage number exponentially decays to zero at high Froude number, with high to low values of slippage corresponding with bubble, elongated bubble, slug, churn, and annular flow, respectively. The ratio of fluids densities (ρ_g/ρ_l) accounts for pressure-induced bubble breakage. Table 3.2 shows the range of dimensionless groups investigated. Except for Re_l, there is an overlap for the values of dimensionless groups selected.

Table 3.2: Range of dimensionless groups investigated

Dimensionless Group	Single Bubble Cap	Three Bubble Caps
β_ρ	0.00137 - 0.04958	0.00137 - 0.0237
Re_l	3,883 - 13,495	1,583 - 3,534
Fr_g	1.96 - 4.46	1.67 - 4.94

3.4 EXPERIMENTAL METHODS

3.4.1 *Experimental Setup*

Experiments were performed in a stainless-steel column with an internal diameter of 0.1016 m and a height of 1.8 m. Industrial grade nitrogen supplied by Messer Group GmbH (part no. 100254) was sparged into the plenum chamber using a sintered porous pipe (10 μm pores). The liquid (0.5 wt % aqueous ethanol) was independently introduced into the plenum, where it mixed with the gas before flowing through the bubble cap risers on the gas–liquid distributor. Two geometrically similar bubble cap distributors (shown in Figure 3.4) with one and three elements were used to test the scaling laws. The gas was allowed to disengage in an expansion section connected to the top the column. The resulting liquid was then directed to a storage tank for final gas removal before it was returned to the plenum. A schematic of the experimental unit is shown in Figure 3.5. Table 3.3 summarizes the experimental conditions investigated. The selected operating conditions span the dispersed bubble flow regime only (U_G < 0.05 m/s), where the impact of gas–liquid distributor

is most significant. Furthermore, the selected operating pressures are lower than the industrial value ($\sim$ 11.7 MPa), and this is justified because the impact of pressure on bubble properties and dynamics was determined in Mach et al.[36] to level off around 2 MPa.

Table 3.3: Summary of Experimental Conditions Investigated

Operation condition	Single bubble cap plate	Three bubble cap plate
Gas superficial velocity (m/s)	0.02, 0.03, 0.04	0.01, 0.03
Liquid superficial velocity (m/s)	0.01, 0.02, 0.03	0.01, 0.02
Pressure (MPa)	0.10, 0.50, 2.00, 4.00	0.10, 2.00
Temperature(K)	297	297
Number of elements	1	3
Outlet orifices per bubble cap	2	4
Outlet orifice diameter (mm)	12.2	5.0

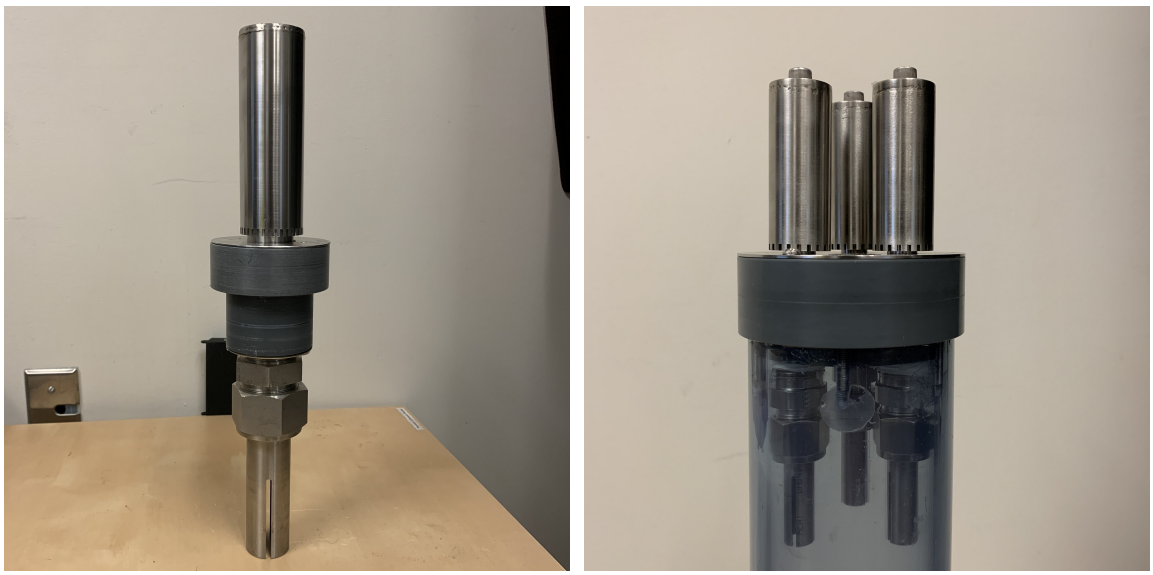

(a) single bubble cap plate (b) Three bubble cap plate

Figure 3.4: Pictures of single bubble cap and three bubble cap plates.

3.4.2 *Instrumental Techniques*

A differential pressure transducer manufactured by ABB Inc. (Model no. 266DSHHHSA2A1/V1E4L5) was used to obtain axial pressure profiles. Assuming wall frictional losses and vertical phase

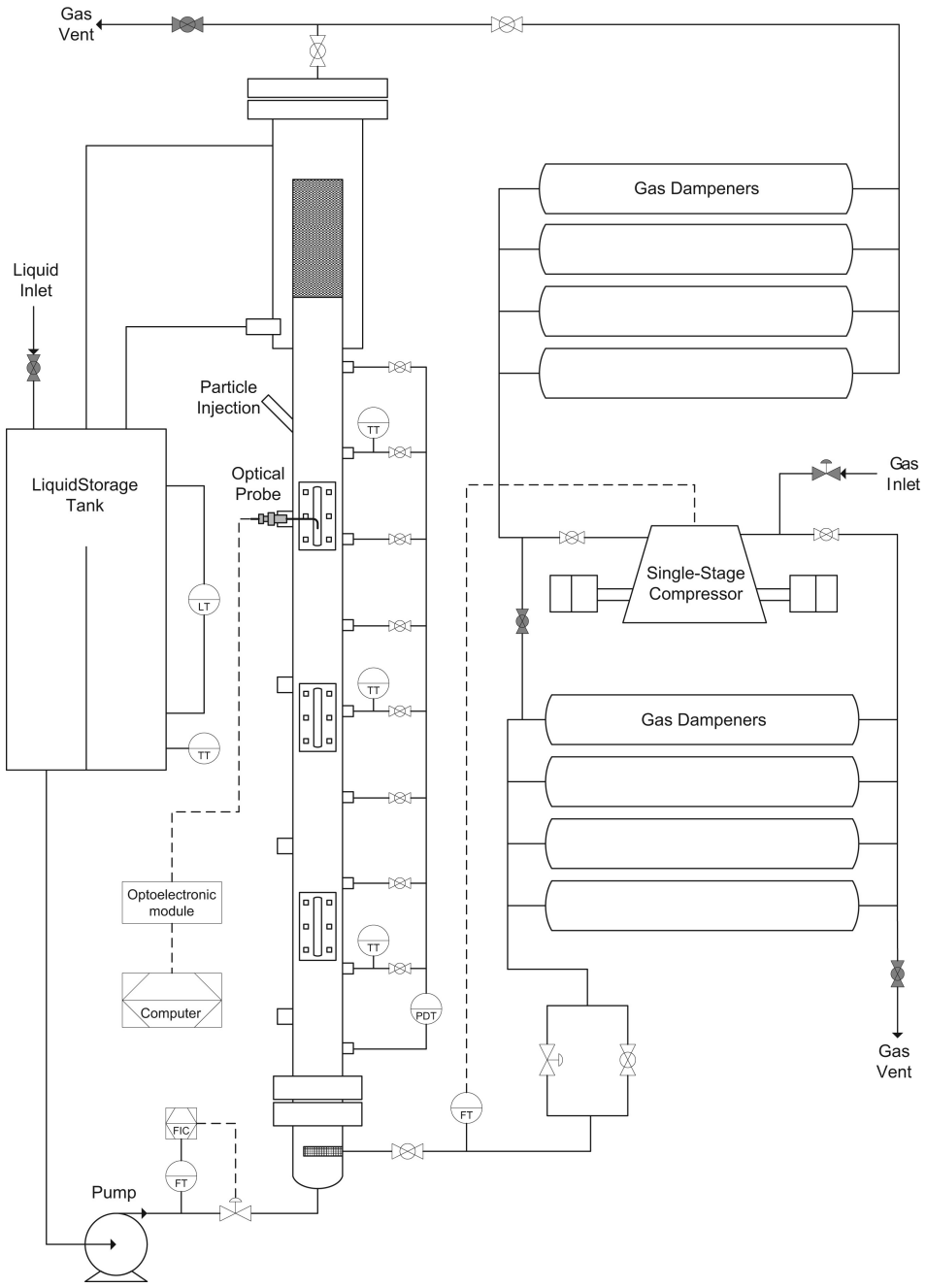

Figure 3.5: A schematic of the experimental unit. (reprinted with permission from Pjontek et al.[6] Copyright 2014 Elsevier Ltd).

acceleration are negligible, the measured dynamic pressure loss can be related to the overall gas holdup through eq 3.4.

$$\varepsilon_g = -\frac{dP/dz}{g\left(\rho_l - \rho_g\right)} \tag{3.4}$$

A custom 1C–3C monofibre optical probe manufactured by A2 Photonics Sensors was used to measure bubble chord lengths ($c_{br,i}$) and rise velocities ($u_{br,i}$). The probe was positioned 0.6 m above the distributor. Guan and Yang[37] demonstrated with tap water that the radial gas holdup profile is fully developed above a height of 0.6 and 0.2 m in the homogeneous and heterogeneous flow regimes, respectively. Camarasa et al.[16] reported negligible changes in bubble size and shape with height beyond the initial point of bubble formation for a liquid contaminated with surface-active compound, conditions which are relevant to this study. Our own measurements of axial pressure profile (for determining overall gas holdup) indicated a linear trend, suggesting a steady bubble rise and negligible changes in bubble properties with height. At each operating condition, measurements were taken at 5 radial locations (r/R = 0, 0.2, 0.4, 0.6, 0.8) to determine the cross-sectional mean of measured properties. The probe relies on the difference in the refractive index of the gas and the liquid. An optoelectronic module sends a monochromatic light (λ = 830 nm) through an optical fibre to the tip of the probe. When the tip is immersed in a bubble, more light is reflected since the gas has a higher index. The reflected light is converted to a voltage signal and analyzed for signal rise time $t_{R,i}$ and bubble residence time $t_{b,i}$. Together with the probe sensing length (L_s = 23.2 μm) provided by the manufacturer, these two parameters are used to determine bubble rise velocity (eq 3.5) and bubble chord length (eq 3.6). A lower and upper threshold of 10 and 80%, respectively, were set for the calculation of signal rise time as recommended by the manufacturer. Data was sampled at 200 kHz for 180 seconds or until 10,000 bubbles were detected. Probe signal was acquired three times, for each condition, to ensure results were repeatable. Data was recorded when the relative difference to the mean between readings was less than 5%. Equations 3.7 – 3.9, 3.10, and 3.11 show the calculation of the cross-sectional mean of measured bubble sizes and rise velocities, respectively. Equation 3.12, by Wellek et al.[38] was used to account for the bubble aspect ratio in the conversion of chord length to diameter.

$$u_{br,i} = \frac{L_s}{t_{R,i}} \tag{3.5}$$

$$c_{br,i} = u_{br,i}.t_{b,i} \tag{3.6}$$

$$c_{br} = \frac{\sum_i c_{br,i}}{n_{br}} \tag{3.7}$$

$$d_{br} = \frac{3}{2} c_{br} E^{-2/3} \tag{3.8}$$

$$d_b = \left(\frac{\int_0^R d_{br}^3 n_{br} 2\pi r dr}{\int_0^R n_{br} 2\pi r dr} \right)^{1/3} \tag{3.9}$$

$$u_{br} = \frac{\sum_i u_{br,i}}{n_{br}} \tag{3.10}$$

$$U_b = \frac{\int_0^R u_{br} d_{br}^3 n_{br} 2\pi r dr}{\int_0^R d_{br}^3 n_{br} 2\pi r dr} \tag{3.11}$$

$$E = \frac{1}{1 + 0.163 Eo^{0.757}} \tag{3.12}$$

The accuracy of the probe has been addressed by a few studies and three effects (blinding, drifting, and crawling) were identified as the cause of uncertainty in measured local gas holdups;[39–41] local gas holdup is not interpreted in this study for this reason. Parisien et al.[42] validated bubble rise velocities and chord lengths measured by the current generation (1C–3C) of the optical probe against pressure signals gathered during gas disengagement experiments.

3.5 RESULTS AND DISCUSSION

3.5.1 *Effects of Dimensionless Groups on Global Bubble Properties*

Figure 3.6 shows the effects of the dimensionless groups (Fr_g, Re_l, and ρ_g/ρ_l) on the overall gas holdup. The dimensionless groups were based on the operating conditions of the single bubble

cap plate outlined in Table 3.3. Gas Froude number (Fr_g) and liquid Reynolds number (Re_l) were respectively varied through the gas and liquid superficial velocities, while the gas–liquid density ratio (ρ_g/ρ_l) was varied through the operating pressure. In Figure 3.6a, the overall gas holdup significantly increases with gas Froude number and slightly decreases with the liquid Reynolds number. In Figure 3.6b, the impact of the gas–liquid density ratio is marginal.

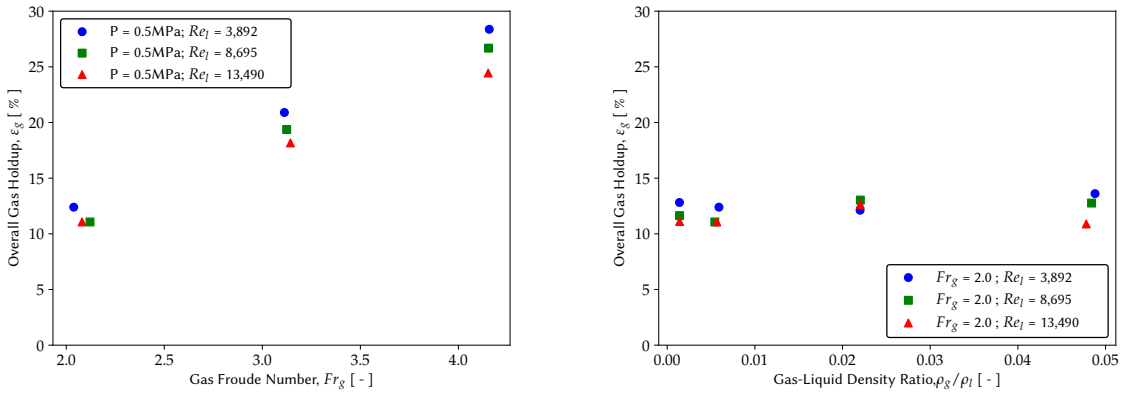

(a) (b)

Figure 3.6: Variation of overall gas holdup with (a) gas Froude and liquid Reynolds numbers and (b) gas–liquid density ratio. Dimensionless groups based on single bubble cap plate operating conditions outlined in Table 3.3.

Generally, the variation of the overall gas holdup is linked to gas phase residence time, which is dependent on bubble size and bubble rise velocity. Operating conditions and gas–liquid distributor, together, alter resulting bubble sizes and their rise velocities, consequently affecting overall gas holdup. Figures 3.7 and 3.8, respectively, show the effects of the dimensionless groups/operating conditions on the mean bubble diameter and rise velocity. Both gas Froude number and liquid Reynolds number have a significant impact on mean bubble diameter (Figure 3.7a), but their impact on mean bubble rise velocity is negligible (Figure 3.8a). The effect of gas Froude number/gas velocity on overall gas holdup in Figure 3.6a is thus largely due to the increased bubble population (gas volume). The effect of Reynolds number/liquid velocity is two-fold: (i) it enhances bubble breakage at the distributor due to increased continuous phase turbulence and (ii) it imparts additional momentum on the gas phase – the former results in smaller bubbles with lower slip velocities,

and depending on these slip velocities, the latter can increase rise velocities and consequently decrease gas residence time. For microbubbles, the additional momentum marginally decreases gas residence time, lowering gas holdup as shown in Figure 3.6a and as reported by Parisien et al.[42] For larger bubbles, the reduction in size and slip velocity is more dominant than the additional momentum from the liquid, resulting in higher gas holdups with an increase in Reynolds number/liquid velocity.[25]

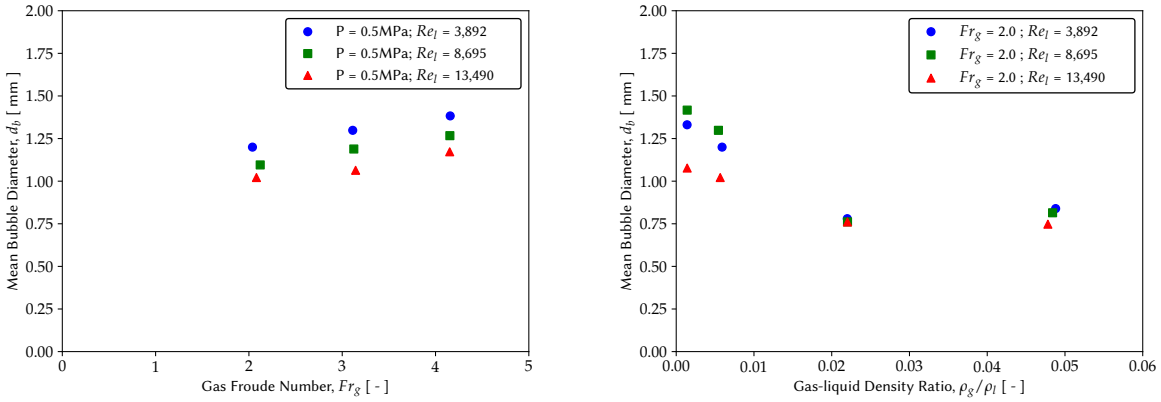

(a) (b)

Figure 3.7: Variation of mean bubble diameter with (a) gas Froude and liquid Reynolds numbers and (b) gas-liquid density ratio. Dimensionless groups based on single bubble cap plate operating conditions outlined in Table 3.3.

The effect of gas–liquid density ratio (pressure) on mean bubble diameter and mean bubble rise velocity shown in Figures 3.7b and 3.8b, respectively, is due to Kelvin–Helmholtz instability and internal circulation within bubbles. Wilkinson et al.[4] argued that external disturbances acting on a bubble induce breakage if their wavelengths are greater than some critical value. This critical wavelength decreases with gas density resulting in enhanced bubble breakage at elevated pressures. Levich[43] argued that internal circulation within a bubble exerts a force toward the gas–liquid interface. This force counterbalances external disturbances and restorative surface forces, but its magnitude increases with gas density, eventually overcoming these counteracting forces and

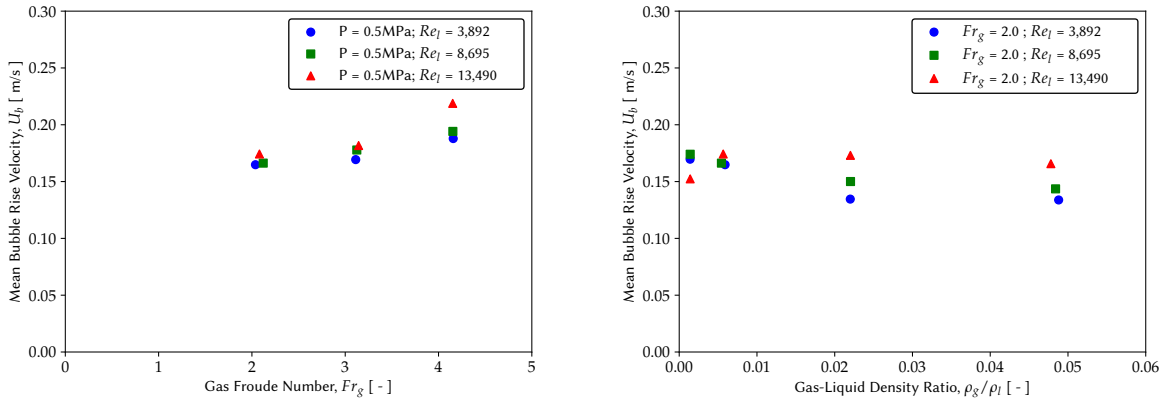

(a) (b)

Figure 3.8: Variation of mean bubble rise velocity with (a) gas Froude and liquid Reynolds numbers and (b) gas-liquid density ratio. Dimensionless groups based on single bubble cap plate operating conditions outlined in Table 3.3.

causing the bubble to split. Both mechanisms are believed to contribute to bubble breakage by pressure, albeit in different proportions.

3.5.2 *Chord Length Distributions*

Initial data exploration suggested that chord lengths detected by the probe follow log-normal distribution. Therefore, maximum likelihood estimates of log-normal distribution parameters (μ and s) were extracted for all operating conditions. Equation 3.13 defines the probability density function of a log-normal distribution. The distribution parameters are defined in eqs 3.14 and 3.15, where m_r and v_r are the mean and variance of a number distribution at a given radial position, respectively. Column-wide parameters (μ, s) were obtained by number and area averaging radial parameters (μ_r, s_r); see eqs 3.16 and 3.17. As shown in eq 3.15, s_r and by extension s is made non-dimensional by normalizing variance (v_r) with the square of mean (m_r^2). We render μ_r and μ dimensionless in eqs 3.18–3.20 using outlet orifice diameter, d_{or}. Both μ^* and s will be correlated with aforementioned dimensionless groups to (i) enable the prediction of resulting chord length

distribution and (ii) to facilitate the comparison of single and three bubble cap plates for testing scaling laws.

$$P\left(c_{bi}\right) = \frac{1}{s\, c_{bi}\sqrt{2\,\pi}} exp\left[-\frac{\left(log\left(c_{bi}\right)-\mu\right)^2}{2\,s^2}\right] \tag{3.13}$$

$$\mu_r = log\left(\frac{m_r^2}{\sqrt{v_r + m_r^2}}\right) = log\left(\frac{m_r}{\sqrt{\frac{v_r}{m_r^2}+1}}\right) \tag{3.14}$$

$$s_r = \sqrt{log\left(\frac{v_r}{m_r^2}+1\right)} \tag{3.15}$$

$$\mu = \frac{\int_0^R \mu_r\, n_{br}\, 2\pi r dr}{\int_0^R n_{br}\, 2\pi r dr} \tag{3.16}$$

$$s = \frac{\int_0^R s_r\, n_{br}\, 2\pi r dr}{\int_0^R n_{br}\, 2\pi r dr} \tag{3.17}$$

$$\mu_r^* = log\left(\frac{m_r}{d_{or}\sqrt{\frac{v_r}{m_r^2}+1}}\right) = \mu_r - log(d_{or}) \tag{3.18}$$

$$\mu^* = \frac{\int_0^R \mu_r^*\, n_{br}\, 2\pi r dr}{\int_0^R n_{br}\, 2\pi r dr} = \frac{\int_0^R \mu_r\, n_{br}\, 2\pi r dr}{\int_0^R n_{br}\, 2\pi r dr} - log\left(d_{or}\right) \tag{3.19}$$

$$\mu^* = \mu - log\left(d_{or}\right) \tag{3.20}$$

Figures 3.9 – 3.11 compare fitted probability and cumulative density functions to some experimental data obtained with a single bubble cap plate. Generally, the log-normal distribution is a good fit. Dimensionless distribution parameters were then correlated with ρ_g/ρ_l, Re_l, and Fr_g via eqs 3.21 and 3.22. Correlation coefficients between natural logarithms of dimensionless groups are shown in Table 3.4. The highest coefficient is only 0.097, suggesting low collinearity between the groups, which is in line with obtaining independent groups via dimensional analysis. Fitted model

parameters and their 95% confidence intervals using a variance estimate from the mean squared residuals are shown in Table 3.5 along with their respective p-values. Figure 3.12 shows parity plots for (a) μ^* and (b) s. Both μ^* and s correlated fairly well with the three groups. As expected, distribution parameters decrease with Re_l and ρ_g/ρ_l, but increase with Fr_g.

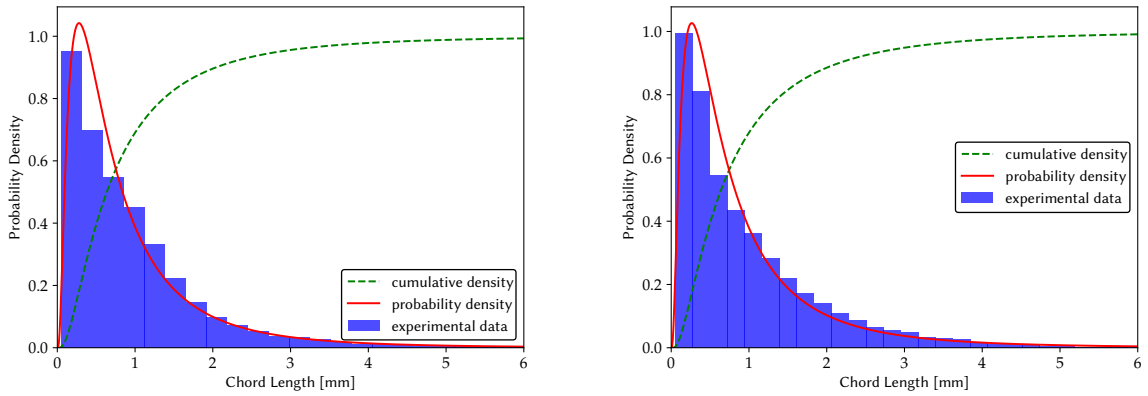

Figure 3.9: CLD for various Froude numbers at low pressure ($\rho_g/\rho_l = 0.0014$, $Re_l = 3892$) a) $Fr_g = 2.0$ b) $Fr_g = 4.0$. Dimensionless groups based on single bubble cap plate operating conditions outlined in Table 3.3.

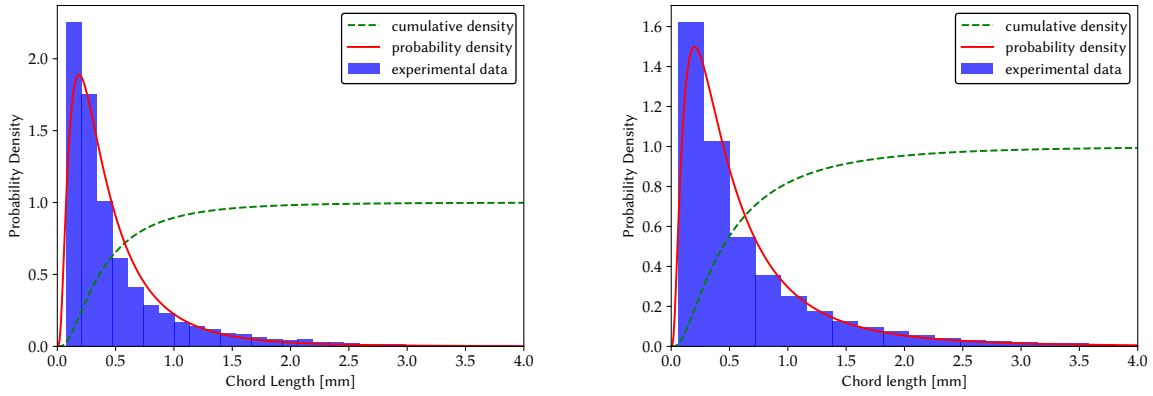

Figure 3.10: CLD for various Froude numbers at high pressure ($\rho_g/\rho_l = 0.048$, $Re_l = 3892$) a) $Fr_g = 2.0$ b) $Fr_g = 4.0$. Dimensionless groups based on single bubble cap plate operating conditions outlined in Table 3.3.

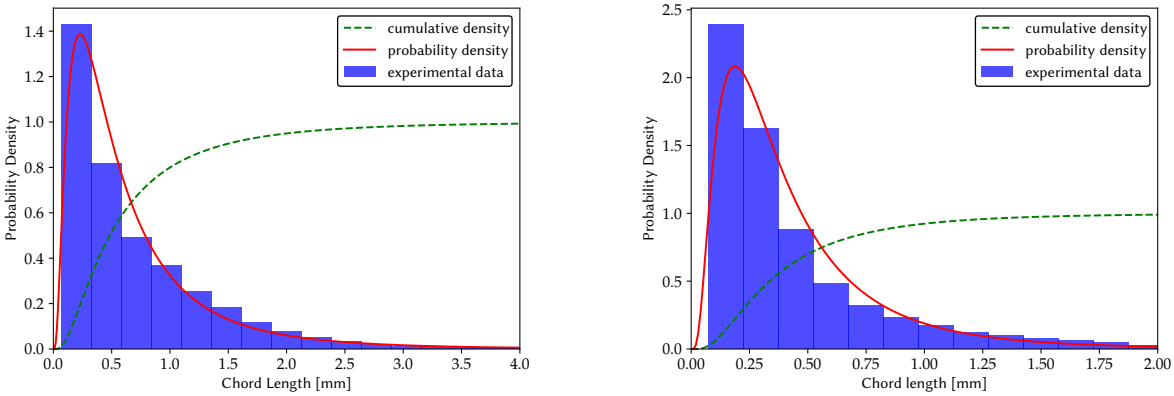

(a) (b)

Figure 3.11: CLD at higher Re_l ($Fr_g = 2.0$, $Re_l = 13,490$) a) $\rho_g/\rho_l = 0.0014$ b) $\rho_g/\rho_l = 0.048$. Dimensionless groups based on single bubble cap plate operating conditions outlined in Table 3.3.

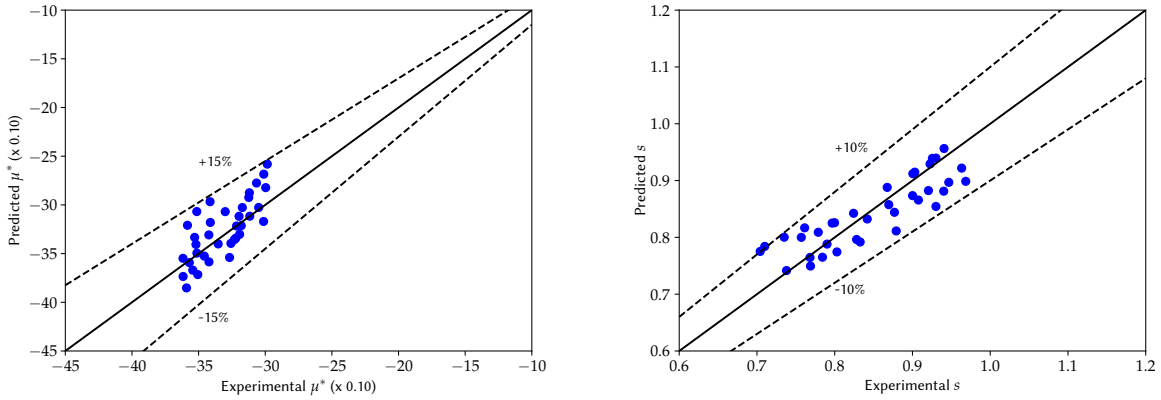

(a) (b)

Figure 3.12: Parity plots for a) μ^* and b) s

Table 3.4: Correlation coefficients between dimensionless groups

	$log(\rho_g/\rho_l)$	$log(Re_l)$	$log(Fr_g)$
$log(\rho_g/\rho_l)$	1	0.097	0.049
$log(Re_l)$	0.097	1	0.018
$log(Fr_g)$	0.049	0.018	1

$$\mu^* = \beta_1 + \beta_2 \, log\left(\frac{\rho_g}{\rho_l}\right) + \beta_3 \, log\left(Re_l\right) + \beta_4 \, log\left(Fr_g\right) \tag{3.21}$$

$$s = \beta_1 + \beta_2 \, log\left(\frac{\rho_g}{\rho_l}\right) + \beta_3 \, log\left(Re_l\right) + \beta_4 \, log\left(Fr_g\right) \tag{3.22}$$

Table 3.5: Estimated model parameters for μ^* and s (see equation 3.21 and 3.22)

Parameter	μ^*		s	
	value	p-value	value	p-value
β_1	-0.5305 $\pm$ 0.039	0.00	0.7594 $\pm$ 0.091	0.00
β_2	-0.1469 $\pm$ 0.000	0.00	-0.0426 $\pm$ 0.005	0.00
β_3	-0.4229 $\pm$ 0.000	0.00	-0.0201 $\pm$ 0.010	0.04
β_4	0.3450 $\pm$ 0.000	0.00	0.0596 $\pm$ 0.019	0.00
General Statistics				
R^2	0.69		0.75	
$AARE$	0.066		0.037	
F_m	1.09		1.09	

3.5.3 *Effects of Gas-liquid Distributor Geometry*

To test scaling laws, we compare results obtained with single and three bubble cap plates. This comparison also assesses the effect of number of elements. The comparison is achieved through the use of models developed for the single bubble cap plate and formulated in eqs 3.21 and 3.22. Both distributors have similar open areas, but different number of elements and outlet orifices. Moreover, the single bubble cap plate has larger orifice diameters than the three bubble cap plate. Despite these differences, ratios of various critical length scales matched for the two distributors. As mentioned previously, there was a good overlap of dimensionless groups except for Re_l. Considering that Re_l influences bubble breakage and that the values of Re_l for the three bubble cap plate are lower than those of the single bubble cap plate, larger dimensionless bubble sizes should be expected from the three bubble cap plate. Table 3.6 shows results obtained with the three bubble cap plate, while Figure 3.13a and 3.13b compares distribution parameters to model predicted values at similar dimensionless groups.

Table 3.6: Results for three bubble cap distributor

Pressure [MPa]	$U_l[m/s]$	$U_g[m/s]$	ρ_g/ρ_l	Re_l	Fr_g	$\varepsilon_g[\%]$	$d_b[mm]$
0.10	0.01	0.01	0.00137	1583	1.67	7.04	1.347
	0.01	0.03	0.00137	1583	4.94	22.23	1.348
	0.02	0.01	0.00137	3534	1.67	7.05	1.214
	0.02	0.03	0.00137	3534	4.94	22.32	1.148
2.00	0.01	0.01	0.02370	1583	1.67	7.20	0.834
	0.01	0.03	0.02370	1583	4.94	24.61	0.956
	0.02	0.01	0.02370	3534	1.67	7.22	0.739
	0.02	0.03	0.02370	3534	4.94	25.69	0.784

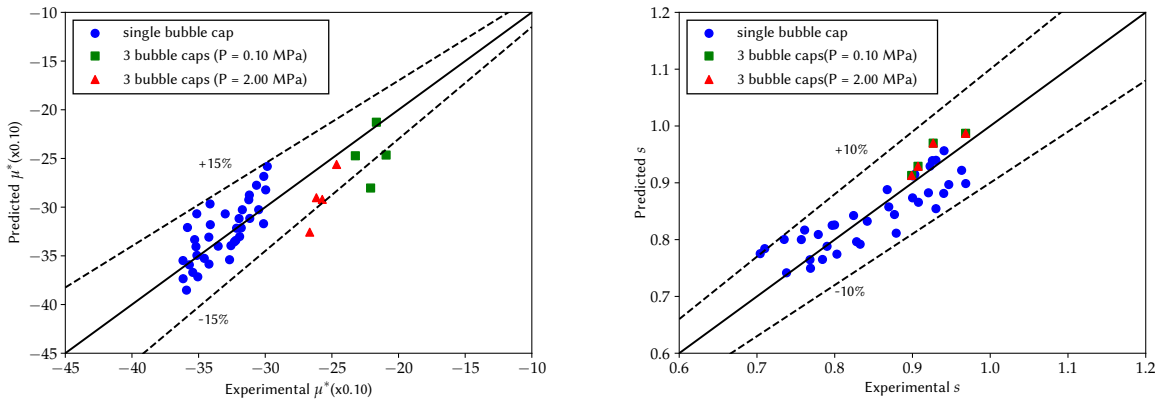

(a) (b)

Figure 3.13: Comparison of single and three bubble cap plates through distribution parameters, a) μ^* b) s

In Figure 3.13a, we see that larger bubbles were indeed recorded for the three bubble cap plate since its values of Re_l were lower. At matching dimensionless groups, the model developed with the single bubble cap plate slightly under-predicts μ^* and overpredicts s (Fig. 3.13b). The discrepancy on μ^* is more pronounced at low pressure and high Re_l/ liquid velocities, while the discrepancy on s is fairly consistent at all operating conditions. The discrepancy on μ^* points to possible bubble coalescence at the exit of three bubble cap plate for two reasons: (i) gas-liquid dispersions from individual bubble caps radially jet farther outwards at higher liquid velocities and could momentarily collide with each other before changing direction; this interaction could lead to bubble coalescence, and (ii) larger bubbles are generally formed at low pressure which enhances chances for bubble coalescence. The two effects act synergistically to compound the difference. Despite

this, the scaling approach works better at elevated pressure (i.e close to industrial conditions) since smaller bubbles are formed.

Scaling based on normalizing μ with the outlet orifice diameter has worked for d_{or} ranging from 5 mm to 12.2 mm, with the outlet orifice diameter of the industrial distributor being typically a few millimeters greater. The dynamics of gas-liquid distributors fundamentally differ from those of single phase distributors. Single phase distributors predominantly involve bubble formation at the outlet of individual orifices, whereas gas-liquid distributors promote simultaneous bubble breakage and coalescence. While bubble size and resulting holdup from single phase distributors can be fairly constant beyond some critical orifice diameter,[4] this is unlikely the case for the two-phase bubble cap distributor due to (i) sudden changes in magnitude and direction of fluids velocities and (ii) simultaneous bubble breakage and coalescence under elevated dispersed phase holdups.

Our previous work[36] demonstrated that the drag coefficient of an individual bubble in a contaminated polydisperse swarm decreases with pressure at constant gas holdup. This observation was attributed to changes in bubble size distribution caused by pressure. As pressure increased, the bubble size distribution shifted towards smaller sizes. These smaller bubbles, relatively speaking, induce marginal liquid perturbations and could dampen turbulence originating from other sources, resulting in reduced drag. Here, we perform a similar analysis to confirm the effect of gas-liquid distributor on bubble drag. Figures 3.14 – 3.16 show the variation of chord length distribution and individual drag coefficient with pressure for U_g = 0.02 - 0.04 m/s and U_l = 0.03 m/s.

Generally, the mean drag coefficient of a given bubble class decreases with increasing pressure for a given gas velocity. The chord length distribution also shifts towards smaller values with increasing pressure as determined in our previous work. A similar drag model (eq. 3.23) was then adopted to correlate this data. Correlation coefficients between various explanatory variables are shown in Table 3.7, where the highest correlation occurs between $Re_b.Eo$ and p'/Eo due to

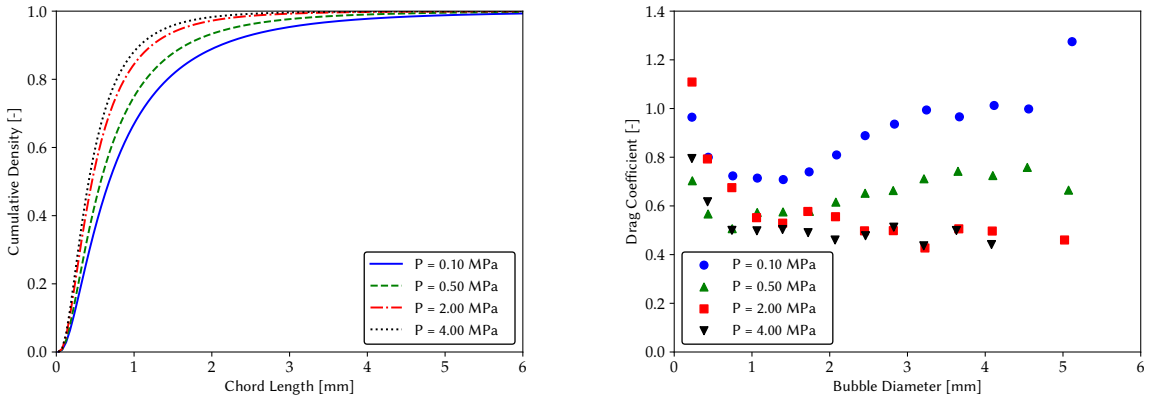

(a) (b)

Figure 3.14: (a) Chord length distributions and (b) individual drag coefficients at various pressures (U_g = 0.02 m/s, U_l = 0.03 m/s)

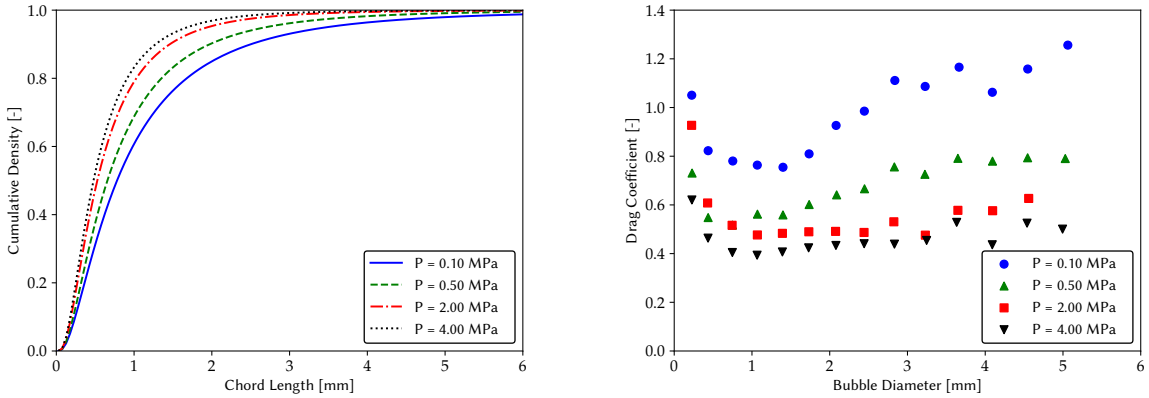

(a) (b)

Figure 3.15: (a) Chord length distributions and (b) individual drag coefficients at various pressures (U_g = 0.03 m/s, U_l = 0.03 m/s)

shared variable (Eo). The inclusion of Eo in both explanatory variables was deemed necessary to account for the effect of bubble size and shape on single isolated bubble drag and swarm correction factor. Single isolated bubble drag has been shown to depend on both Re_b and Eo.[44] As can be seen in Figures 3.14 – 3.16, the effect of pressure on the drag coefficient depends on bubble size. The dimensionless pressure (p') was thus normalized by Eo to better capture this effect. Estimated model parameters for a single bubble cap plate are compared to those of a perforated plate from our previous work[36] in Table 3.8. Figure 3.17 compares model predicted drag coefficients

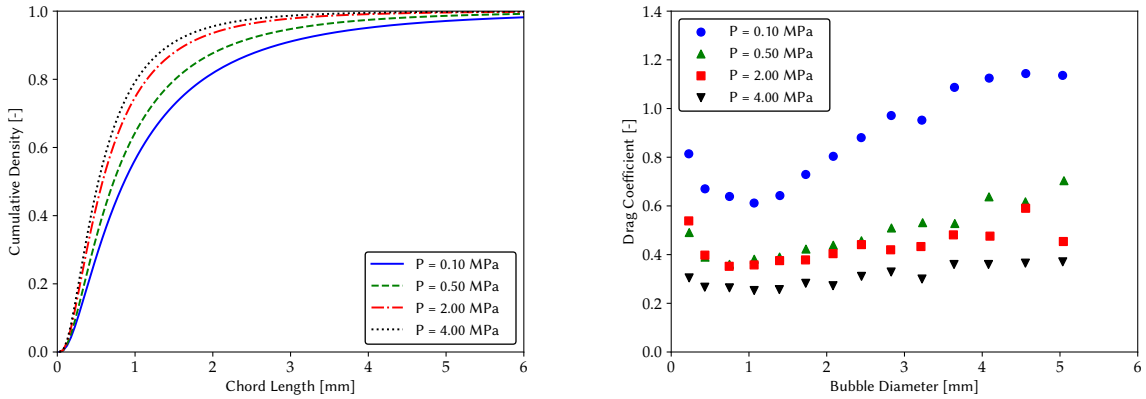

(a) (b)

Figure 3.16: (a) Chord length distributions and (b) individual drag coefficients at various pressures (U_g = 0.04 m/s, U_l = 0.03 m/s)

to their corresponding experimental values. For both gas-liquid distributors, β_1 is fairly similar. However, values of β_2 and β_3 differ, suggesting that the geometry of the gas-liquid distributor influences bubble drag. Based on model parameters, bubbles produced by a single bubble cap plate tend to be more hindered than those produced by a perforated plate. Similar to the effect of pressure on bubble drag, the effect of distributor geometry is through bubble size distribution. The bubble cap distributor produces larger bubbles than the perforated plate distributor due to possible re-coalescence inside the riser and bubble cap.[25]

$$C_{D,i} = \frac{24}{Re_b}\left[1 + (Re_b.Eo)^{\beta_1}\right].\left[1-\varepsilon_g\right]^{\beta_2\left[1-exp\left(\frac{\beta_3.p'}{Eo}\right)\right]} \tag{3.23}$$

Table 3.7: Correlation coefficients between explanatory variables

	$Re_b.Eo$	ε_g	p'/Eo
$Re_b.Eo$	1	0.112	-0.236
ε_g	0.112	1	0.050
p'/Eo	-0.236	0.050	1

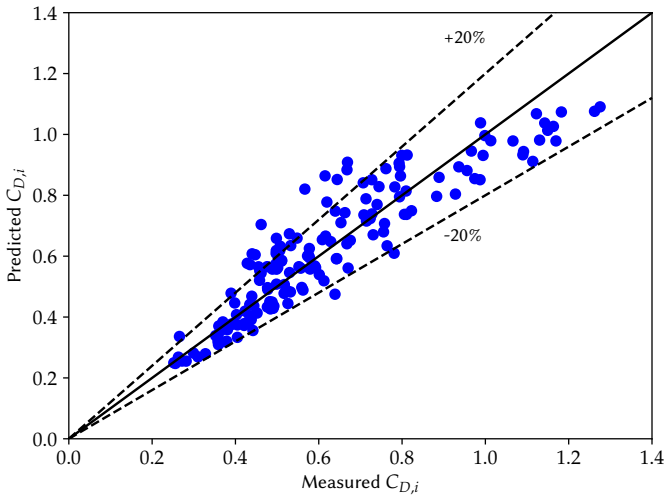

Figure 3.17: Parity plot for the drag model obtained with bubble cap data

Table 3.8: Parameters for drag model

Parameter	Perforated Plate		Bubble Cap	
	value	p-value	value	p-value
β_1	0.42 $\pm$ 0.00	0.00	0.47 $\pm$ 0.00	0.00
β_2	3.96 $\pm$ 0.22	0.00	2.46 $\pm$ 0.12	0.00
β_3	-0.07 $\pm$ 0.01	0.00	-0.13 $\pm$ 0.02	0.00
General Statistics				
R^2	0.84		0.87	
$AARE$	0.20		0.12	
F_m	1.05		1.055	

3.6 CONCLUSION

This study aimed to develop and experimentally validate scaling laws for a gas-liquid distributor used in an ebullated bed hydroprocessor. The geometric scale down of the distributor was based on first matching the fractional open area, followed by matching ratios of various critical dimensions. Three dimensionless groups (gas-liquid density ratio, liquid Reynolds number and gas Froude number) were determined through Buckingham pi theorem and subsequent reduction. In addition to these dimensionless groups, bubble coalescence behaviour was considered. Measured bubble properties correlated well to the three dimensionless groups for a nitrogen-0.5wt.% aqueous

ethanol system. To test the scaling laws, two geometrically similar distributors with different number of bubble cap elements were compared. At atmospheric conditions, similar chord length distribution parameters were observed for both distributors except at higher liquid velocities. The slight discrepancy can be attributed to interactions, caused by radially oriented jets, between gas-liquid dispersions emerging from multiple bubble caps. A better agreement was observed at elevated pressures for low and high liquid velocities, suggesting that the scaling approach works at industrially relevant conditions. Further analysis of the data collected with single bubble cap plate showed that the gas-liquid distributor also influences the drag on an individual bubble in a contaminated polydisperse swarm. This effect is attributed to bubble size distribution generated by the gas-liquid distributor. Bubbles produced by the single bubble cap plate were found to be more hindered than those produced by a perforated plate since the former produced larger bubbles.

ACKNOWLEDGEMENTS

The authors thank Stephane Gluck and Nicolas Zuanon of A2 Photonic Sensors for their technical support. The authors also thank Syncrude Canada Ltd., Natural Sciences and Engineering Research Council (NSERC), and Ontario's Ministry of Colleges and Universities for financial assistance.

NOMENCLATURE

Ar_{l-s}	Archimedes number
β_d	solid-liquid density ratio
β_i	model parameters, $i = 1, 2, 3, ...$
β_ρ	gas-liquid density ratio
β_U	gas-liquid velocity ratio
$c_{br,i}$	individual bubble chord length, m

$c_{b,i}$	mean bubble chord for a given class, m
c_{br}	local mean chord length, m
CLD	Chord Length Distribution
$C_{D,i}$	Drag coefficient of a bubble in a swarm
d_{br}	local mean bubble diameter, m
d_b	global mean bubble diameter, m
d_{or}	outlet orifice diameter, m
d_p	particle diameter, m
dP	differential pressure, Pa
d_{sv}	Sauter mean particle diameter, m
d_v	volume mean particle diameter, m
dz	axial distance between pressure taps, m
ε_g	overall gas holdup, $m^3_{bubble}/m^3_{reactor}$
E	bubble aspect ratio
Eo	Eötvös number
Fr_g	gas Froude number
g	gravitational acceleration, m/s^2
L_s	probe's sensing length, μm
μ_g	gas viscosity, $Pa.s$
$P(c_{b,i})$	probability density of a bubble with chord length, $c_{b,i}$
μ_r	local log mean of bubble chord lengths, m
μ_r^*	dimensionless local log mean of bubble chord lengths
μ	global log mean of bubble chord lengths, m
μ^*	dimensionless global log mean of bubble chord lengths
m_r	local mean of bubble chord lengths, m
s_r	local log standard deviation of bubble chord lengths
s	global log standard deviation of bubble chord lengths

v_r	local variance of bubble chord lengths, m^2
μ_l	liquid viscosity, $Pa.s$
Mo	Morton's number
n_{br}	number of bubbles at a given radial position
p'	dimensionless pressure
ρ_g	gas density, kgm^{-3}
ρ_l	liquid density, kgm^{-3}
ρ_s	solid density, kgm^{-3}
Re_b	bubble Reynolds number
Re_l	liquid Reynolds number
Re_{l-s}	liquid-solid Reynolds number
σ	surface tension, N/m
$t_{b,i}$	bubble residence time, ms
t_T	total measurement time, s
$t_{R,i}$	signal rise time, ms
$u_{br,i}$	individual bubble rise velocity, m/s
u_{br}	mean rise velocity at a given radial position, m/s
U_b	global mean rise velocity, m/s
U_g	column-based superficial gas velocity, m/s
$U_{g,or}$	orifice-based superficial gas velocity, m/s
U_l	column-based superficial liquid velocity, m/s
$U_{l,or}$	orifice-based superficial liquid velocity, m/s

REFERENCES

[1] James G Speight. *Heavy and extra-heavy oil upgrading technologies*. Gulf Professional Publishing, 2013. ISBN 0124017479.

[2] Craig A. McKnight, Larry P. Hackman, John R. Grace, Arturo Macchi, Darwin Kiel, and Jonathan Tyler. Fluid Dynamic Studies in Support of an Industrial Three-Phase Fluidized Bed Hydroprocessor. *Can. J. Chem. Eng.*, 81(3-4):338–350, jun 2008. ISSN 0008-4034. doi: 10.1002/cjce.5450810302.

[3] R. S. Ruiz, F. Alonso, and J. Ancheyta. Effect of high pressure operation on overall phase holdups in ebullated-bed reactors. *Catal. Today*, 98(1-2 SPEC. ISS.):265–271, 2004. ISSN 09205861. doi: 10.1016/j.cattod.2004.07.039.

[4] Peter M. Wilkinson, Arie P. Spek, and Laurent L. van Dierendonck. Design parameters estimation for scale-up of high-pressure bubble columns. *AIChE J.*, 38(4):544–554, 1992. ISSN 15475905. doi: 10.1002/aic.690380408.

[5] K. Malysa, M. Krasowska, and M. Krzan. Influence of surface active substances on bubble motion and collision with various interfaces. *Adv. Colloid Interface Sci.*, 114-115:205–225, 2005. ISSN 00018686. doi: 10.1016/j.cis.2004.08.004.

[6] Dominic Pjontek, Valois Parisien, and Arturo Macchi. Bubble characteristics measured using a monofibre optical probe in a bubble column and freeboard region under high gas holdup conditions. *Chem. Eng. Sci.*, 111:153–169, 2014. ISSN 00092509. doi: 10.1016/j.ces.2014.02.024.

[7] Dominic Pjontek, Craig A. McKnight, Jason Wiens, and Arturo Macchi. Ebullated bed fluid dynamics relevant to industrial hydroprocessing. *Chem. Eng. Sci.*, 126:730–744, 2015. ISSN 00092509. doi: 10.1016/j.ces.2015.01.002.

[8] Mike Safoniuk, John R. Grace, Larry Hackman, and Craig A. McKnight. Use of dimensional similitude for scale-up of hydrodynamics in three-phase fluidized beds. *Chem. Eng. Sci.*, 54 (21):4961–4966, 1999. ISSN 00092509. doi: 10.1016/S0009-2509(99)00218-3.

[9] Arturo Macchi, Hsiaotao Bi, John R. Grace, Craig A. McKnight, and Larry Hackman. Dimensional hydrodynamic similitude in three-phase fluidized beds. *Chem. Eng. Sci.*, 56(21-22): 6039–6045, 2001. ISSN 00092509. doi: 10.1016/S0009-2509(01)00207-X.

[10] Arturo Macchi, Hsiaotao Bi, John R. Grace, Craig A. McKnight, and Larry Hackman. Effect of Gas Density on the Hydrodynamics of Bubble Columns and Three-Phase Fluidized Beds. *Can. J. Chem. Eng.*, 81(3-4):846–852, jun 2008. ISSN 0008-4034. doi: 10.1002/cjce.5450810368.

[11] Fereshteh Rahimpour, Reza Zarghami, and Navid Mostoufi. Effect of distributor on fluidized bed hydrodynamics. *Can. J. Chem. Eng.*, 95(11):2221–2234, 2017. ISSN 1939019X. doi: 10.1002/cjce.22895.

[12] Safa Sharaf, Maria Zednikova, Marek C. Ruzicka, and Barry J. Azzopardi. Global and local hydrodynamics of bubble columns - Effect of gas distributor. *Chem. Eng. J.*, 288:489–504, 2016. ISSN 13858947. doi: 10.1016/j.cej.2015.11.106.

[13] Anand V. Kulkarni and Jyeshtharaj B. Joshi. Design and selection of sparger for bubble column reactor. Part I: Performance of different spargers. *Chem. Eng. Res. Des.*, 89(10):1972–1985, 2011. ISSN 02638762. doi: 10.1016/j.cherd.2011.01.004.

[14] Anand V. Kulkarni and Jyeshtharaj B. Joshi. Design and selection of sparger for bubble column reactor. Part II: Optimum sparger type and design. *Chem. Eng. Res. Des.*, 89(10):1986–1995, oct 2011. ISSN 02638762. doi: 10.1016/j.cherd.2011.01.014.

[15] C. J.P. Ouyang and G. B. Tatterson. The Effect of Distributors on Two-Phase and Three-Phase Flows in Vertical Columns. *Chem. Eng. Commun.*, 49(4-6):197–215, 1987. ISSN 15635201. doi: 10.1080/00986448708911803.

[16] E. Camarasa, C. Vial, S. Poncin, G. Wild, N. Midoux, and J. Bouillard. Influence of coalescence behaviour of the liquid and of gas sparging on hydrodynamics and bubble characteristics in a bubble column. *Chem. Eng. Process. Process Intensif.*, 38(4-6):329–344, 1999. ISSN 02552701. doi: 10.1016/S0255-2701(99)00024-0.

[17] Bimal Gandhi, Anand Prakash, and Maurice A. Bergougnou. Effects of sparger height and orifice orientation on solids dispersion in a slurry bubble column. *Can. J. Chem. Eng.*, 77(2): 383–391, apr 1999. ISSN 00084034. doi: 10.1002/cjce.5450770226.

[18] Lu Han and Muthanna H. Al-Dahhan. Gas-liquid mass transfer in a high pressure bubble column reactor with different sparger designs. *Chem. Eng. Sci.*, 62(1-2):131–139, jan 2007. ISSN 00092509. doi: 10.1016/j.ces.2006.08.010.

[19] Giorgio Besagni, Lorenzo Gallazzini, and Fabio Inzoli. Effect of gas sparger design on bubble column hydrodynamics using pure and binary liquid phases. *Chem. Eng. Sci.*, 176:116–126, feb 2018. ISSN 00092509. doi: 10.1016/j.ces.2017.10.036.

[20] Dale D. McClure, Congcong Wang, John M. Kavanagh, David F. Fletcher, and Geoffrey W. Barton. Experimental investigation into the impact of sparger design on bubble columns at high superficial velocities. *Chem. Eng. Res. Des.*, 106:205–213, feb 2016. ISSN 02638762. doi: 10.1016/j.cherd.2015.12.027.

[21] Claudio Alimonti, Gioia Falcone, and Oladele Bello. Two-phase flow characteristics in multiple orifice valves. *Exp. Therm. Fluid Sci.*, 34(8):1324–1333, 2010. ISSN 08941777. doi: 10.1016/j.expthermflusci.2010.06.004.

[22] Ammar Zeghloul, Abdelwahid Azzi, Faiza Saidj, Barry J. Azzopardi, and Buddhika Hewakandamby. Interrogating the effect of an orifice on the upward two-phase gas-liquid flow behavior. *Int. J. Multiph. Flow*, 74:96–105, 2015. ISSN 03019322. doi: 10.1016/j.ijmultiphaseflow.2015.04.013.

[23] Ammar Zeghloul, Abdelwahid Azzi, Faiza Saidj, Abdelkader Messilem, and Barry James Azzopardi. Pressure Drop Through Orifices for Single- and Two-Phase Vertically Upward Flow - Implication for Metering. *J. Fluids Eng. Trans. ASME*, 139(3):1–12, 2017. ISSN 1528901X. doi: 10.1115/1.4034758.

[24] Ammar Zeghloul, Abdelwahid Azzi, Abbas Hasan, and Barry James Azzopardi. Behavior and pressure drop of an upwardly two-phase flow through multi-hole orifices. *Proc. Inst. Mech. Eng. Part C J. Mech. Eng. Sci.*, 232(18):3281–3299, 2018. ISSN 20412983. doi: 10.1177/0954406217736081.

[25] Jacob Mach, Valois Parisien, Jason Wiens, Craig A. McKnight, and Arturo Macchi. Impact of plenum conditions and gas-liquid distributor on bubble column hydrodynamics. *Chem. Eng. Sci.*, 211:115296, 2020. ISSN 00092509. doi: 10.1016/j.ces.2019.115296.

[26] James H. Colvert. Bubble cap assembly in an ebullated bed reactor, 1989.

[27] Amol A. Kulkarni and Jyeshtharaj B. Joshi. Bubble formation and bubble rise velocity in gas-liquid systems: A review. *Ind. Eng. Chem. Res.*, 44(16):5873–5931, aug 2005. ISSN 08885885. doi: 10.1021/ie049131p.

[28] Shu Takagi and Yoichiro Matsumoto. Surfactant Effects on Bubble Motion and Bubbly Flows. *Annual Review of Fluid Mechanics*, 43(1):615–636, 2011. ISSN 0066-4189. doi: 10.1146/annurev-fluid-122109-160756.

[29] Dimitrina S. Valkovska and Ivan B. Ivanov. Effect of surfactants on the film drainage. *Journal of Colloid and Interface Science*, 211(2):291–303, 1999. ISSN 00219797. doi: 10.1006/jcis.1998.5973.

[30] R. Bel Fdhila and P. C. Duineveld. The effect of surfactant on the rise of a spherical bubble at high Reynolds and Peclet numbers. *Physics of Fluids*, 8(2):310–321, 1996. ISSN 10706631. doi: 10.1063/1.868787.

[31] M. Jamialahmadi and H. Müller-Steinhagen. Effect of alcohol, organic acid and potassium chloride concentration on bubble size, bubble rise velocity and gas hold-up in bubble columns. *The Chemical Engineering Journal*, 50(1):47–56, 1992. ISSN 03009467. doi: 10.1016/0300-9467(92)80005-U.

[32] Weihua Li and Nivedita R. Gupta. Buoyancy-Driven Motion of Bubbles in the Presence of Soluble Surfactants in a Newtonian Fluid. *Industrial and Engineering Chemistry Research*, 58 (18):7640–7649, 2019. ISSN 15205045. doi: 10.1021/acs.iecr.8b04788.

[33] Sayantan Samanta and Pallab Ghosh. Coalescence of bubbles and stability of foams in brij surfactant systems. *Industrial and Engineering Chemistry Research*, 50(8):4484–4493, 2011. ISSN 08885885. doi: 10.1021/ie102396v.

[34] Puneet Dargar and Arturo Macchi. Effect of surface-active agents on the phase holdups of three-phase fluidized beds. *Chem. Eng. Process. Process Intensif.*, 45(9):764–772, 2006. ISSN 02552701. doi: 10.1016/j.cep.2006.03.004.

[35] Alsarkhi Abdelsalam, Sarica Cem, and Pereyra Eduardo. New dimensionless number for gas-liquid flow in pipes. *Int. J. Multiph. Flow*, 81:15–19, 2016. ISSN 03019322. doi: 10.1016/j.ijmultiphaseflow.2015.12.008.

[36] Jacob Mach, Jason Wiens, John Adjaye, Adam A. Donaldson, and Arturo Macchi. Effect of pressure on the drag coefficient of individual bubbles in a contaminated polydisperse swarm. *Chem. Eng. Sci.*, 223:115728, 2020. ISSN 00092509. doi: 10.1016/j.ces.2020.115728.

[37] Xiaoping Guan and Ning Yang. Bubble properties measurement in bubble columns: From homogeneous to heterogeneous regime. *Chem. Eng. Res. Des.*, 127(1999):103–112, 2017. ISSN 02638762. doi: 10.1016/j.cherd.2017.09.017.

[38] R. M. Wellek, A. K. Agrawal, and A. H.P. Skelland. Shape of liquid drops moving in liquid media. *AIChE J.*, 12(5):854–862, 1966. ISSN 15475905. doi: 10.1002/aic.690120506.

[39] E. Barrau, N. Rivière, Ch Poupot, and A. Cartellier. Single and double optical probes in air-water two-phase flows: Real time signal processing and sensor performance. *Int. J. Multiph. Flow*, 25(2):229–256, mar 1999. ISSN 03019322. doi: 10.1016/S0301-9322(98)00042-1.

[40] Alain Cartellier. Optical probes for multiphase flow characterization: Some recent improvements. *Chem. Eng. Technol.*, 24(5):535–538, may 2001. ISSN 09307516. doi: 10.1002/1521-4125(200105)24:5<535::AID-CEAT535>3.0.CO;2-X.

[41] J. Enrique Juliá, Wouter K. Harteveld, Robert F. Mudde, and Harrie E.A. Van Den Akker. On the accuracy of the void fraction measurements using optical probes in bubbly flows. *Review of Scientific Instruments*, 76(3), 2005. ISSN 00346748. doi: 10.1063/1.1862192.

[42] Valois Parisien, Alixia Farrell, Dominic Pjontek, Craig A. McKnight, Jason Wiens, and Arturo Macchi. Bubble swarm characteristics in a bubble column under high gas holdup conditions. *Chem. Eng. Sci.*, 157:88–98, jan 2017. ISSN 00092509. doi: 10.1016/j.ces.2016.04.051.

[43] Veniamin G Levich. *Physiochemical Hydrodynamics*. Prentice Hall, Engelwood Cliffs, NJ, 1962.

[44] Akio Tomiyama, Isao Kataoka, Iztok Zun, and Tadashi Sakaguchi. Drag coefficients of single bubbles under normal and micro gravity conditions. *JSME Int. Journal, Ser. B Fluids Therm. Eng.*, 41(2):472–479, 1998. ISSN 13408054. doi: 10.1299/jsmeb.41.472.

4

EFFECT OF PRESSURE ON THE DRAG COEFFICIENT OF INDIVIDUAL BUBBLES IN A CONTAMINATED POLYDISPERSE SWARM

ABSTRACT

This study investigated the effect of pressure on individual bubble drag for a contaminated polydisperse swarm. Bubble size distributions and individual bubble drag coefficients were experimentally determined at four different pressures (0.14, 0.46, 2.00, 4.00 MPa) to establish if there is a relationship between bubble size distribution and individual drag coefficient and quantify the effect of pressure on bubble drag. The analysis is limited to bubbles with diameters between 0.4 and 6 mm. Individual bubble drag coefficients were found to decrease with pressure at constant gas hold-up. This effect is attributed to changes in bubble size distribution driven by pressure. As pressure increased, the bubble size distribution shifted towards smaller sizes. Relatively speaking, these smaller bubbles induce marginal liquid perturbations and could potentially dampen turbulence from other sources, resulting in reduced drag. A new drag model has been proposed to improve CFD simulation of bubble columns at elevated pressures.[1]

1 This chapter has been published in Chemical Engineering Science: doi.org/10.1016/j.ces.2020.115728

4.1 INTRODUCTION

Drag is an important force in gas-liquid flows since it contributes to bubble rise and residence time, which in turn govern mass transfer and performance of bubble column reactors. Several studies have been conducted to understand and review the effects of various factors (e.g. phase properties, shape, size, bubble population and surface contamination) on bubble drag.[1–10] However, there are fewer studies on the effect of pressure on individual bubbles in a swarm. It has been shown that pressure enhances bubble breakage, through a combination of Kelvin-Helmholtz instability and internal circulation, shifting bubble size distribution towards smaller sizes.[11,12] Relatively speaking, these smaller bubbles induce marginal fluctuations in the liquid flow field and could potentially dampen turbulence from other sources (e.g. wall-induced turbulence and large scale buoyancy driven flows), resulting in reduced drag.[13–17]

To our knowledge, there are only three studies in open literature on the effect of pressure on the drag coefficient of individual bubbles in a swarm.[18–20] Both works of Yan et al.[20] and Yang et al.[19] are based on Computational Fluid Dynamic (CFD) simulation of bubble columns at pressure and propose new swarm correction factors that incorporate the effect of pressure through the volume fraction of small and large bubbles. Yang et al.[19] identified a diameter of 10 mm as the demarcation between small and large bubbles but pointed out that the value is based on pure liquid systems, making its applicability to contaminated liquids limited. Lane et al.[18] experimentally investigated the effect of swarm on 0.1–10 mm diameter bubbles for overall gas hold-ups ranging from 10 to 37 % at pressures of 0.1 and 6.5 MPa. At 0.1 MPa, their rise velocities were relatively well predicted by the single bubble drag model of Tomiyama et al.[1] and the swarm correction factor of Lockett and Kirkpatrick.[7] At 6.5 MPa, the swarm correction factor was not required as the single bubble drag model provided a better approximation for the measured rise velocities, suggesting that the effect of swarm decreases with pressure.

A new experimental design is proposed to isolate the effect of pressure by controlling liquid superficial velocity, gas holdup and bubble size. Our analysis is limited to bubbles with diameters between 0.4 and 6 mm. Bubble size distributions and individual bubble drag coefficients are determined at four different pressures (0.14, 0.46, 2.00, and 4.00 MPa) to (i) determine if there is a relationship between bubble size distribution and individual bubble drag coefficient, and (ii) to quantify the effect of pressure on the drag coefficient.

4.2 EXPERIMENTAL METHODS

4.2.1 *Experimental Setup*

Experiments were performed in a stainless-steel column with an internal diameter of 0.10 m and a height of 1.80 m. Nitrogen was delivered into the plenum chamber of the column using a sintered porous pipe (10 μm in diameter pores), with the resulting gas-liquid mixture allowed to pass through a perforated plate with 23 holes, each with an inner diameter of 3.2 mm. An expansion section at the top of the column allowed the gas to disengage from the liquid. The residual liquid was then directed to a storage tank for final gas-liquid separation before the liquid was returned to the plenum. A schematic of the experimental unit is shown in Fig. 4.1.

The gas phase consisted of industrial grade nitrogen supplied by Messer Group GmbH (part #: 100254). A liquid made of 0.5 wt.% ethanol in tap water was used (i) to simulate a surfactant contaminated system, (ii) to inhibit bubble coalescence, and (iii) to maintain a polydisperse bubble swarm generated by the gas-liquid distributor. Liquid superficial velocity was maintained at 0.03 m/s for all runs to control wall-induced turbulence. Gas superficial velocity was then varied to achieve gas holdups ranging from 10 to 34%. Experiments were conducted at four different pressures of 0.14, 0.46, 2.00, and 4.00 MPa. The operating temperature was 302 K. A summary of all experimental conditions can be found in Table 4.1.

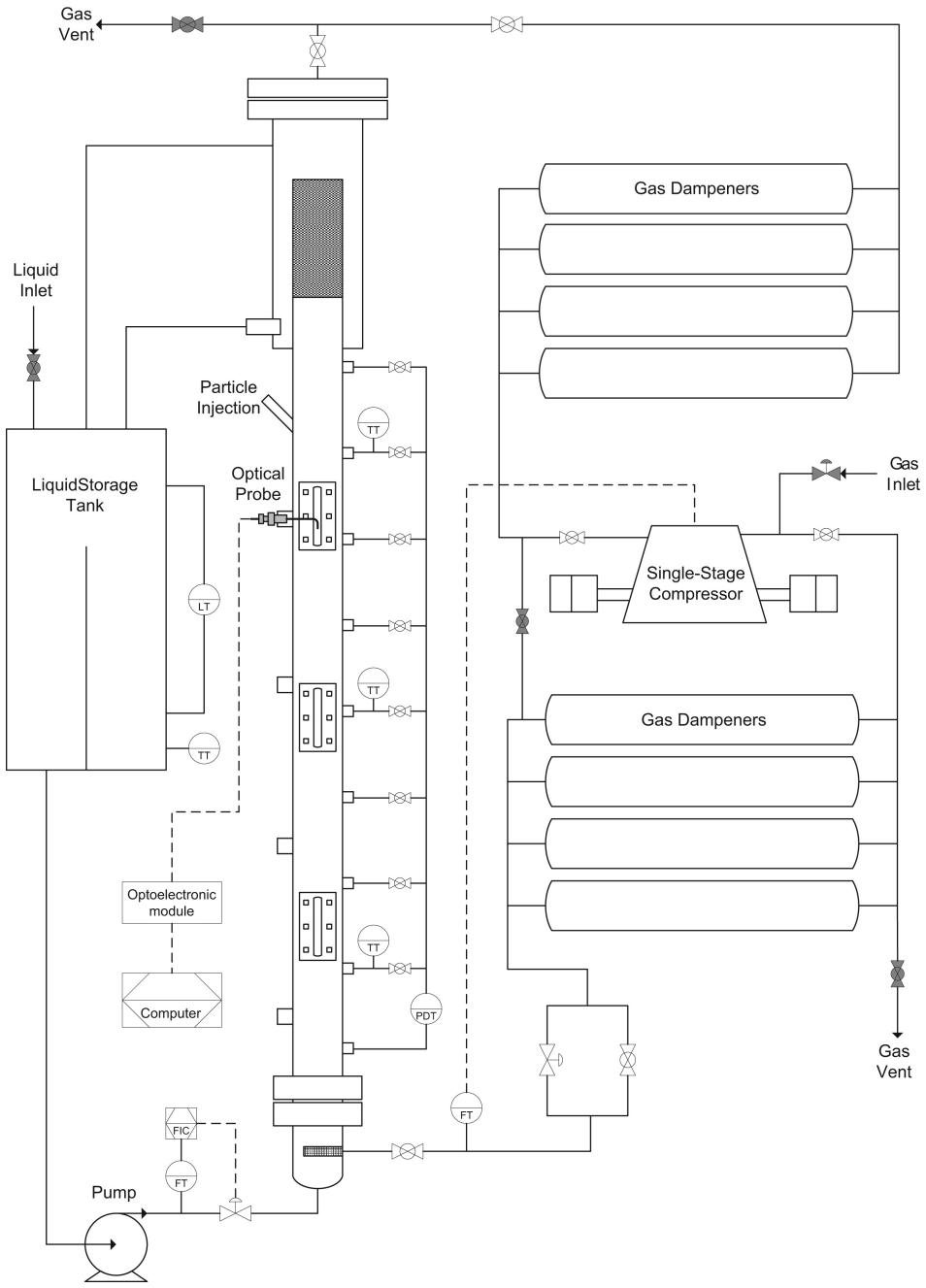

Figure 4.1: Schematic of experimental system.[21]

4.2.2 *Instrumental Techniques*

A differential pressure transducer manufactured by ABB Inc. (Model #: 266DSHHHSA2A1V1E4L5) was used to obtain axial pressure profile. Measurements were taken at four pressure ports located 0.39, 0.68, 0.97, and 1.12 m above the perforated plate. The reference port was located 0.10 m above

Table 4.1: Summary of experimental conditions

Pressure [MPa]	U_L [m/s]	U_G [m/s]	Gas holdup [%]	Fully detected bubbles
0.14	0.03	0.011	9.18	27 167
		0.021	17.83	44 514
		0.031	27.13	71 256
		0.041	33.49	74 705
0.46	0.03	0.011	10.15	19 792
		0.018	18.97	43 527
		0.026	24.20	67 434
		0.038	32.41	70 703
2.00	0.03	0.010	9.80	15 612
		0.017	18.70	47 083
		0.026	26.41	61 977
		0.035	33.08	63 709
4.00	0.03	0.008	10.35	13 111
		0.016	19.42	45 835
		0.026	27.88	61 292
		0.034	34.20	62 868

the perforated plate. Assuming wall frictional losses and phase acceleration are negligible, the measured dynamic pressure loss can be related to the gas hold-up as shown in Eq. 4.1, where $-dP/dz$, ρ_L, ρ_G and g are the slope of axial pressure profile, liquid density, gas density, and gravitational acceleration, respectively. Linearity of axial pressure profile was used to confirm uniformity of axial gas holdup profile and steady bubble rise.

$$\varepsilon_G = \frac{-dP/dz}{(\rho_L - \rho_G)g} \tag{4.1}$$

A custom 1C-3C mono-fibre optical probe manufactured by A2 Photonics Sensors was used to measure bubble chord lengths $c_{br,i}$ and rise velocities $u_{br,i}$. The probe was positioned 1.02 m above the perforated plate to minimize the effect of turbulence generated at the inlet. At each operating condition, measurements were taken at 9 radial locations (r/R = -0.80 to 0.80, 0.20 increments). The probe relies on the difference in refractive index of the gas and the liquid. An optoelectronic module sends a monochromatic light (λ = 830 nm) through an optical fibre to the tip of probe.

When the tip is immersed in a bubble, more light is reflected since the gas has a higher index. The reflected light is converted to a voltage signal and analysed for signal rise time $t_{R,i}$ and bubble residence time $t_{b,i}$. A lower and upper threshold of 10 and 80%, respectively, were set for the calculation of signal rise time as recommended by the manufacturer. Data was sampled at 200 kHz for 180 s or until 10,000 bubbles were detected. A typical signal is shown in Fig. 4.2. At each radial location, optical probe signal was acquired three times. This was done for all operating conditions. The final replicate was stored if the average relative errors associated with the rise velocity and chord length were less than 5%. In all cases, the average relative error was less than 5%.

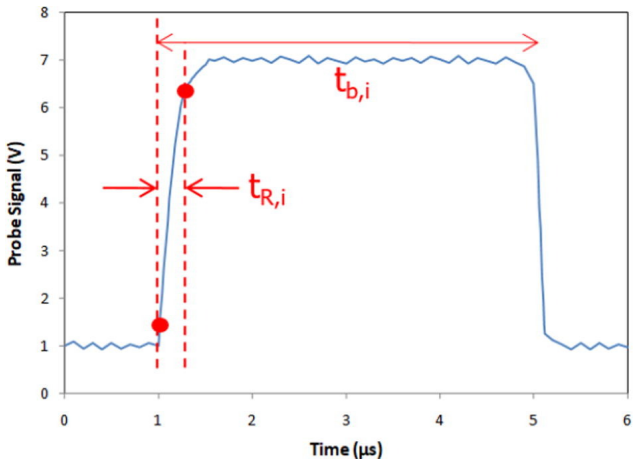

Figure 4.2: Typical probe signal

As shown in Eq. 4.2, the rise velocity of an individual bubble is calculated from the signal rise time and probe sensing length $L_s = 23.2\,\mu m$, provided by the manufacturer. The chord length is determined from the rise velocity and bubble residence time as shown in Eq. 4.3.

$$u_{br,i} = \frac{L_s}{t_{R,i}} \tag{4.2}$$

$$c_{br,i} = u_{br,i}.t_{b,i} \tag{4.3}$$

The accuracy of the probe has been addressed by other studies and three effects (blinding, drifting and crawling) were identified as the cause of uncertainty in measured local gas holdups;[22–24] the

local gas holdup was not used in our analysis for this reason. A validation of bubble rise velocity and chord length can be found in Parisien et al.[21]

4.2.3 *Data Analysis*

In total, 790,585 bubbles were fully detected by the probe for all operating conditions in Table 4.1. For each gas holdup, bubbles measured at a given radial position were grouped into 14 bubble size classes of 0.20 mm interval, with the smallest and largest chord lengths being 0.20 and 3.0 mm, respectively. Rise velocities and chord lengths in each of those classes were then number-averaged as shown in Eq. 4.4, 4.5, respectively. Eq. 4.6 shows the conversion of a local bubble chord length $\overline{c_{br,i}}$, within each class, to a local volume equivalent diameter $\overline{d_{br,i}}$. Eq. 4.7 is the widely used aspect ratio E model of Wellek et al.,[25] while Eq. 4.8 defines the dimensionless Eötvös number Eo; both are inputs to Eq. 4.6 and account for bubble shape. To get global means in each class, various values of $\overline{u_{br,i}}$ and $\overline{d_{br,i}}$ are further averaged as shown in Eq. 4.9, 4.10, respectively. The average drag coefficient $C^*_{D,i}$ within an individual bubble class was calculated as shown in Eq. 4.11, which is derived from a force balance on an individual bubble in a swarm.[18] Eq. 4.12 was used to calculate slip velocity $U_{s,i}$ from average rise velocity and interstitial liquid velocity $U_L/(1-\varepsilon_G)$.

$$\overline{u}_{br,i} = \frac{\sum_i u_{br,i}}{n_{br,i}} \tag{4.4}$$

$$\overline{c}_{br,i} = \frac{\sum_i c_{br,i}}{n_{br,i}} \tag{4.5}$$

$$\overline{d}_{br,i} = \frac{3}{2}\,\overline{c}_{br,i}\,E^{-2/3} \tag{4.6}$$

$$E = \frac{1}{1+0.163Eo^{0.757}} \tag{4.7}$$

$$Eo = \frac{(\rho_L - \rho_G)\, g \bar{d}_{br,i}^2}{\sigma} \tag{4.8}$$

$$U_{b,i} = \frac{\int_r \overline{u}_{br,i}\, n_{br,i}\, \bar{d}_{br,i}^3\, 2\pi r dr}{\int_r n_{br,i}\, \bar{d}_{br,i}^3\, 2\pi r dr} \tag{4.9}$$

$$d_{b,i} = \left(\frac{\int_r \bar{d}_{br,i}^3\, n_{br,i}\, 2\pi r dr}{\int_r n_{br,i}\, 2\pi r dr} \right)^{1/3} \tag{4.10}$$

$$C_{D,i}^* = \frac{4}{3} \frac{(\rho_L - \rho_G)}{\rho_L} g d_{b,i} E^{\frac{2}{3}} \frac{1}{U_{s,i}^2} \tag{4.11}$$

$$U_{s,i} = U_{b,i} - \frac{U_L}{1 - \varepsilon_G} \tag{4.12}$$

4.3 DIMINISHING EFFECT OF BUBBLE SWARM WITH PRESSURE

Fig. 4.3 shows cumulative distribution of bubble chord lengths at various pressures and gas holdups. For all gas holdups, the distribution shifts towards smaller sizes as pressure increases. This observation can be explained with the help of Kelvin-Helmholtz instability and internal circulation theory. Wilkinson et al.[11] reported that disturbances at bubble interface whose wavelengths exceed some critical value cause bubble breakage. This critical wavelength decreases with pressure, resulting in enhanced bubble breakage at elevated pressures. Levich[12] suggested that internal circulation inside the bubble exerts centrifugal force towards the gas-liquid interface. This force stabilizes the bubble against external disturbances, but its magnitude increases with pressure, eventually overcoming restorative surface forces and causing the bubble to split. The internal circulation is reported to be largely responsible for the decrease in maximum stable diameter with pressure. This could also be true for spherical-cap bubbles in contaminated systems since

surfactants adhering to the interface are sheared off as the bubble rises.

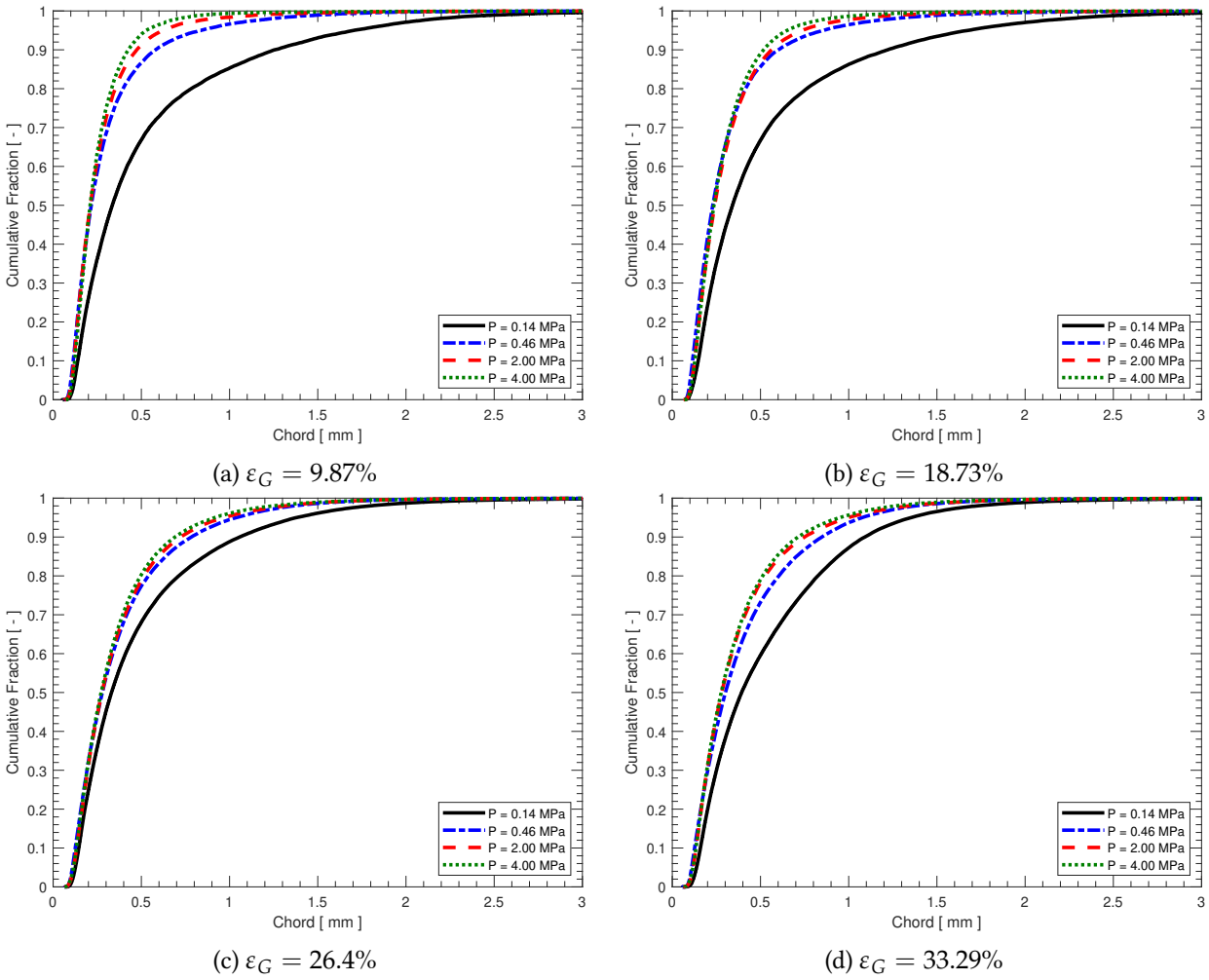

(a) $\varepsilon_G = 9.87\%$ (b) $\varepsilon_G = 18.73\%$

(c) $\varepsilon_G = 26.4\%$ (d) $\varepsilon_G = 33.29\%$

Figure 4.3: Cumulative distribution of chord lengths at various gas hold-ups and pressures. Distribution shifts towards smaller bubbles with increasing pressure.

Fig. 4.4 shows average drag coefficients of individual bubble classes at various gas holdups and pressures. Generally, the average drag coefficient decreases with increasing pressure for a given bubble class and gas holdup. Fig. 4.5 shows the rise velocities of individual bubble classes at three radial positions and four different pressures. At any radial position, the rise velocity of an individual bubble class increases with pressure, suggesting that the observed drag reduction in Fig. 4.4 does not arise from radial averaging. This drag reduction is due to changes in bubble size distribution caused by pressure. As can be seen in Fig. 4.3, the bubble size distribution shifts towards smaller

sizes with an increase in pressure. These smaller bubbles not only induce little to no agitation in the continuous phase but can also dampen turbulence from other sources. Ghatage et al.[26] and Doroodchi et al.[27] discuss the impact of continuous phase turbulence on settling of solid particles and rise of bubbles. They found an increase in continuous phase turbulence hinders the motion of solids and bubbles, which implies that the dampening of continuous phase turbulence by increasing number of smaller bubbles at elevated pressures could be responsible for the observed drag reduction. It is worth noting that the bubble size distribution (Fig. 4.3) and individual bubble drag coefficients (Fig. 4.4) remain fairly constant above a pressure of 2.0 MPa, which further confirms that the effect of pressure on bubble drag is through bubble size distribution.

Figure 4.6 provides the variation of drag coefficient $C^*_{D,i}$ and polydispersity index *PDI* with gas holdup at 0.14 and 0.46 MPa. It can be seen that $C^*_{D,i}$ and *PDI* vary in the same direction at both pressures. Equation (4.13) defines *PDI*, where *PDI* greater than unity signifies broad size distribution and *PDI* equal to unity signifies uniform size distribution. As shown in Figure 4.6, PDI also decreases with increasing pressure. This suggests that swarm polydispersity could also be responsible for the observed variation of drag with pressure and gas holdup. McClure et al.[28] and Rabha and Buwa[29] also reported similar observations, where the swarm correction factor decreased with gas holdup for polydisperse swarms at atmospheric conditions.

$$PDI = \frac{< c^2_{br,i} >}{< c_{br,i} >^2} \tag{4.13}$$

4.4 A NEW CORRELATION INCORPORATING THE EFFECT OF PRESSURE

Section 3.3 demonstrated the impact of pressure on the drag coefficient of individual bubbles in a swarm. In this section, the goal is to develop a new empirical correlation that includes the effect of

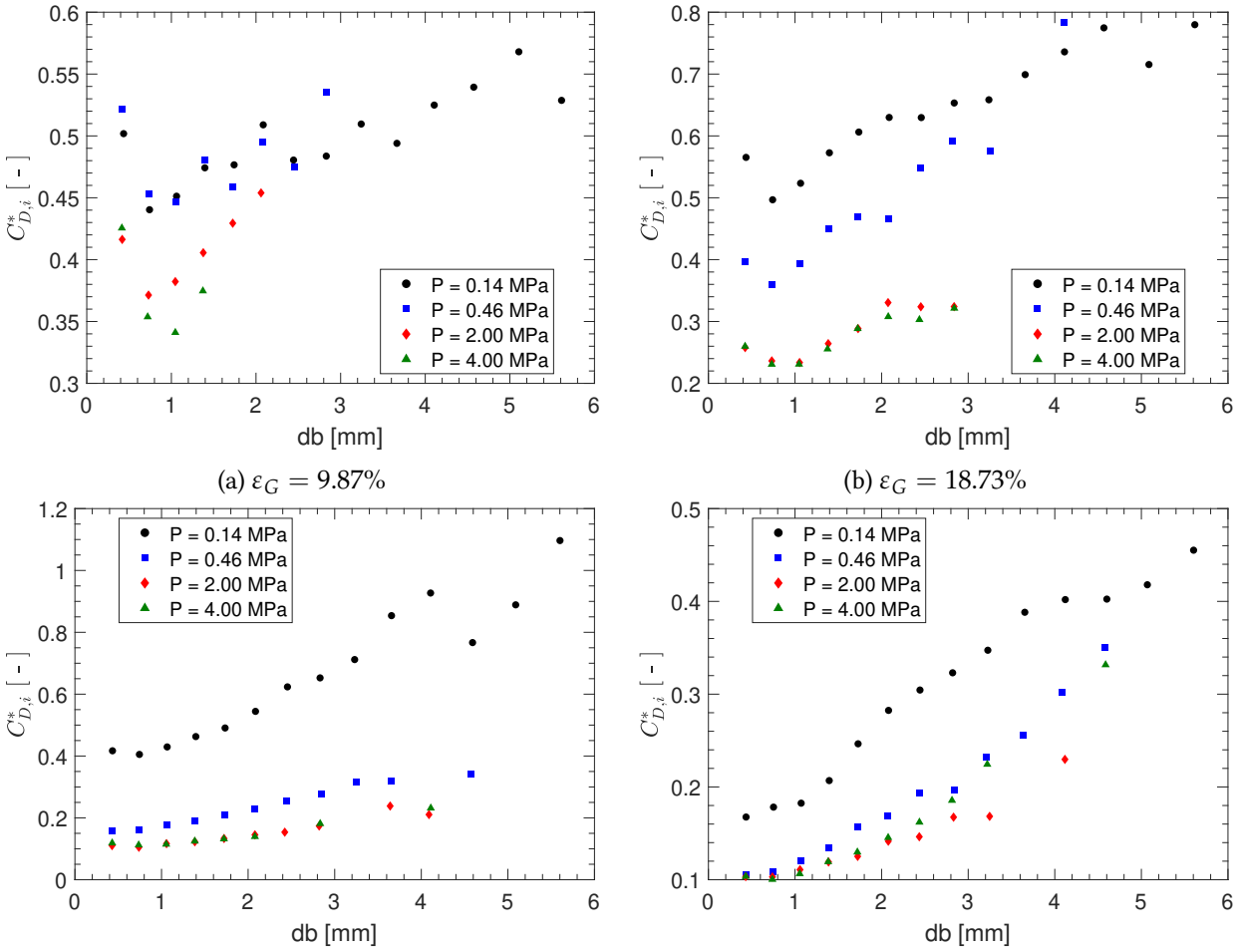

(a) $\varepsilon_G = 9.87\%$ (b) $\varepsilon_G = 18.73\%$

(c) $\varepsilon_G = 26.4\%$ (d) $\varepsilon_G = 33.29\%$

Figure 4.4: Average drag coefficient of individual bubble classes at various gas hold-ups and pressures. Drag coefficient generally decreases with pressure at constant bubble size and gas holdup. The effect of pressure is enhanced at higher gas hold-ups.

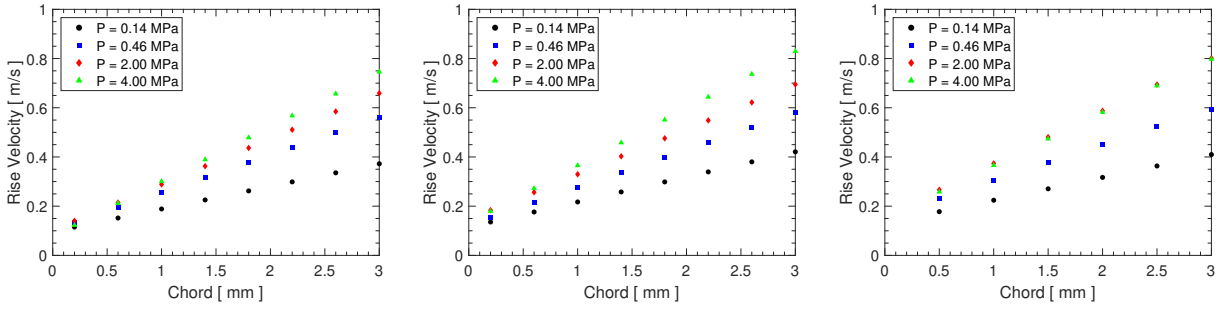

(a) $r/R = -0.60$ (b) $r/R = 0$ (c) $r/R = 0.60$

Figure 4.5: Plot of rise velocities against bubble chord length at various radial positions and pressures ($\varepsilon_G = 18.73\%$). Individual rise velocities increase with pressure at each radial position.

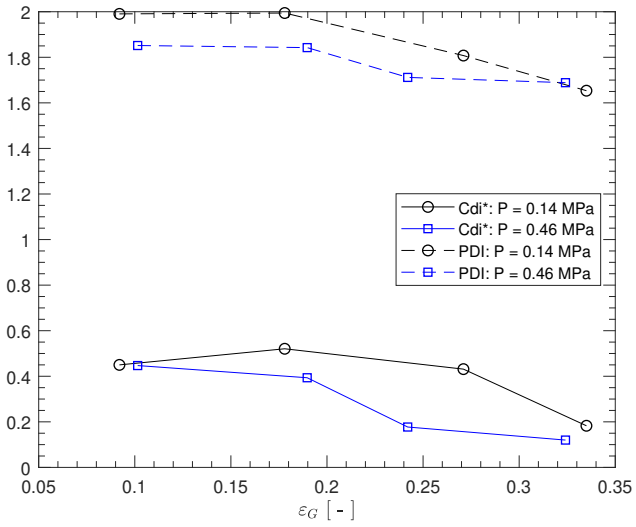

Figure 4.6: Plot of drag coefficient (1 mm bubble) and polydispersity index PDI against gas holdup. Similar trends can be seen for both drag coefficient and polydispersity index suggesting that drag variation with gas holdup could be due to swarm polydispersity.

pressure. To compute the swarm correction factor $C^*_{D,i}/C_{D\infty,i}$ from experimental data, an accurate model of isolated bubble's slip velocity $U_{b\infty,i}$ is needed, see equation (4.14).

$$\frac{C^*_{D,i}}{C_{D\infty,i}} = \left(\frac{U_{b\infty,i}}{U_{s,i}}\right)^2 \tag{4.14}$$

However, existing models for $U_{b\infty,i}$ are valid for systems in which the liquid phase is stagnant and show significant discrepancy amongst themselves, in the bubble size range (0.4 - 6 mm) of interest, due to differing levels of surface contamination and initial bubble detachment conditions.[2] To circumvent this, we fit a new single bubble drag model $C_{D\infty,i}$ as a function of *Re* and *Eo* (see equation 4.15). Note that equation (4.15) reduces to the Stokes model as the product of *Re* and *Eo* approaches zero. The choice of dimensionless numbers was inspired by the work of Tomiyama et al.[1] The departure from piecewise function in Tomiyama et al.[1] was necessary to obtain a better fit to our data.

$$C_{D\infty,i} = \frac{24}{Re}\left[1 + (Re.Eo)^{\beta_1}\right] \tag{4.15}$$

We also propose a new swarm correction model as a function of gas holdup raised to a coefficient that changes with pressure and *Eo* (equation 4.16). Equation (4.17) defines the dimensionless

pressure p', where $P_{ref} = 0.10$ MPa. Although the impact of pressure on drag coefficient is due to changes in bubble size distribution, the effect is quantified through pressure which is precisely known and is the initial cause of observed effect. The dependence of swarm correction factor on bubble diameter is evident in Fig. 4.5, where the amount of change in drag coefficient from one pressure to another at a given gas holdup depends on bubble diameter. The choice of *Eo* over *Re* was made to obtain better fit to our data.

$$\frac{C^*_{D,i}}{C_{D\infty,i}} = (1-\varepsilon_G)^{\beta_2\left[1-exp\left(-\beta_3\frac{p'}{Eo}\right)\right]} \tag{4.16}$$

$$p' = \frac{P}{P_{ref}} \tag{4.17}$$

Combining equation (4.15) and (4.16) results in equation (4.18). The drag model in equation (4.18) was fitted to our data to obtain β_1, β_2, and β_3. Figure 4.7 is a plot of model predicted average drag coefficients against their corresponding experimental values. A reasonably good fit was obtained as indicated by R^2 equal to 0.84, an average absolute relative error (AARE) equal to 20.42%, and a bias factor equal to 1.05. Model parameters and their standard errors are outlined in Table 4.2 and were fitted for $46 \leq Re \leq 2089$ and $0.02 \leq Eo \leq 4.54$.

$$C^*_{D,i} = \frac{24}{Re}\left[1+(Re.Eo)^{\beta_1}\right](1-\varepsilon_G)^{\beta_2\left[1-exp\left(-\beta_3\frac{p'}{Eo}\right)\right]} \tag{4.18}$$

Table 4.2: Parameters for the new drag model

Parameter	Mean Value	Standard Error
β_1	0.42	0.00
β_2	3.96	0.22
β_3	0.07	0.01

Earlier swarm correction models were extended from the work of Richardson and Zaki [30] on the settling of uniformly sized solid spheres, as shown in equations (4.19) and (4.20), where n is the

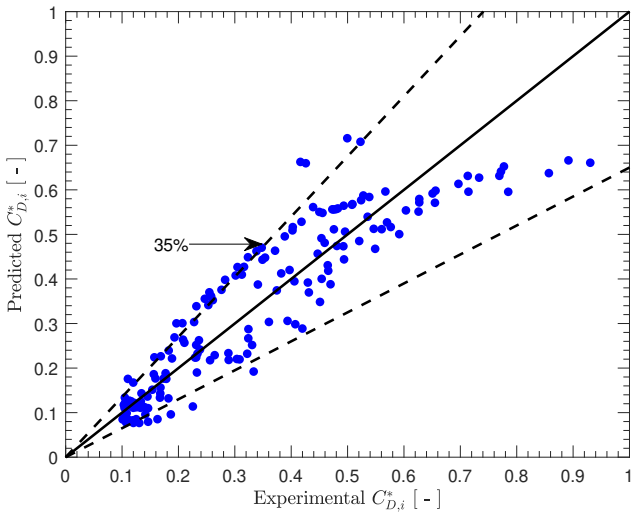

Figure 4.7: Parity plot comparing predicted drag coefficients to experimentally determined drag coefficients

Richardson-Zaki coefficient. The value of n varies from 4.65 to 2.39 depending on particle Reynolds number.

$$U_{s,i} = U_{b\infty,i}\left(1-\varepsilon_G\right)^n \tag{4.19}$$

$$\frac{C^*_{D,i}}{C_{D\infty,i}} = \left(1-\varepsilon_G\right)^{-2n} \tag{4.20}$$

Based on our experimental results at near atmospheric conditions, n ranges from -2.01 to -0.03 for Eo values ranging from 0.02 to 4.54, respectively. This suggests that the effect of swarm polydispersity is assistive to begin with, depends on bubble diameter and diminishes to a constant non-zero value since the maximum stable diameter decreases, eventually levelling off at elevated pressures.

4.5 CONCLUSION

Experiments were performed to determine the effect of pressure on the drag coefficient of individual bubbles in a contaminated polydisperse swarm. Various gas holdups ranging from 10 to 34% were investigated at constant liquid superficial velocity of 0.03 m/s to control gas holdup and wall-induced turbulence, respectively. The optical probe used to measure bubble sizes and

rise velocities was positioned 1.02 m above a perforated plate distributor to minimize the effect of turbulence generated at the inlet.

Our analysis show that, for bubbles in the diameter range of 0.4 to 6 mm, the drag coefficient decreases with increasing pressure due to a shift in bubble size distribution towards the smaller sizes. These smaller bubbles induce, relatively speaking, marginal disturbances in the liquid and could dampen or inhibit other sources of turbulence, resulting in reduced drag. A new empirical drag model was proposed to improve CFD simulation of bubble columns at elevated pressures.

ACKNOWLEDGEMENTS

The authors are grateful to Stéphane Gluck and Nicolas Zuanon of A2 Photonic Sensors for their technical support. The authors would also like to thank the Natural Sciences and Engineering Research Council of Canada, Ontario's Ministry of Training, Colleges and Universities, and Syncrude Canada Ltd. for financial assistance.

NOMENCLATURE

L_s	probe sensing length, μm
$t_{R,i}$	signal rise time, ms
$u_{br,i}$	individual bubble rise velocity, m/s
$c_{br,i}$	individual bubble chord length, m
$t_{b,i}$	bubble residence time, ms
n_{bri}	number of bubbles in a given class at a given radial position
$\overline{u}_{br,i}$	local mean bubble rise velocity within a given class at a given radial position, m/s
$\overline{c}_{br,i}$	local mean bubble chord length within a given class at a given radial position, m

$\overline{d}_{br,i}$	local mean bubble diameter within a given class at a given radial position, m
E	bubble aspect ratio
Eo	Eötvös number
$U_{b,i}$	global mean bubble rise velocity within a given class, m/s
$d_{b,i}$	global mean bubble diameter within a given class, m
r	radial position, m
dr	differential radius, m
$C^*_{D,i}$	mean drag coefficient within a given class
$U_{s,i}$	mean slip velocity within a given class, m/s
U_L	gas superficial velocity, m/s
ε_g	overall gas holdup, $m^3_{bubbles}/m^3_{reactor}$
ρ_L	liquid density, kgm^{-3}
ρ_G	gas density, kgm^{-3}
g	gravitational acceleration, m/s^2
dP	dynamic pressure loss, Pa
dz	vertical distance between pressure ports, m
PDI	polydispersity index
$C_{D\infty,i}$	isolated bubble drag coefficient
$U_{b\infty,i}$	isolated bubble slip velocity, m/s
Re	bubble Reynolds number
p’	dimensionless pressure
P_{ref}	reference pressure, 1 bar
n	Richardson-Zaki coefficient
β_1	model parameter
β_2	model parameter
β_3	model parameter

[1] Akio Tomiyama, Isao Kataoka, Iztok Zun, and Tadashi Sakaguchi. Drag coefficients of single bubbles under normal and micro gravity conditions. *JSME Int. Journal, Ser. B Fluids Therm. Eng.*, 41(2):472–479, 1998. ISSN 13408054. doi: 10.1299/jsmeb.41.472.

[2] A. Tomiyama, G. P. Celata, S. Hosokawa, and S. Yoshida. Terminal velocity of single bubbles in surface tension force dominant regime. *Int. J. Multiph. Flow*, 28(9):1497–1519, 2002. ISSN 03019322. doi: 10.1016/S0301-9322(02)00032-0.

[3] R. Clift, J. Grace, and M. Weber. *Bubbles, Drops, and Particles*. Academic Press, New York, 1978.

[4] Amol A. Kulkarni and Jyeshtharaj B. Joshi. Bubble formation and bubble rise velocity in gas-liquid systems: A review. *Ind. Eng. Chem. Res.*, 44(16):5873–5931, aug 2005. ISSN 08885885. doi: 10.1021/ie049131p.

[5] G. Q. Yang, Bing Du, and L. S. Fan. Bubble formation and dynamics in gas-liquid-solid fluidization-A review. *Chem. Eng. Sci.*, 62(1-2):2–27, 2007. ISSN 00092509. doi: 10.1016/j.ces.2006.08.021.

[6] M. Simonnet, C. Gentric, E. Olmos, and N. Midoux. Experimental determination of the drag coefficient in a swarm of bubbles. *Chem. Eng. Sci.*, 62(3):858–866, 2007. ISSN 00092509. doi: 10.1016/j.ces.2006.10.012.

[7] M. J. Lockett and R. D. Kirkpatrick. Ideal Bubbly Flow and Actual Flow in Bubble Columns. *Trans. Inst. Chem. Eng.*, 53(4 (OCTOBER, 1975)):267–273, 1975.

[8] I. Roghair, Y. M. Lau, N. G. Deen, H. M. Slagter, M. W. Baltussen, M. Van Sint Annaland, and J. A.M. Kuipers. On the drag force of bubbles in bubble swarms at intermediate and high Reynolds numbers. *Chem. Eng. Sci.*, 66(14):3204–3211, 2011. ISSN 00092509. doi: 10.1016/j.ces.2011.02.030.

[9] A. Buffo, M. Vanni, P. Renze, and D. L. Marchisio. Empirical drag closure for polydisperse gas–liquid systems in bubbly flow regime: Bubble swarm and micro-scale turbulence. *Chem. Eng. Res. Des.*, 113:284–303, 2016. ISSN 02638762. doi: 10.1016/j.cherd.2016.08.004.

[10] Y. M. Lau, I. Roghair, N. G. Deen, M. van Sint Annaland, and J. A.M. Kuipers. Numerical investigation of the drag closure for bubbles in bubble swarms. *Chem. Eng. Sci.*, 66(14): 3309–3316, 2011. ISSN 00092509. doi: 10.1016/j.ces.2011.01.053.

[11] Peter M. Wilkinson, Arie P. Spek, and Laurent L. van Dierendonck. Design parameters estimation for scale-up of high-pressure bubble columns. *AIChE J.*, 38(4):544–554, 1992. ISSN 15475905. doi: 10.1002/aic.690380408.

[12] Veniamin G Levich. *Physiochemical Hydrodynamics*. Prentice Hall, Engelwood Cliffs, NJ, 1962.

[13] Akimi Serizawa and Isao Kataoka. Turbulence suppression in bubbly two-phase flow. *Nucl. Eng. Des.*, 122(1-3):1–16, 1990. ISSN 00295493. doi: 10.1016/0029-5493(90)90193-2.

[14] Shigeo Hosokawa and Akio Tomiyama. Bubble-induced pseudo turbulence in laminar pipe flows. *Int. J. Heat Fluid Flow*, 40:97–105, 2013. ISSN 0142727X. doi: 10.1016/j.ijheatfluidflow.2013.01.004.

[15] C. Garnier, M. Lance, and J. L. Marié. Measurement of local flow characteristics in buoyancy-driven bubbly flow at high void fraction. *Exp. Therm. Fluid Sci.*, 26(6-7):811–815, 2002. ISSN 08941777. doi: 10.1016/S0894-1777(02)00198-X.

[16] Akiko Fujiwara, Daijyu Minato, and Koichi Hishida. Effect of bubble diameter on modification of turbulence in an upward pipe flow. *Int. J. Heat Fluid Flow*, 25(3):481–488, 2004. ISSN 0142727X. doi: 10.1016/j.ijheatfluidflow.2004.02.018.

[17] Frédéric Risso. Agitation, mixing, and transfers induced by bubbles. *Annual Review of Fluid Mechanics*, 50(1):25–48, 2018. doi: 10.1146/annurev-fluid-122316-045003.

[18] C. D. Lane, V. Parisien, A. Macchi, and A. A. Donaldson. Investigation of bubble swarm drag at elevated pressure in a contaminated system. *Chem. Eng. Sci.*, 152:381–391, 2016. ISSN 00092509. doi: 10.1016/j.ces.2016.06.017.

[19] Guangyao Yang, Huahai Zhang, Jiajia Luo, and Tiefeng Wang. Drag force of bubble swarms and numerical simulations of a bubble column with a CFD-PBM coupled model. *Chem. Eng. Sci.*, 192:714–724, 2018. ISSN 00092509. doi: 10.1016/j.ces.2018.07.012.

[20] Peng Yan, Haibo Jin, Guangxiang He, Xiaoyan Guo, Lei Ma, Suohe Yang, and Rongyue Zhang. CFD simulation of hydrodynamics in a high-pressure bubble column using three optimized drag models of bubble swarm. *Chem. Eng. Sci.*, 199:137–155, 2019. ISSN 00092509. doi: 10.1016/j.ces.2019.01.019.

[21] Valois Parisien, Alixia Farrell, Dominic Pjontek, Craig A. McKnight, Jason Wiens, and Arturo Macchi. Bubble swarm characteristics in a bubble column under high gas holdup conditions. *Chem. Eng. Sci.*, 157:88–98, jan 2017. ISSN 00092509. doi: 10.1016/j.ces.2016.04.051.

[22] E. Barrau, N. Rivière, Ch Poupot, and A. Cartellier. Single and double optical probes in air-water two-phase flows: Real time signal processing and sensor performance. *Int. J. Multiph. Flow*, 25(2):229–256, mar 1999. ISSN 03019322. doi: 10.1016/S0301-9322(98)00042-1.

[23] Alain Cartellier. Optical probes for multiphase flow characterization: Some recent improvements. *Chem. Eng. Technol.*, 24(5):535–538, may 2001. ISSN 09307516. doi: 10.1002/1521-4125(200105)24:5<535::AID-CEAT535>3.0.CO;2-X.

[24] J. Enrique Juliá, Wouter K. Harteveld, Robert F. Mudde, and Harrie E.A. Van Den Akker. On the accuracy of the void fraction measurements using optical probes in bubbly flows. *Rev. Sci. Instrum.*, 76(3):035103, mar 2005. ISSN 00346748. doi: 10.1063/1.1862192.

[25] R. M. Wellek, A. K. Agrawal, and A. H.P. Skelland. Shape of liquid drops moving in liquid media. *AIChE J.*, 12(5):854–862, 1966. ISSN 15475905. doi: 10.1002/aic.690120506.

[26] Swapnil V. Ghatage, Mayur J. Sathe, Elham Doroodchi, Jyeshtharaj B. Joshi, and Geoffrey M. Evans. Effect of turbulence on particle and bubble slip velocity. *Chem. Eng. Sci.*, 100:120–136, 2013. ISSN 00092509. doi: 10.1016/j.ces.2013.03.031.

[27] E. Doroodchi, G. M. Evans, M. P. Schwarz, G. L. Lane, N. Shah, and A. Nguyen. Influence of turbulence intensity on particle drag coefficients. *Chem. Eng. J.*, 135(1-2):129–134, 2008. ISSN 13858947. doi: 10.1016/j.cej.2007.03.026.

[28] Dale D. McClure, John M. Kavanagh, David F. Fletcher, and Geoffrey W. Barton. Experimental investigation into the drag volume fraction correction term for gas-liquid bubbly flows. *Chem. Eng. Sci.*, 170:91–97, 2017. ISSN 00092509. doi: 10.1016/j.ces.2016.12.066.

[29] Swapna S. Rabha and Vivek V. Buwa. Experimental investigations of rise behavior of monodispersed/polydispersed bubbly flows in quiescent liquids. *Ind. Eng. Chem. Res.*, 49(21):10615–10626, nov 2010. ISSN 08885885. doi: 10.1021/ie1006454.

[30] J. F. Richardson and W. N. Zaki. The sedimentation of a suspension of uniform spheres under conditions of viscous flow. *Chem. Eng. Sci.*, 3(2):65–73, 1954. ISSN 00092509. doi: 10.1016/0009-2509(54)85015-9.

5

FLUID DYNAMICS MODELING OF A COMMERCIAL EBULLATED BED HYDROPROCESSOR

ABSTRACT

A new multiphase fluid dynamics model for a commercial ebullated bed hydroprocessor was developed. The impact of the gas–liquid distribution system is now explicitly included through new submodels for bubble size distribution and drag coefficients. The size distribution submodel is coupled with the existing gas–liquid separation submodel to better predict recycled gas and liquid flow rates. Either the mass of the catalyst inventory or recycle pump curve can be specified as inputs to converge the model; the former is not always well known during operation in which case the latter can be used after making a few assumptions. A sensitivity analysis was performed to study the impact of fresh treat gas velocity, catalyst mass, phase properties, and reactor internals on recycled gas and liquid flow rates, bubble size distribution, and bed liquid holdup. A 0.2 mm shift in bubble size distribution toward larger sizes was found to significantly increase bed liquid holdup, suggesting that distributor modification/redesign could help improve the capacity of the hydroprocessor.[1]

1 This chapter has been published in Industrial & Engineering Chemistry Research: doi.org/10.1021/acs.iecr.0c03454

5.1 INTRODUCTION

Non-conventional crude oil, such as oil sand bitumen and distillation residues, is viscous and contain impurities (e.g., sulfur, nitrogen, and heavy metals), making direct transportation and/or conventional refining impossible.[1] Ebullated bed reactors, among other technologies,[2] are often employed industrially to preprocess these heavy feedstocks to acceptable standards. The LC-Fining unit in Figure 5.1 is one such reactor designed to process vacuum tower residues at elevated pressures ($\sim$ 11.7 MPa) and temperatures ($\sim$ 440 °C).[3] Fresh residues and hydrogen treat gas are separately heated, premixed in static mixers, and fed into the plenum chamber of the unit, where they combine with internally recycled fluids and flow through the bubble cap risers on the grid. In the bed, liquid hydrocarbons are thermally cracked and hydrogenated in the presence of solid catalysts. A fraction of the liquid is recycled back to the plenum via the recycle line to keep the bed ebullated. The rest of the fluids leave the unit as an effluent.

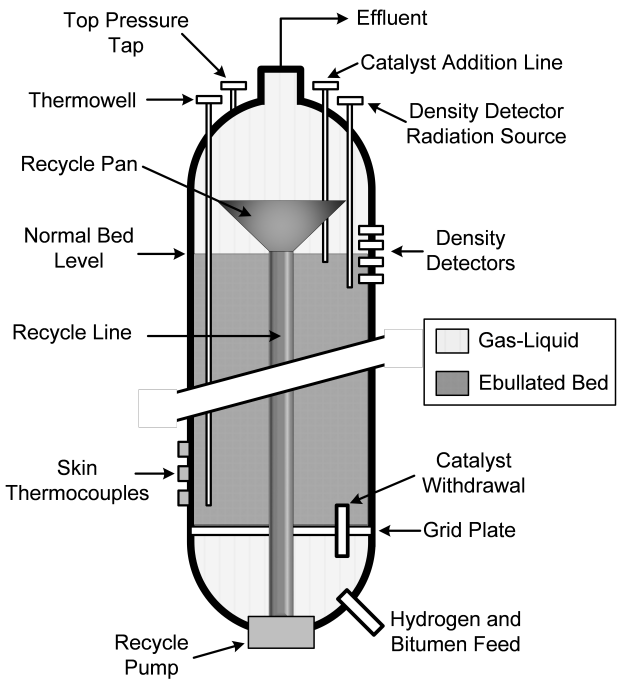

Figure 5.1: Simplified schematic of the LC-Fining unit (reprinted with permission from Pjontek et al.[4] Copyright 2015 Elsevier Ltd.)

The performance of the unit is affected by its operating conditions and internal geometry. Elevated pressures enhance bubble breakage through a combination of Kelvin–Helmholtz instability and internal circulation within bubbles, creating smaller bubbles with lower rise velocities.[5–8] Naturally occurring surface-active compounds adsorb onto the bubble–liquid interface and get swept to the rear of the bubble where they hinder bubble rise by inducing surface tension gradients.[9] The gas–liquid distribution system (plenum and grid) and the liquid recycle pan also affect the performance of the unit. A uniform spatial distribution of fluids into the bed is essential for uniform hydrogenation and to prevent the formation of a mesophase and coke, which can deposit on the grid and further hinder the distribution. Since bubbles do not readily coalesce in the bed,[10] the original bubble size distribution generated at the grid likely impacts gas–liquid separation at the recycle pan and gas entrained in the liquid recycle increases bed gas holdup at the expense of liquid holdup and product yield.

Previous studies on ebullated bed hydroprocessors focused on the scaling of bed fluid dynamics,[4,11–13] simulation of gas–liquid separation at the recycle pan,[14,15] modeling of overall reactor fluid dynamics,[16–19] and the impact of gas–liquid distribution system on bubble dynamics and properties.[20–22] Building on the works of Safoniuk et al.[11] and Macchi et al.,[12,13] Pjontek et al.[4] proposed a scaling approach for bed fluid dynamics. The proposed scaling required matching of five dimensionless groups (U_g/U_l, ρ_g/ρ_l, ρ_l/ρ_s, Ar_{L-S} and Re_{L-S}) and bubble coalescence behavior.

Lane et al.[14] developed a computational fluid dynamics model of the first generation recycle pan (two stage recycle cups) to perform a parametric analysis on the fluid dynamics in the separation region of the LC-Fining unit. Previous studies on freeboard gas holdup has suggested the potential presence of an effervescent foam in this region.[3] By assuming non-coalescing flow, they implemented a bubble–bubble packing limiter to investigate the impact of foam generation. Significant reductions in gas–liquid separation efficiency were reported for simulations in which

the disengaged gas-phase fraction reached the packing limiter. A sensitivity analysis of gas–liquid separation to gas and liquid velocities, freeboard gas holdup, liquid recycle fraction, and mean bubble diameter revealed that the liquid residence time through the pan can be used to correlate changes in the gas–liquid separation efficiency resulting from these parameters.

Lane et al.[15] later simulated the performance of the second generation recycle pan (flow through pan) by leveraging previously developed model.[14] An improved separation performance relative to the two stage recycle cups was reported for the flow through pan. The improvement was primarily due to better separation of larger bubbles (1–2 mm in diameter). No marked improvement in separation of smaller bubbles was reported. While both pan designs exhibited liquid short-circuiting, the reduction in the amount of liquid with lower residence time resulted in better separation of larger bubbles by the flow through pan.

Lane et al.[16] then incorporated their previously developed separation models[14,15] into an overall fluid dynamics model of the LC-Fining unit. As the bubble size information was not available at the time, an initial guess of the mean size was made to predict gas–liquid separation efficiency and subsequent iterations were necessary to determine the bubble size that provided the best fit to commercial operating data for the freeboard gas holdup. The gas–liquid separation efficiency was then used to determine recycled gas and liquid flow rates, which were in turn required to determine bed and freeboard holdups.

Eccles[17] developed a reactor model, assuming a flow through stirred tank, to investigate the relationship between frequency factor and catalyst ageing for three different modes of operation: (i) ebullated bed reactor with catalyst addition and withdrawal, (ii) ebullated bed reactor with fixed bed inventory, and (iii) stirred-basket reactor. The model was also used to develop other correlations, which accounted for the effect of catalyst replacement rate, catalyst pore volume, and ratio of thermal to catalytic zones. The fluid dynamics model implicitly accounted for internal

recycles as it was based on commercial gas holdup data, making its extension to other operating conditions and reactor geometries difficult.

Schweitzer and Kressmann [18] developed a dynamic reactor model accounting for fluid dynamics and catalytic and thermal kinetics. The fluid dynamics model comprised a catalytic zone, bubble column, and the recycle line. Liquid flow in the catalytic zone and bubble column was modeled as a dispersed-plug flow, while gas flow in the same zones was modeled as a plug flow. In the recycle line, there was only liquid and it was assumed to be in plug flow. Two lumped reaction schemes were used to describe simultaneous hydrocracking and thermal cracking. Phase equilibria were also considered. The fluid dynamics model was validated with a bench-scale reactor using a radioactive tracer test for residence time distributions in various industrial conditions.

Manek and Haydary [19] developed a simplified block model of a cascade of three ebullated bed hydroprocessors in Aspen Plus to investigate the impact of liquid recycle (without gas) on ebullated bed characteristics. Measurements from an industrial scale hydrocracking unit were used as inputs to the Aspen Plus model. Calculated distillation curves and reactor inlet temperatures were compared to experimental values to validate the model. Model analyses included (i) the influence of the feed rate on recycle ratio, (ii) the relationship between the recycle flow rate, recycle pump head, and catalyst inventory, and (iii) the relationship between the recycle ratio and temperature gradient across the cascade.

Mach et al. [20] utilized a perforated plate and a geometrically scaled bubble cap plate to investigate the impact of plenum conditions and a gas–liquid distributor on the resulting bubble properties in atmospheric conditions. Plenum conditions tested were found to have a marginal impact on the resulting phase holdups. For both plates, measured mean bubble sizes correlated well with power dissipation and gas–liquid velocity ratio to the power of -0.4 and 0.60, respectively, which is in agreement with theory on turbulent breakup of dense dispersions. Comparison of the propor-

tionality constants revealed that the bubble cap plate produced bubbles at least two times larger than the perforated plate due to possible recoalescence inside the risers and the space between the bubble cap and the riser. It is worth noting that the developed mean bubble size model relies on prior knowledge of a two-phase pressure drop through the distributor, which can be challenging to accurately predict. The model is also limited to turbulent flows, which may not always be the case such as for highly viscous hydrocarbon feed.

Mach et al.[21] proposed and experimentally validated a scaling approach for a gas-liquid distributor based on the industrial bubble cap geometry. Geometrical scaling was achieved by matching the distributor fractional open area and ratios of critical dimensions. Dynamic similarity was realized by matching three dimensionless groups (ρ_g/ρ_l, Re_l, and Fr_g) and bubble coalescence behavior. Measured bubble sizes were found to follow log-normal distributions. Distribution parameters were then extracted and correlated to the proposed dimensionless groups to enable the prediction of bubble size distribution in industrial conditions. The bubble size distribution produced at the distributor is an important input to the overall fluid dynamics model of the LC-Fining unit.

Mach et al.[22] investigated the effect of pressure on the drag coefficient of individual bubbles in a contaminated polydisperse swarm. The drag coefficient was found to decrease with increasing pressure at constant gas holdup. This effect was attributed to changes in the bubble size distribution. As pressure increased, the bubble size distribution shifted to smaller sizes. Relatively speaking, these smaller bubbles not only induce marginal liquid perturbations, but they can also dampen turbulence originating from other sources, resulting in reduced drag. A new drag model was proposed. In the study of Mach et al.[21] new parameters of the drag model were estimated for the industrial bubble cap geometry. It was found that bubbles generated by the industrial bubble cap geometry are more hindered than their similarly sized counterparts produced by the perforated plate since the latter are surrounded by smaller bubbles that induce lower liquid-phase turbulence.

The objective of this study is to incorporate a new gas–liquid distributor model into the overall multiphase fluid dynamics model of the LC-Fining unit. Bubble size distribution and drag models proposed in the study of Mach et al.[21] will be used to predict phase holdups in the unit. Further, the size distribution model will be coupled with the gas–liquid separation model proposed by Lane et al.[15] to better predict recycled gas and liquid flow rates and, consequently, phase holdups. Two new numerical frameworks using mass of the catalyst inventory or the recycle pump curve as inputs to determine the bed height (criterion for convergence) are described in the next section. The catalyst inventory may not always be well known during operation in which case the pump curve can be used after making a few assumptions.

5.2 NUMERICAL METHODOLOGY

Figure 5.2 shows a compartmental model of the LC-Fining unit. Key compartments that will be detailed in this section include the grid, ebullated bed, freeboard, gas–liquid separator, and recycle line.

5.2.1 *Governing Equations*

5.2.1.1 *Grid Distributor*

Mach et al.[21] proposed a scaling approach for a gas–liquid distributor and experimentally validated it on a geometrically scaled version of the industrial bubble cap grid. The scaling was based on ensuring both geometric and dynamic similitude. Geometric similarity was achieved by matching the fractional open area and ratios of critical dimensions. Three dimensionless groups (ρ_g/ρ_l, Re_l and Fr_g) were identified through the Buckingham pi theorem and subsequent reduction. The gas–liquid density ratio (ρ_g/ρ_l) accounts for pressure-induced bubble breakage. The liquid Reynolds number (Re_l) is a measure of continuous phase turbulence and thus accounts for shear-induced and/or turbulent bubble breakage. Abdelsalam et al.[23] showed that the gas Froude number, which measures the relative importance of gas inertia to gravity, can also influence bubble sizes

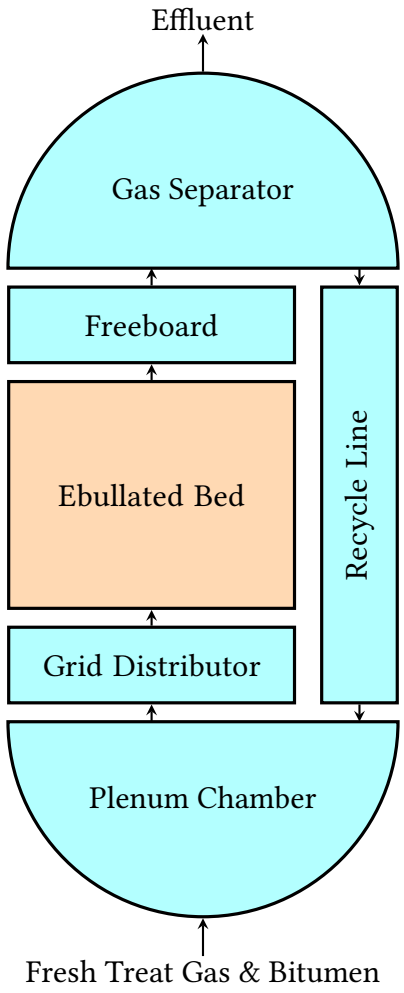

Figure 5.2: Compartmental model of the LC-Fining^{TM} unit

and internal flow regime.

Bubble properties were measured using a custom 1C-3C monofibre optical probe with a sensing length of 23.2 μm. The probe was positioned 0.60 m above the distributor and at 5 radial positions (r/R = 0, 0.20, 0.40, 0.60, 0.80) to determine column-wide bubble properties. Axial pressure profiles followed a linear trend, suggesting steady bubble rise and negligible changes in bubble properties with height. Camarasa et al.[24] also reported negligible changes in bubble size and shape with increasing height for a liquid contaminated with a surface active agent, conditions which are relevant to this work.

The experimental operating conditions were matched to the LC-Fining unit's hydrodynamics conditions as much as possible through dimensional analysis. Histograms of measured bubble chord lengths at the tested operating conditions suggested a log-normal distribution, which was later confirmed by an excellent fit to log-normal distribution model. The log-normal chord length distributions were observed for a liquid contaminated with surface active compound and for gas–liquid density ratios ranging from 0.00137 to 0.04958, liquid Reynolds numbers ranging from 1583 to 13,495, and gas Froude numbers ranging from 1.67 to 4.94. The probability density function for a log-normal distribution is shown in eq 5.1. The distribution parameters, μ and s, were extracted, rendered non-dimensional, and correlated with the three dimensionless groups (eqs 5.2 – 5.6).

$$P(c_{bi}) = \frac{1}{s\, c_{bi}\, \sqrt{2\pi}} \exp\left[-\frac{(\ln(c_{bi}) - \mu)^2}{2s^2}\right] \tag{5.1}$$

$$\mu = \mu^* + \ln(d_{or}) \tag{5.2}$$

$$\mu^* = -0.5305 - 0.1469 \ln\left(\frac{\rho_g}{\rho_l}\right) - 0.4229 \ln\left(\mathrm{Re}_l\right) + 0.3450 \ln\left(\mathrm{Fr}_g\right) \tag{5.3}$$

$$s = 0.7594 - 0.04206 \ln\left(\frac{\rho_g}{\rho_l}\right) - 0.0201 \ln\left(\mathrm{Re}_l\right) + 0.0596 \ln\left(\mathrm{Fr}_g\right) \tag{5.4}$$

$$\mathrm{Re}_l = \frac{\rho_l\, U_{lor}\, d_{or}}{\mu_l} \tag{5.5}$$

$$\mathrm{Fr}_g = \frac{U_{gor}}{\sqrt{g\, d_{or}}} \tag{5.6}$$

In this work, the lower and upper limits of the distribution containing 95% of the chord lengths were first determined. Multiple bubble classes with uniform widths of 0.01 mm were then constructed

from the estimated limits. The equivalent diameter $d_{b,i}$ of an individual bubble class was based on the equivalent diameter of an oblate ellipsoid given by eq 5.7, where d_{horz} and d_{vert} are the lengths of the horizontal and vertical axes, respectively. The equivalent diameter can be re-expressed in terms of the length of the vertical axis using the aspect ratio ($E = \frac{d_{vert}}{d_{horz}}$) as shown in eq 5.8. The individual bubble chord length ($c_{b,i}$) can be related to the length of the vertical axis through eq 5.9.[25] Substituting eq 5.9 into eq 5.8 gives eq 5.10. Equation 5.11 is the aspect ratio model of Wellek et al.[26] and eq 5.12 defines the Eötvös number. The resulting equivalent bubble diameters and their corresponding probability densities were coupled with the drag and gas separation models to predict freeboard gas holdups and recycle flow rates, respectively.

$$d_{b,i} = \left(d_{horz}^2 * d_{vert}\right)^{1/3} \tag{5.7}$$

$$d_{b,i} = d_{vert} E^{-2/3} \tag{5.8}$$

$$d_{vert} = 3/2 c_{b,i} \tag{5.9}$$

$$d_{bi} = 3/2\, c_{bi}\, E^{-2/3} \tag{5.10}$$

$$E = \frac{1}{1 + 0.163 Eo^{0.757}} \tag{5.11}$$

$$\mathrm{Eo} = \frac{\left(\rho_l - \rho_g\right) g d_{bi}^2}{\sigma} \tag{5.12}$$

5.2.1.2 *Ebullated Bed*

Prediction of bed liquid holdup is important because it is required to determine the effective reaction volume, total reaction rate, pitch, and Conradson carbon residue (CCR) conversions. High CCR conversion is critical to minimize the amount of hydrocarbon feed converted to the undesirable coke. Pjontek et al.[4] utilized the Richardson–Zaki relationship to develop a correlation for particle holdup in conditions relevant to the LC-Fining unit (eqs 5.13 – 5.17). The correlation explicitly accounts for fluid velocities, particle–liquid Archimedes number, particle terminal velocity, particle–liquid Reynolds number, and wall effects.

$$\varepsilon_s = 1 - \left(\frac{U_{lbed}}{k\, u_{p\infty}}\right)^{1/n} \left[1 + 0.22 \left(\frac{U_{gbed}}{U_{lbed}}\right)^{0.92}\right] \tag{5.13}$$

$$k = 1 - 1.33 \left(\frac{d_v}{d_c}\right) \tag{5.14}$$

$$\frac{4.8 - n}{n - 2.4} = 0.043 \mathrm{Ar}_{L-S}^{0.57} \left[1 - 1.24 \left(\frac{d_v}{d_c}\right)^{0.27}\right] \tag{5.15}$$

$$\mathrm{Re}_{p\infty} = \mathrm{Ar}_{L-S}^{1/3} \left[\frac{18}{\mathrm{Ar}_{L-S}^{2/3}} + \frac{2.335 - 1.744\phi}{\mathrm{Ar}_{L-S}^{1/6}}\right]^{-1} \tag{5.16}$$

$$u_{p\infty} = \frac{\mu_l}{\rho_l d_v} \mathrm{Re}_{p\infty} \tag{5.17}$$

Pjontek et al.[4] also established a simple linear relationship (eq 5.18) between freeboard and bed gas holdup under conditions in which bubble coalescence was sufficiently inhibited (e.g., surfactant-contaminated liquid, high-pressure operation, and large dense solids). In atmospheric conditions, the model underpredicted some freeboard gas holdups due to particle-induced bubble breakage. In this work, the bed gas holdup is back-calculated from the freeboard gas holdup.

$$\varepsilon_{gbed} = \frac{\varepsilon_g}{1.3} \tag{5.18}$$

The bed liquid holdup is estimated using eq 5.19, which satisfies continuity and requires gas and particle holdups estimated from previous correlations (eqs 5.13 and 5.18).

$$\varepsilon_{lbed} = 1 - \varepsilon_{gbed} - \varepsilon_s \tag{5.19}$$

Due to the location of the densitometers on the LC-Fining unit, the recycle pump speed is manipulated to position the bed level at the location of the densitometers. As such, the bed height will be utilized as a convergence criterion. Equation 5.20 shows the calculation of the bed height for a known mass of the catalyst inventory.

$$h_{bed} = \frac{4m_{cat}}{\pi d_c^2 \varepsilon_s \rho_p} \tag{5.20}$$

When the mass of the catalyst inventory is not well known, the recycle pump curve can be utilized to estimate the bed height after making a few assumptions. As shown in eq 5.21, the pump head (ΔP_{pump}) comprises the grid pressure drop (ΔP_{grid}), ebullated bed pressure drop (ΔP_{bed}), freeboard pressure drop ($\Delta P_{freeboard}$), recycle pan pressure drop (ΔP_{pan}), and recycle line pressure drop ($\Delta P_{recycle}$). Each of these components is defined in eqs 5.22 – 5.26. Please note that wall frictional losses were deemed negligible for the bed and recycle line due to their respective sizes.

$$\Delta P_{pump} = \Delta P_{grid} + \Delta P_{bed} + \Delta P_{freeboard} + \Delta P_{pan} + \Delta P_{recycle} \tag{5.21}$$

$$\Delta P_{grid} = f_1 \left(\varepsilon_{g,grid}\, \rho_g + \varepsilon_{l,grid}\, \rho_l\right) \left(U_g + U_l\right)^2 \tag{5.22}$$

$$\Delta P_{bed} = \left(\varepsilon_{gbed}\rho_g + \varepsilon_{lbed}\rho_l + \varepsilon_s\rho_s\right) g h_{bed} \tag{5.23}$$

$$\Delta P_{freeboard} = \left(\varepsilon_g \rho_g + \varepsilon_l \rho_l\right) g \left(h_{recycle} - h_{bed}\right) \tag{5.24}$$

$$\Delta P_{pan} = f_2 \left(\varepsilon_g \, \rho_g + \varepsilon_l \, \rho_l\right) \left(U_g + U_l\right)^2 \tag{5.25}$$

$$-\Delta P_{recycle} = \frac{q_{g,recycle} \, \rho_g + q_{l,recycle} \, \rho_l}{q_{recycle}} g h_{recycle} \tag{5.26}$$

In addition to matching a prescribed bed height, bed liquid velocity must be greater than the minimum fluidization velocity. Building on the works of Zhang et al.,[27] Lee et al.[28] proposed a correlation for gas-liquid-solid minimum fluidization velocity (eq. 5.27 – 5.33).

$$\mathrm{Re}_{mf} = \sqrt{C_1^2 + C_2 \, \mathrm{Ar}_p} - C_1 \tag{5.27}$$

$$\mathrm{Ar}_p = \frac{\rho_l \left[\rho_p - \left(\rho_g \alpha_{mf} + \rho_l \left(1 - \alpha_{mf}\right)\right)\right] g d_v^3}{\mu_l^2} \tag{5.28}$$

$$\alpha_{mf} = \frac{0.16 U_{gbed}}{\varepsilon_{mf} \left(U_{gbed} + U_{lmf}\right)} \tag{5.29}$$

$$C_1 = \frac{150 \left(1 - \varepsilon_{mf}\right)}{3.5 \phi} \tag{5.30}$$

$$C_2 = \frac{\varepsilon_{mf}^3 \left(1 - \varepsilon_{mf}\right)^3}{1.75} \tag{5.31}$$

$$\varepsilon_{mf} = \varepsilon_{mfo} \left[1 - 0.34 \left(1 - \frac{U_{lmf}}{U_{lmfo}}\right) + 0.22 \left(1 - \frac{U_{lmf}}{U_{lmfo}}\right)^2\right] \tag{5.32}$$

$$U_{lmf} = \frac{\mu_l}{\rho_l d_v} \mathrm{Re}_{mf} \tag{5.33}$$

As shown in eq. 5.32, the liquid-solid minimum fluidization velocity (U_{lmfo}) and void fraction (ε_{mfo}) are required inputs for the calculation of gas-liquid-solid values. Equations 5.34 – 5.39 show the calculation of these required inputs.

$$\mathrm{Re}_{mfo} = \sqrt{C_{1o}^2 + C_{2o}\,\mathrm{Ar}_{L-S}} - C_{1o} \tag{5.34}$$

$$\mathrm{Ar}_{L-S} = \frac{\rho_l\left(\rho_p - \rho_l\right) g d_v^3}{\mu_l^2} \tag{5.35}$$

$$C_{1o} = \frac{150\left(1-\varepsilon_{mfo}\right)}{3.5\phi} \tag{5.36}$$

$$C_{2o} = \frac{\varepsilon_{mfo}^3}{1.75} \tag{5.37}$$

$$\varepsilon_{mfo} \approx \frac{0.415}{\sqrt[3]{\phi}} \tag{5.38}$$

$$U_{lmfo} = \frac{\mu_l}{\rho_l d_v}\mathrm{Re}_{mfo} \tag{5.39}$$

5.2.1.3 *Freeboard*

To determine freeboard gas holdup, multiple bubble classes were constructed and their probability densities estimated using the bubble size distribution model presented in section 5.2.1.1 The drag coefficient of an individual bubble class was estimated using the model developed in the study of Mach et al.[21] and presented in eq. 5.42. The rise velocity of an individual bubble class can be determined using eq. 5.41, which is derived from a force balance on an individual bubble in a swarm. The rise velocity can also be estimated from fluids velocities and individual bubble class holdup as shown in eq. 5.40. To compute the class holdup, an initial guess of its rise velocity is

made and subsequent iterations performed to ensure the rise velocity predicted by eq. 5.40 and 5.41 are practically the same (absolute tolerance = 10^{-5}). To compute overall freeboard gas holdup, the class holdups are weighted using the predicted probability densities as shown in eq. 5.43.

$$u_{s,i} = \frac{U_{gbed}}{\varepsilon_{g,i}} - \frac{U_{lbed}}{1-\varepsilon_{g,i}} \tag{5.40}$$

$$u_{si} = \sqrt{\frac{4}{3}\frac{g\,d_{bi}\,E^{2/3}}{C^*_{D,i}}\frac{\rho_l - \rho_g}{\rho_l}} \tag{5.41}$$

$$C^*_{D,i} = \frac{24}{Re_b}\left[1 + (Re_b.Eo)^{0.47}\right]\left[1-\varepsilon_{g,i}\right]^{2.46\left[1-exp\left(-\frac{0.13p'}{Eo}\right)\right]} \tag{5.42}$$

$$\varepsilon_g = \frac{\sum_i \varepsilon_{g,i} P(d_{bi})}{\sum_i P(d_{bi})} \tag{5.43}$$

One key assumption made here is that the bubble size distribution generated at the grid is preserved through the bed and freeboard regions. For similar operating conditions and when bubble coalescence was significantly inhibited, Pjontek et al.[10] found both local and global gas holdups measured in the freeboard to match those measured in a bubble column. This suggested that the bubble size distribution generated at the grid is likely preserved through the bed and freeboard regions. It is still likely for particles in the bed to promote bubble break-up and/or coalescence, especially when the particles are smaller than the bubbles, solids holdup is significantly high and bubble coalescence is not inhibited. However, this is likely not the case under industrial conditions since bubbles are generally smaller than particles, particles holdup is significantly low ($\sim$ 25%) and bubble coalescence is inhibited by naturally occuring surface active compounds.

5.2.1.4 *Gas-liquid Separator and Recycle Line*

The separation efficiency of an individual bubble class (η_i) is given by eq. 5.44, where k' is a liquid residence time in the pan and B_i depends on bubble size and pan design. The probability ($P_{recycle}$)

of entraining an individual bubble class in the liquid recycle is given by eq. 5.46, where R and P are the internal recycle ratio and probability of the bubble class in the bed, respectively. The overall separation efficiency (η) is given by eq. 5.47.

$$\eta_i = 0.29\, ln\left(k'\right) + B_i \tag{5.44}$$

$$k' = \frac{V_{sep}}{q_{l,recycle}} \tag{5.45}$$

$$P_{recycle}\left(d_{bi}\right) = \left(1 - \eta_i\right) R\, P\left(d_{bi}\right) \tag{5.46}$$

$$\eta = 1 - \frac{\sum_i P_{recycle}\left(d_{bi}\right)}{R \sum_i P\left(d_{bi}\right)} \tag{5.47}$$

Gas and liquid flow rates in the recycle line are calculated using eq. 5.48 and 5.49, respectively.

$$q_{g,recycle} = R\ \left(1 - \eta\right)\ q_{gbed} \tag{5.48}$$

$$q_{l,recycle} = R\, q_{lbed} \tag{5.49}$$

Gas and liquid flow rates through the bed are calculated from inlet and recycle flow rates using eq. 5.50 and 5.51, respectively. Consumption of hydrogen, which is in excess, and vaporization of lighter components also contribute to bed flow rates and resulting phase holdups. Phase equilibria and reaction kinetics, which are out of the scope of this work, are required to predict the net impact on flow rates and resulting fluid dynamics.

$$q_{gbed} = U_{gbed} A_c = q_{g,treat} + q_{g,recycle} \tag{5.50}$$

$$q_{lbed} = U_{lbed} A_c = q_{l,vr} + q_{l,recycle} \tag{5.51}$$

5.2.2 *Numerical Solution*

Two numerical algorithms using either catalyst mass or recycle pump curve to calculate bed height are proposed. Fig. 5.3 and 5.4, respectively, show the catalyst inventory and pump curve algorithms. The internal loops ensure bed liquid velocity is greater than minimum fluidization velocity, while the outer loops ensure the bed height is within 10^{-8} tolerance of desired bed height dictated by the position of densitometers. Both loops manipulate internal recycle ratio, which is akin to changing recycle pump speed in practice, to meet specified tolerances. The algorithm in Fig. 5.3 is implemented in this paper and utilized to explore the impact of fresh treat gas velocity, catalyst inventory, phase properties and reactor internals on recycled gas and liquid fractions, bubble size distribution and bed liquid holdup.

5.3 RESULTS AND DISCUSSION

5.3.1 *Effects of Fresh Treat Gas Flow Rate*

Figure 5.5 shows the effect of fresh treat gas velocity (based on inlet hydrogen flow rate and reactor cross-sectional area) on recycled gas and liquid fractions, bubble size distribution, and bed liquid holdup. Given that both gas and liquid velocities contribute to bed expansion, an increase in fresh treat gas velocity lowers the amount of gas and liquid recycle needed to maintain a specific bed height. Although the fraction of recycled gas decreases with fresh treat gas velocity, the gas flow through the distribution system increases. Coupled with lower liquid recycle flow rates, this shifts bubble size distribution toward larger values, but whether these larger bubbles decrease bed and freeboard gas holdup depends on individual gas velocities. At sufficiently low gas velocities, the

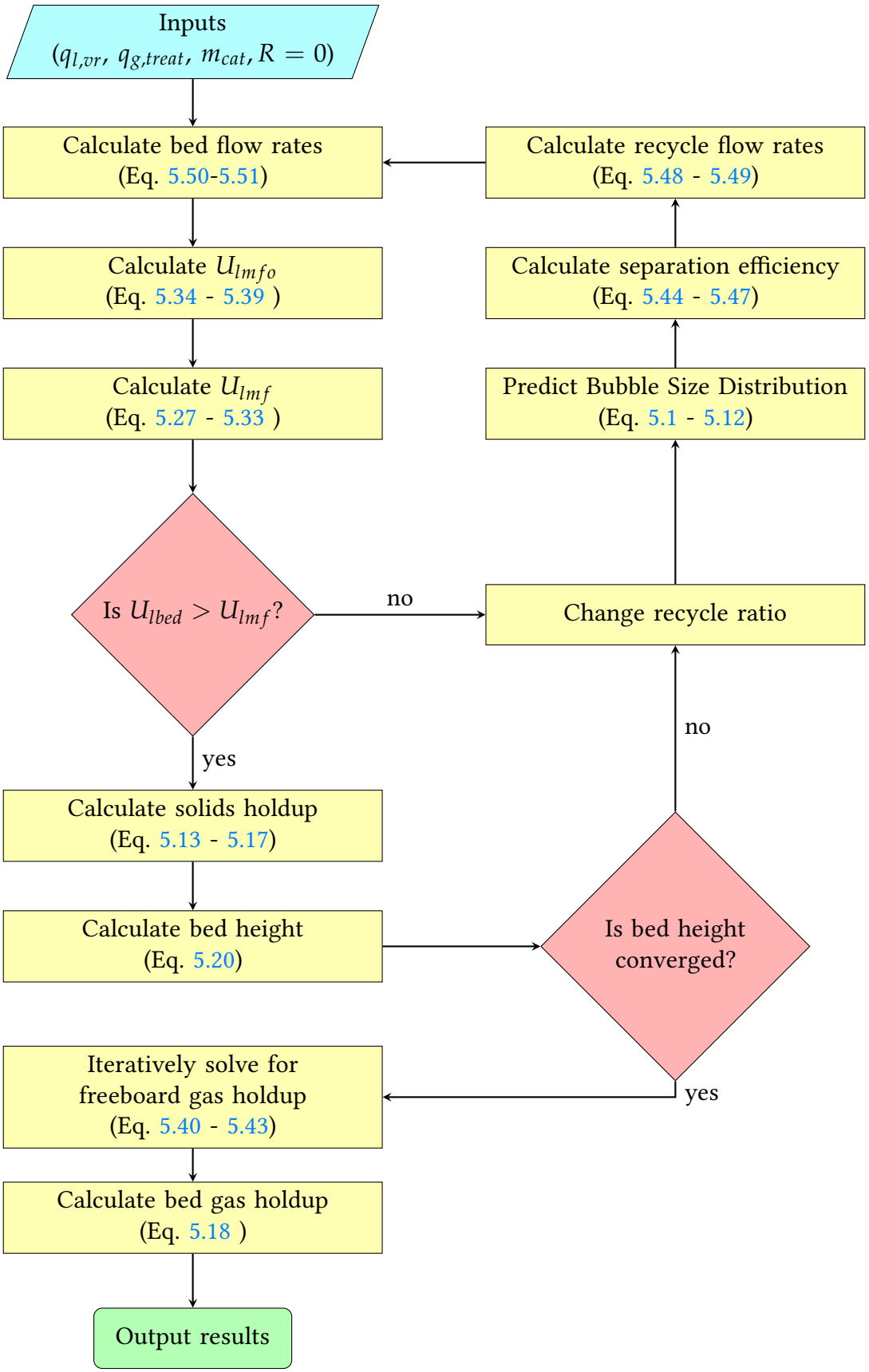

Figure 5.3: Flow chart for an algorithm utilizing catalyst inventory to converge bed height

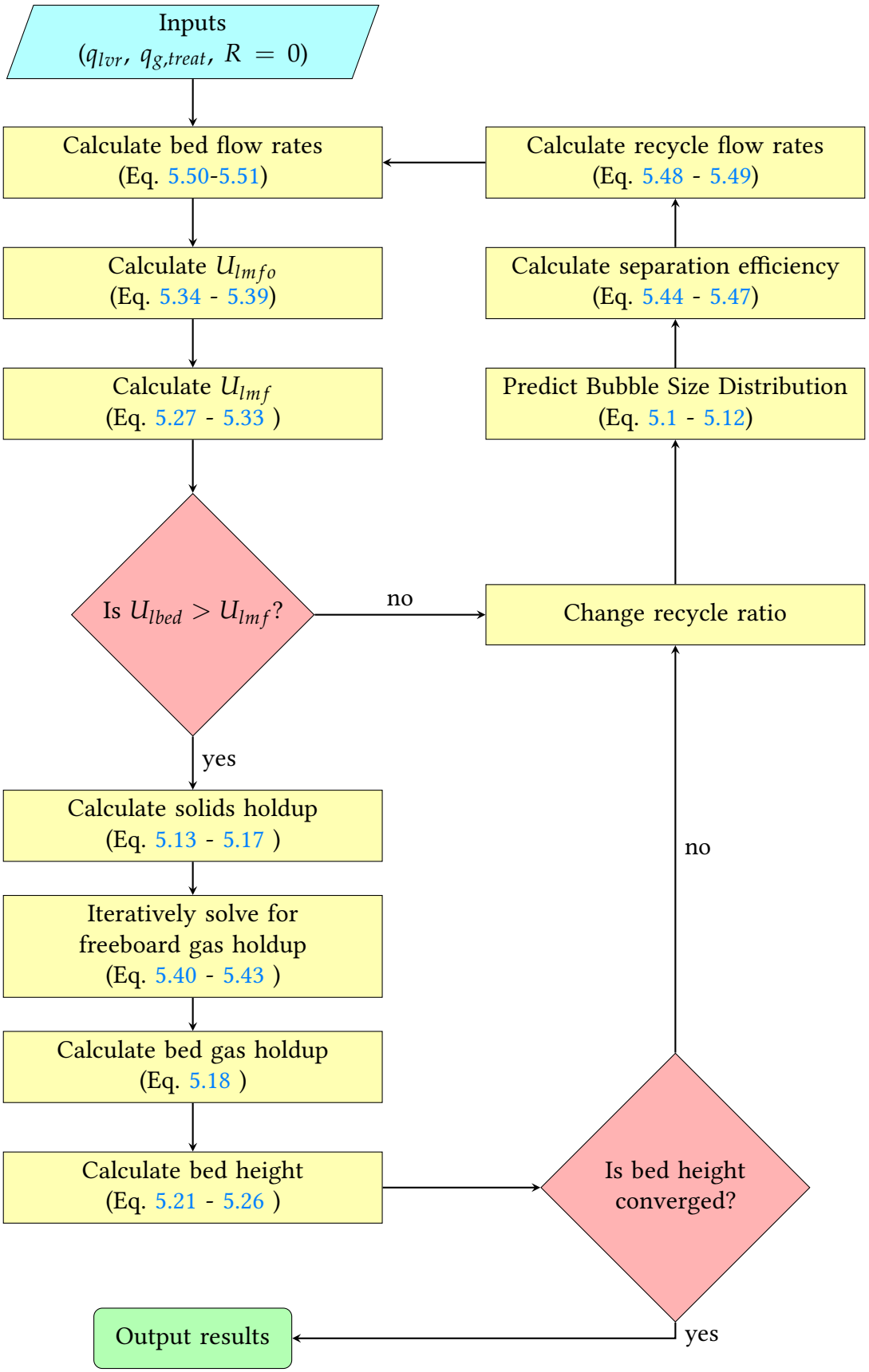

Figure 5.4: Flow chart for an algorithm utilizing pump calculations to converge bed height

increase in bubble sizes may not be enough to lower gas residence time and holdup. As gas velocity increases, the effect of bubble size becomes more significant, offsetting the increase in gas holdup caused by increased gas flow/volume. Given that both the bed height and catalyst inventory are constant, the bed liquid holdup decreases with fresh treat gas velocity to satisfy continuity.

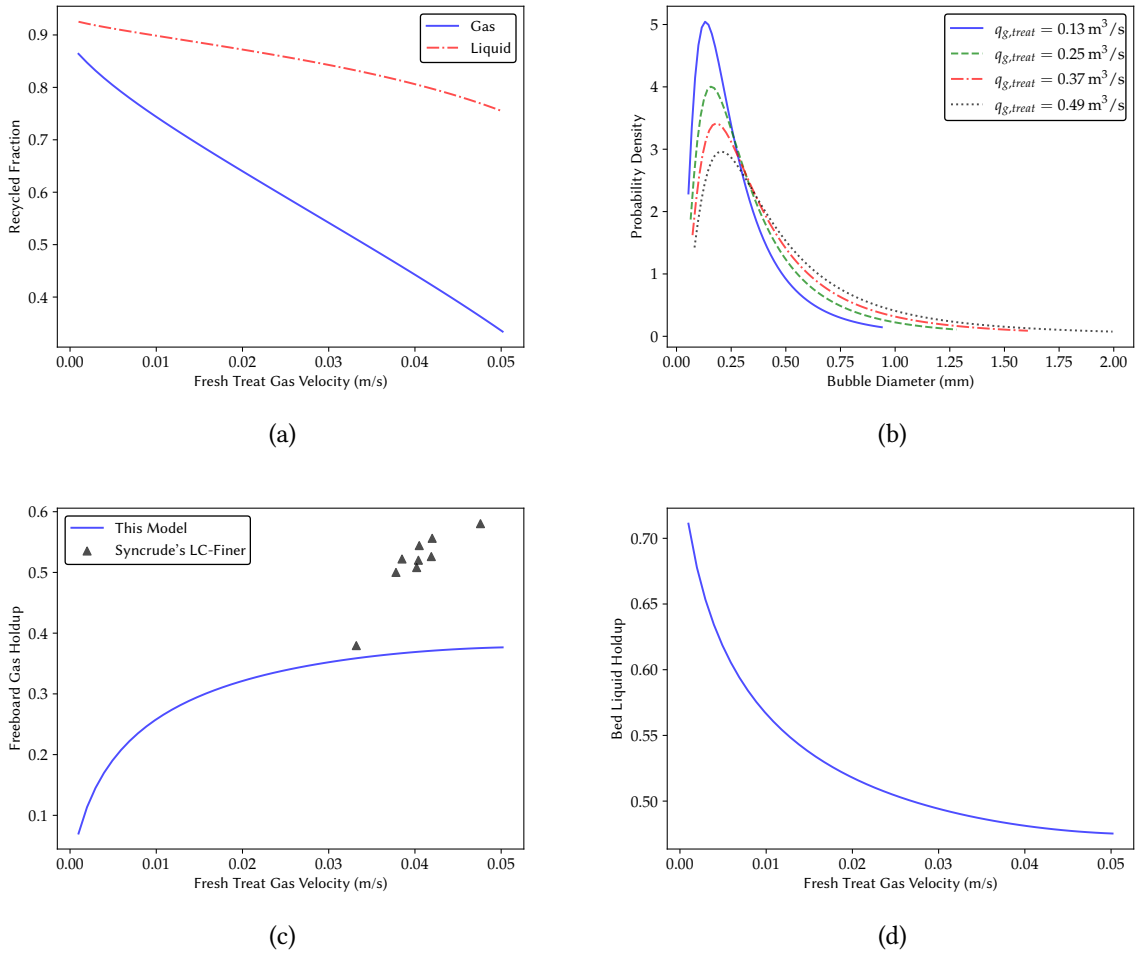

Figure 5.5: Effect of treat gas velocity on (a) recycled gas and liquid fractions, (b) bubble size distribution, (c) freeboard gas holdup, and (d) bed liquid holdup (fixed bed height and $m_{cat} = 65,000$ kg).

With the exception of the lowest commercial gas holdup data, the model under-predicts industrial freeboard gas holdup by at least 10 per cent points (Figure 5.5). Although the mass of the catalyst inventory and phase properties are not precisely known, the discrepancy is largely attributable to vaporization of lighter components. Commercial gas holdup data collected at Exxon and presented

in Eccles[17] clearly show the impact of vaporized lighter components on gas holdup, where gas holdups greater than 10% were recorded with no treat gas flowing. Some previous fluid dynamics models[16] showed negligible gas holdup discrepancy despite not modeling vaporization of lighter components. Such models were tuned with commercial operating data due to the lack of bubble size information, and as a result, they implicitly accounted for the effect of vaporization of lighter components and reaction kinetics. As this work explicitly models bubble size distribution, the commercial operating data is not used for tuning purposes, resulting in the decoupling of vaporization of lighter components and reaction kinetics and making the fluid dynamics model more extensible to other operating conditions.

It is likely that the amount of vaporized lighter components is dependent on fresh treat gas velocity as hydrogen partial pressure increases with fresh treat gas velocity and influences reaction rates, bed temperature, and consequently phase equilibria. However, the fluid dynamics behavior of vaporized lighter components is not clear; would the vapors appear as independent bubbles from nucleation events (e.g., on catalyst particles/solid impurities) or would they appear by increasing the volumes of existing bubbles in a ratio proportional to their surface area (i.e., smaller bubbles more likely to grow due to larger surface area)? Depending on how the vaporized components affect the bubble size distribution, the gas–liquid separation efficiency of the pan may or may not be affected.

5.3.2 *Effects of Catalyst Inventory*

The true mass of the bed inventory is not precisely known when the catalyst is continuously added and withdrawn from the unit. Due to the fixed measured region of the internal density detectors, the bed height must be maintained within a specific window for control purposes. Fluidization is controlled through liquid recycled via the recycle pump, whose speed must be adjusted when the

catalyst inventory changes.

Figure 5.6 shows the effect of catalyst mass on recycled gas and liquid fractions, bubble size distribution, and bed liquid holdup. With an increase in catalyst mass, the amount of recycled gas and liquid decreases, resulting in a relatively smaller increase in bubble sizes since lower gas and liquid flow rates have opposite effects. An increase in the solids inventory naturally increases solids holdup and lowers gas holdup. However, the change in gas holdup is not sufficient to satisfy continuity; hence, there is a decrease in liquid holdup. The resulting impact on CCR conversion is difficult to predict since lower liquid holdup and higher solids holdup have opposite effects; the former increases liquid residence time and decreases conversion, and the latter increases conversion by increasing the surface area available for reaction.

5.3.3 *Effects of Feed Properties*

Changes to bitumen feed composition, such as increasing the fraction of the vacuum residue, can alter its phase properties. Sensitivity analysis is performed on individual phase properties even though more than one property can change when feed composition changes. This analysis also serves to determine the effect of uncertainty arising from experimentally estimating phase properties.

Figure 5.7 shows the effect of pressure and gas density on recycled gas and liquid fractions, bubble size distribution, and bed liquid holdup. Elevated pressures induce bubble breakage and create smaller bubbles with lower slip velocities. These smaller bubbles are entrained in the liquid recycle since they cannot disengage fast enough. Due to poorer separation at the recycle pan, more gas is internally recycled, increasing bed gas holdup and lowering bed liquid holdup. It is worth pointing out that the relative change in liquid holdup is much smaller than the relative change in

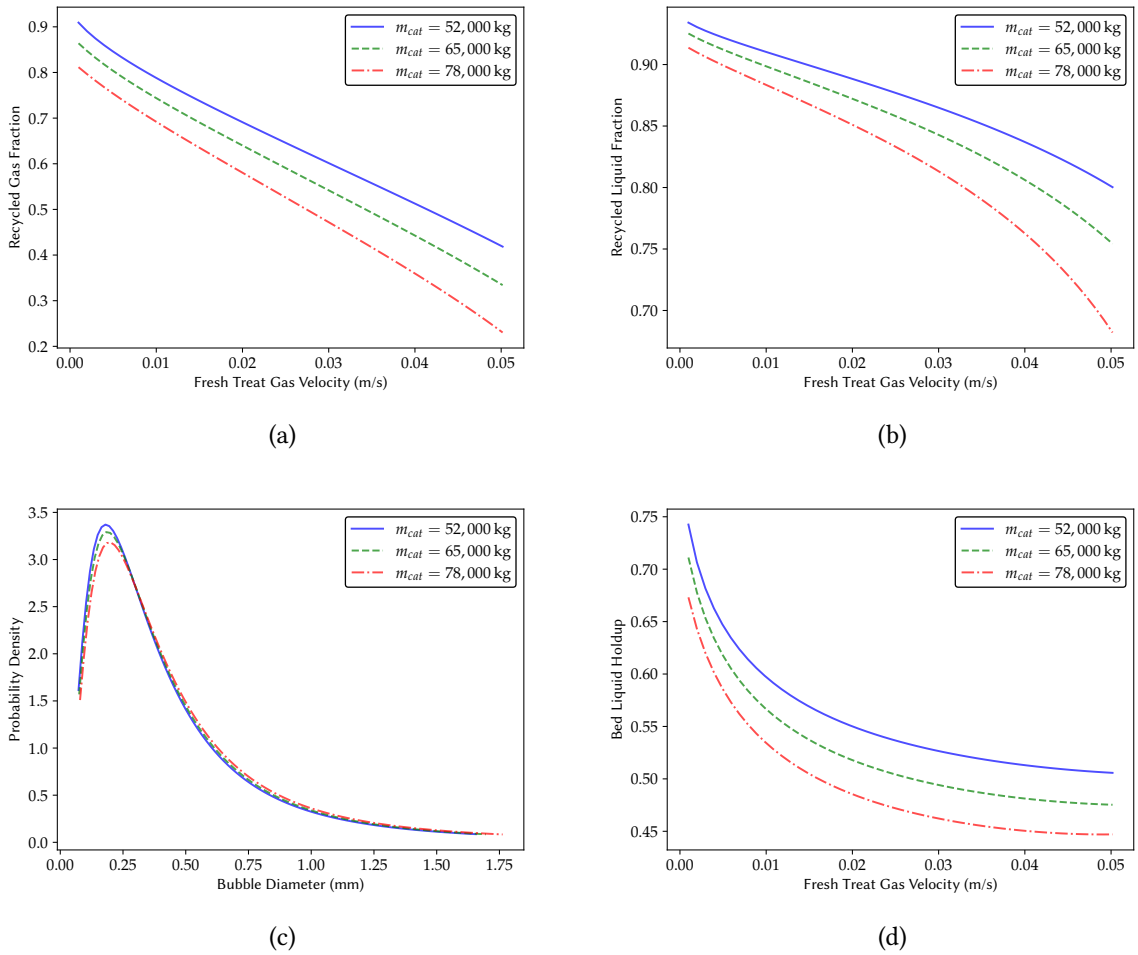

Figure 5.6: Effect of catalyst mass on (a) recycled gas fraction, (b) recycled liquid fraction, (c) bubble size distribution ($q_{g,treat} = 0.40\ m^3/s$) and (d) bed liquid holdup(fixed bed height).

pressure since the base value is already high (11.7 MPa). In the study of Mach et al.[22] bubble size distributions and individual bubble drag coefficients were found to change marginally above 2 MPa.

Figure 5.8 shows the effect of liquid density on recycled gas and liquid fractions, bubble size distribution, and bed liquid holdups. The effect of an increase in liquid density is twofold: (i) it increases continuous phase turbulence and (ii) it lowers the minimum fluidization velocity; the former results in smaller bubbles being generated at the grid and the latter results in less gas and liquid being recycled to keep the bed fluidized. Based on the impact of liquid density on bubble

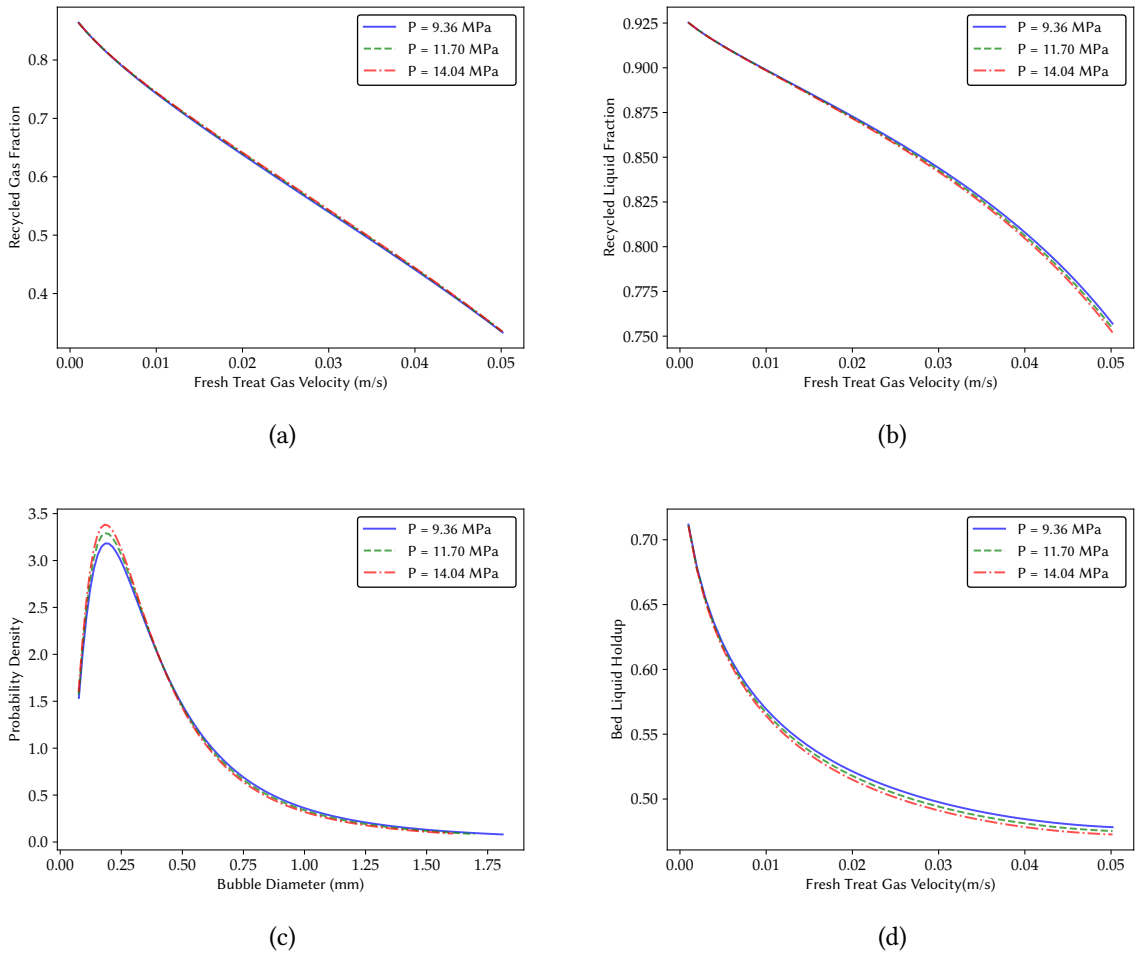

Figure 5.7: Effect of operating pressure/gas density on (a) recycled gas flowrate, (b) recycled liquid flowrate, (c) bubble size distribution ($q_{g,treat} = 0.40\ m^3/s$) and (d) bed liquid holdup (fixed bed height and $m_{cat} = 65,000$ kg).

size distribution (Figure 5.8c), the latter effect appears to dominate.

Figure 5.9 shows the effect of liquid viscosity on recycled gas and liquid fractions, bubble size distribution, and bed liquid holdup. An increase in liquid viscosity increases bubble sizes, lowers minimum fluidization velocity, and increases the drag coefficient. As mentioned, lower minimum fluidization velocity means lower recycle flow rates. Lower liquid recycle flow rates, coupled with the generation of larger bubbles at the grid, improves gas separation. The impact of drag coefficient appears to outweigh the combined impact of bubble sizes and minimum fluidization velocity since liquid holdup decreases with viscosity.

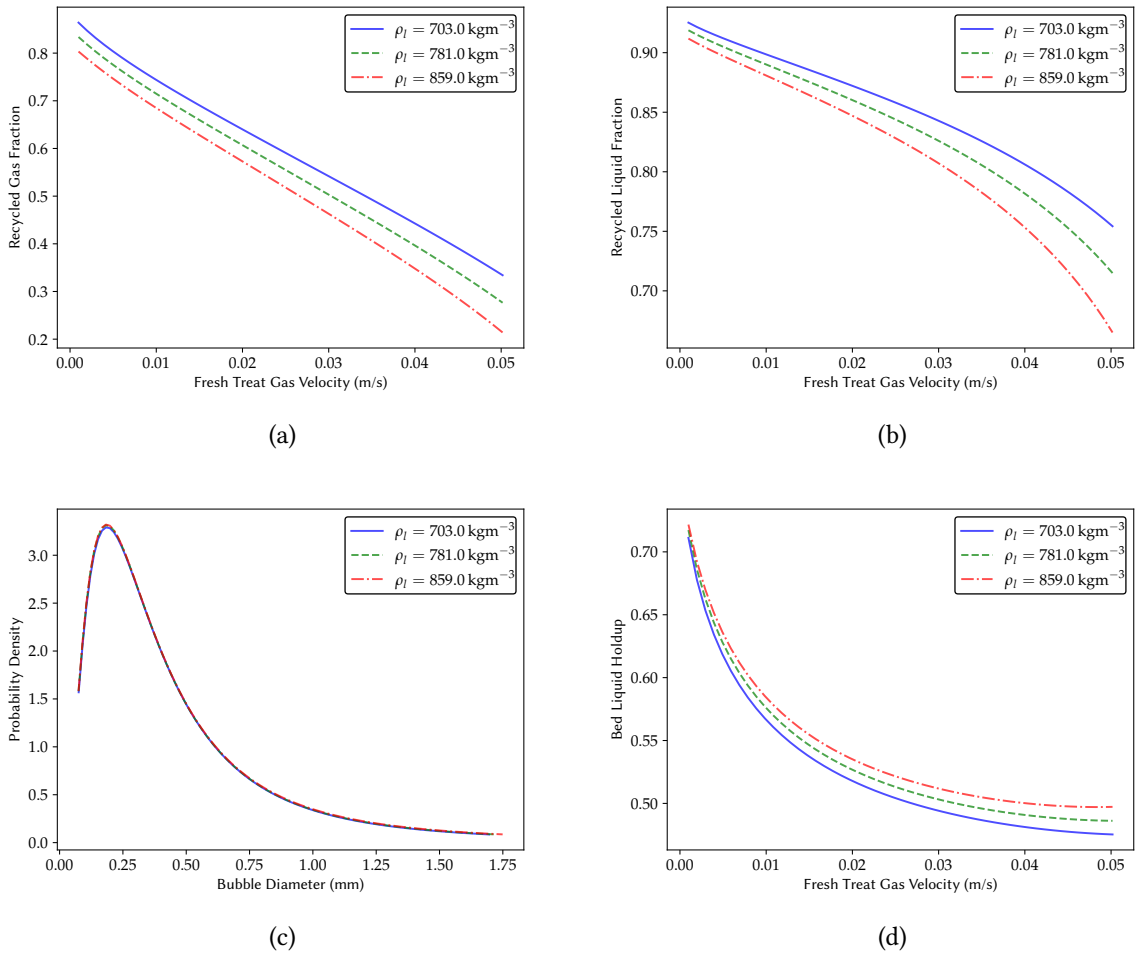

Figure 5.8: Effect of liquid density on (a) recycled gas flowrate, (b) recycled liquid flowrate, (c) bubble size distribution ($q_{g,treat} = 0.40\ m^3/s$) and (d) bed liquid holdup (fixed bed height and $m_{cat} = 65,000$ kg).

5.3.4 *Effects of Internals*

In this section, the impact of different recycle pan designs is first compared and then the effect of shifting bubble size distribution towards larger bubbles is investigated. The location parameter (LOC) is increased from 0 to 0.2 to simulate the effect of the shift. The means through which such a shift could be achieved are proposed, if desirable.

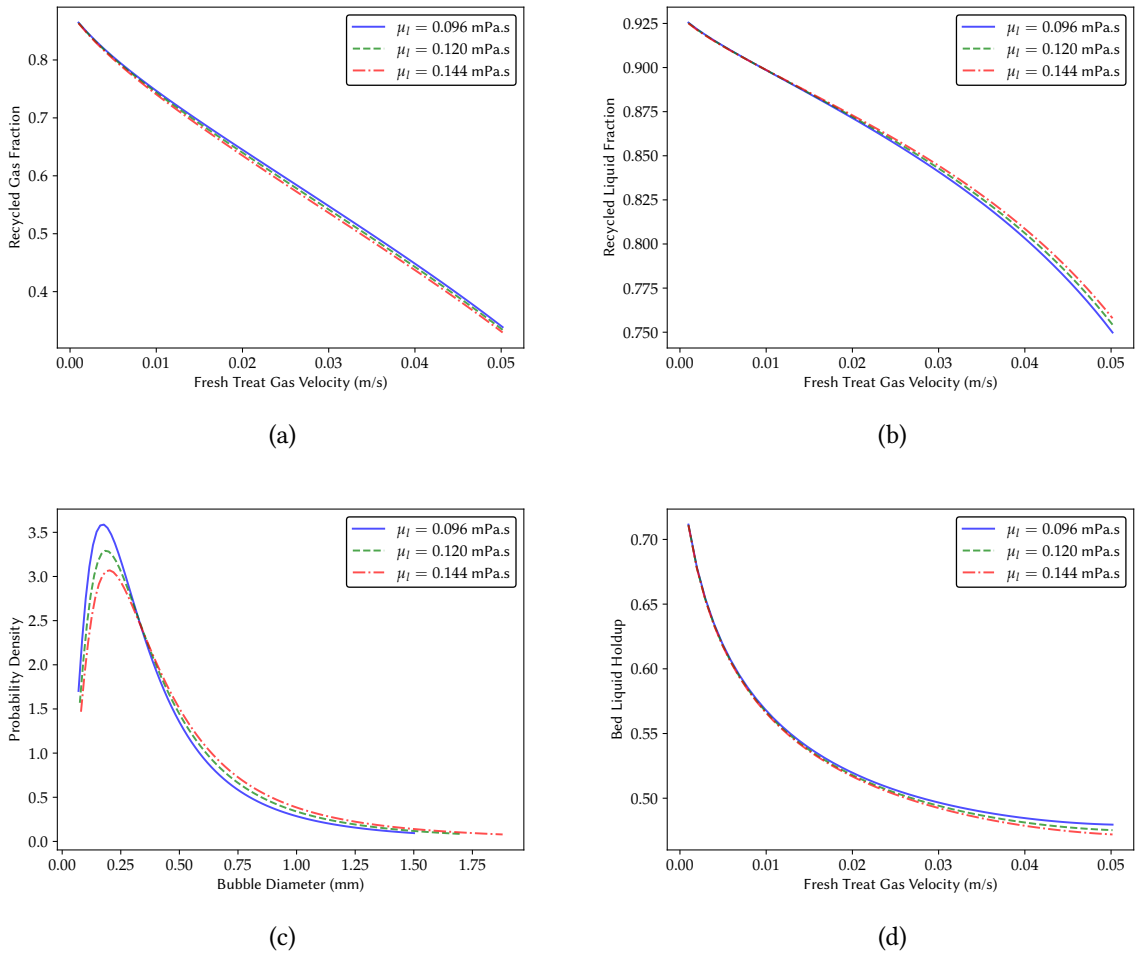

Figure 5.9: Effect of liquid viscosity on (a) recycled gas flowrate, (b) recycled liquid flowrate, (c) bubble size distribution ($q_{g,treat} = 0.40\ m^3/s$) and (d) bed liquid holdup (fixed bed height and $m_{cat} = 65,000$ kg).

Figure 5.10 compares the performance of flow through pan and two stage recycle cups. As expected, there is a marginal difference in the overall performance of the two pans. There is a clear need to reduce the amount of recycled gas to improve the performance of the industrial unit. In the case of the recycle pan, this could be achieved by increasing liquid residence time and/or promoting bubble coalescence to produce larger bubbles that disengage faster. Hamdani et al.[29] showed that twisted tape inserts, which induce swirling flow, could enhance bubble coalescence, albeit with air–water at atmospheric pressure. Enhancing bubble coalescence is certainly a greater challenge operating at high pressure with surface-active agents, where the extra energy input could potentially further reduce the bubble size — although similar solutions have been proposed for gas–liquid separation

by Chan and Colvert.[30]

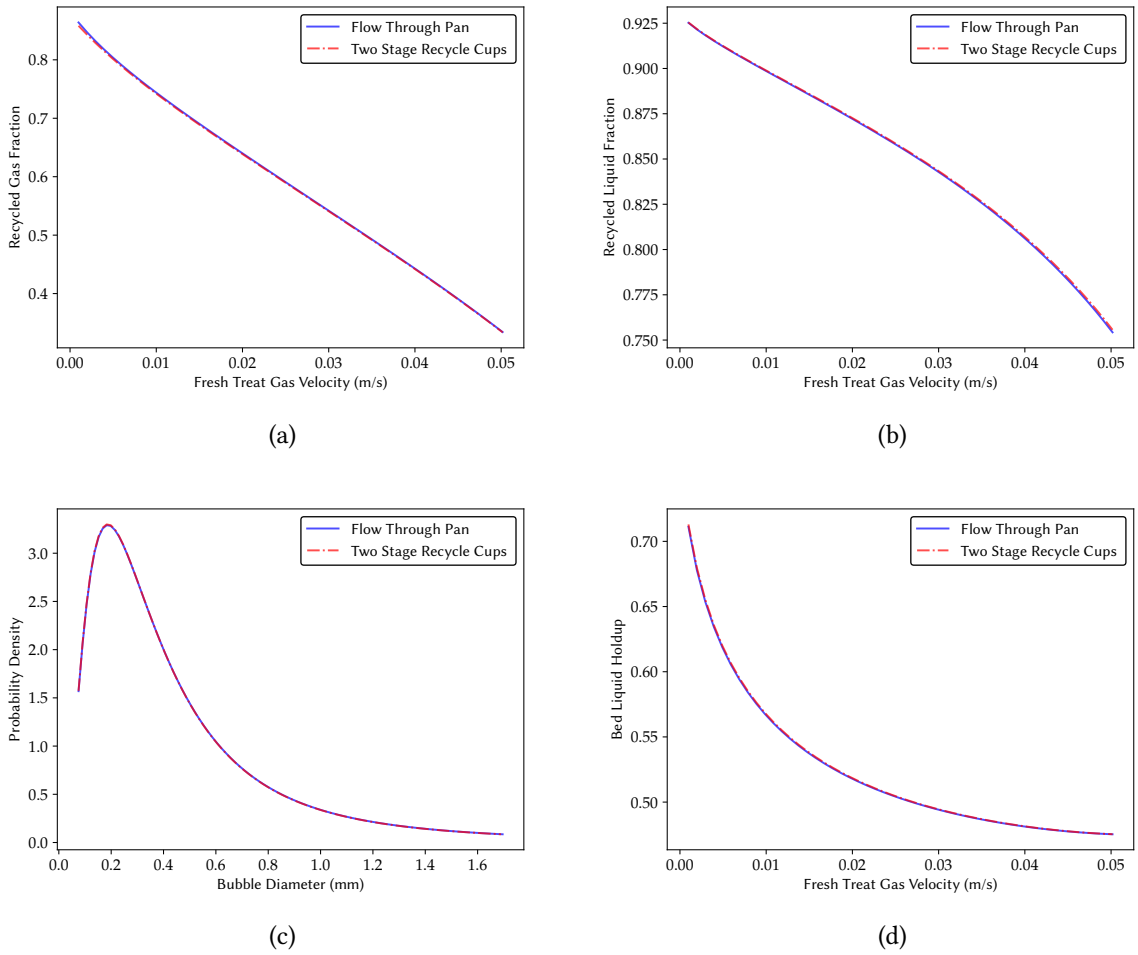

Figure 5.10: Effect of pan design on (a) recycled gas flowrate, (b) recycled liquid flowrate, (c) bubble size distribution ($q_{g,treat} = 0.40\ m^3/s$) and (d) bed liquid holdup.

Figure 5.11 shows the effect of the location parameter on recycled gas and liquid fractions, bubble size distribution, and bed liquid holdup. A location parameter of zero represents the unshifted bubble size distribution and the current distributor design. A value of 0.20, for example, signifies a positive shift in bubble size distribution by 0.20 mm. Modification of the grid operating conditions to achieve a shift of 0.1 or 0.2 mm in bubble size has significant potential to improve the bed liquid holdup and processing capacity. Based on the bubble size distribution model, the energy dissipation/liquid velocity through each orifice would need to be reduced in order to achieve the desired

bubble size distribution. There is certainly a limit to changes in grid operating conditions since a minimum distributor pressure drop ($\sim$ 30% of frictional pressure drop across the bed) is required to ensure disturbances upstream do not travel downstream and vice versa. To achieve these changes, the catalyst inventory would thus need to be precisely controlled, which is a difficult task to achieve.

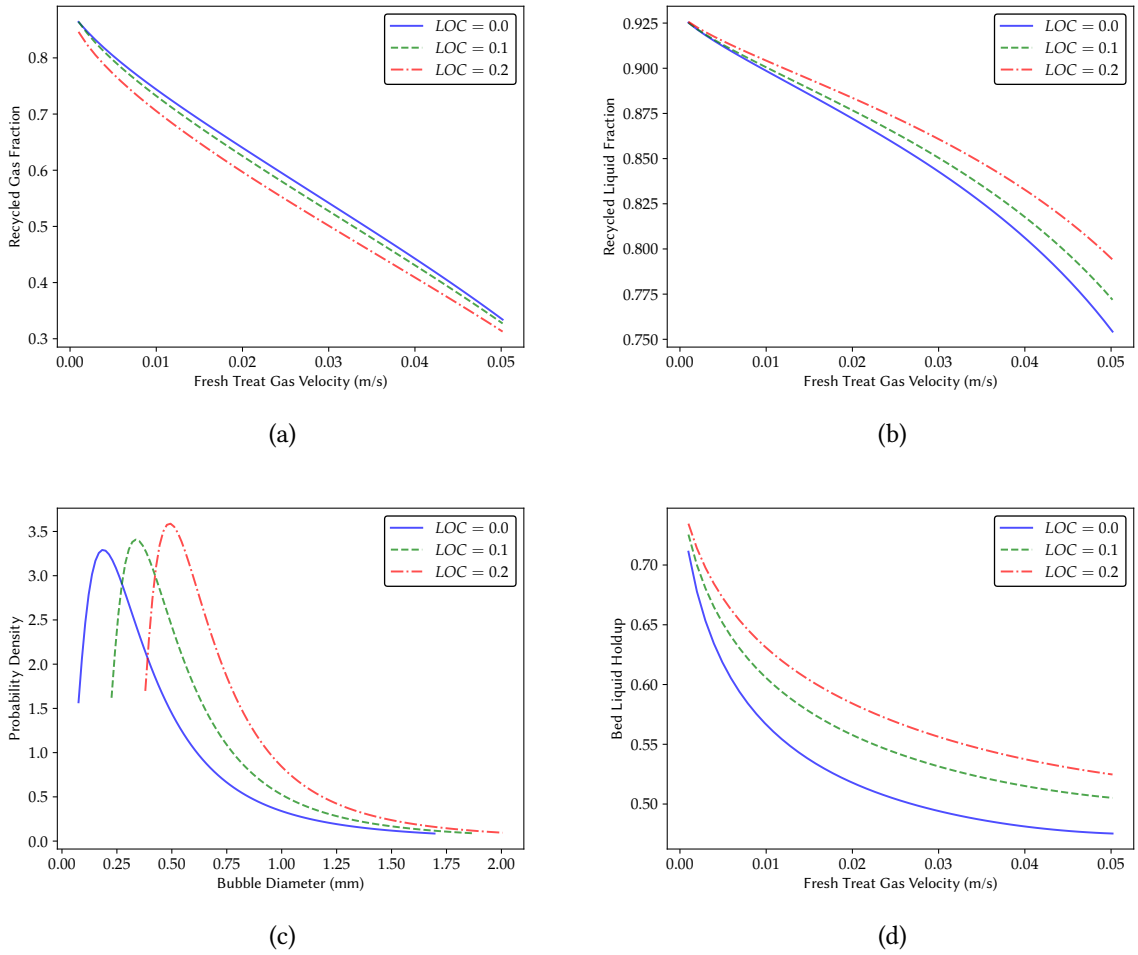

Figure 5.11: Effect of location parameter on (a) recycled gas flow rate, (b) recycled liquid flowrate, (c) bubble size distribution ($q_{g,treat} = 0.40\ m^3/s$) and (d) bed liquid holdup.

Modification of critical grid dimensions such as number and size of outlet orifices without changing the fractional open area might provide another way for increasing bubble sizes. Figure 5.12 shows the effect of increasing the number of outlet orifices (n_{or}) without changing the fractional open area on recycled gas and liquid fractions, bubble size distribution, and bed liquid holdup.

Changing the number of outlet orifices would not require scaling of other critical grid dimensions. However, changing the number of outlet orifices does not significantly increase the bubble sizes and bed liquid holdup due to competing effects of gas and liquid velocities (see eqs 5.3 and 5.4).

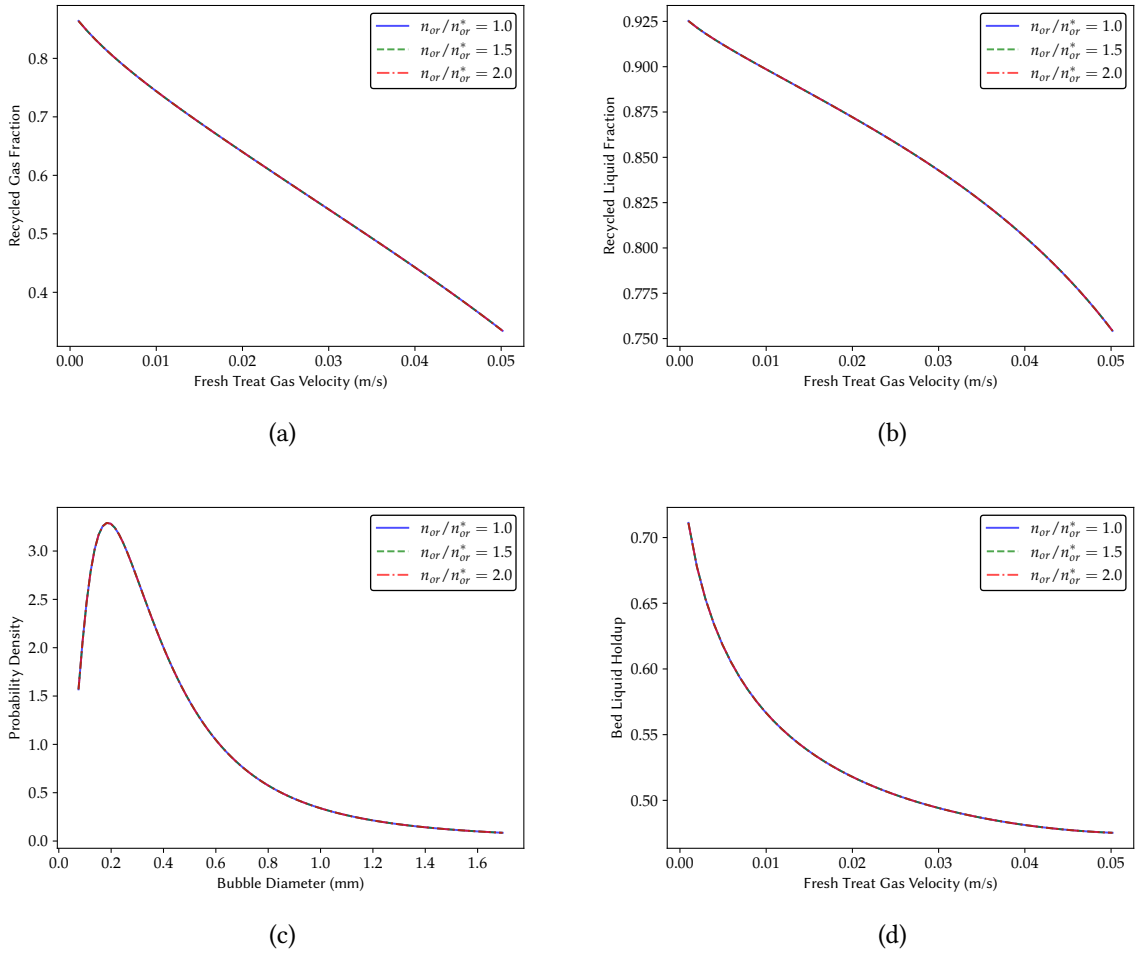

Figure 5.12: Effect of increasing number of outlet orifices on (a) recycled gas flow rate, (b) recycled liquid flowrate, (c) bubble size distribution ($q_{g,treat} = 0.40\ m^3/s$) and (d) bed liquid holdup.

Figure 5.13 shows the effect of outlet orifice diameter (d_{or}) on recycled gas and liquid fractions, bubble size distribution, and bed liquid holdup. Changes in the outlet orifice diameter require scaling of other critical dimensions to produce predicted improvements. The modification of the outlet orifice diameter is quite promising in increasing bubble sizes and bed liquid holdup. Future work will investigate other alternatives such as a complete distributor redesign to further improve

processing capacity of the hydroprocessor. This might require computational fluid dynamics simulations to help identify zones of high power dissipation and/or explore new geometries, with experiments only needed to test the most promising solutions.

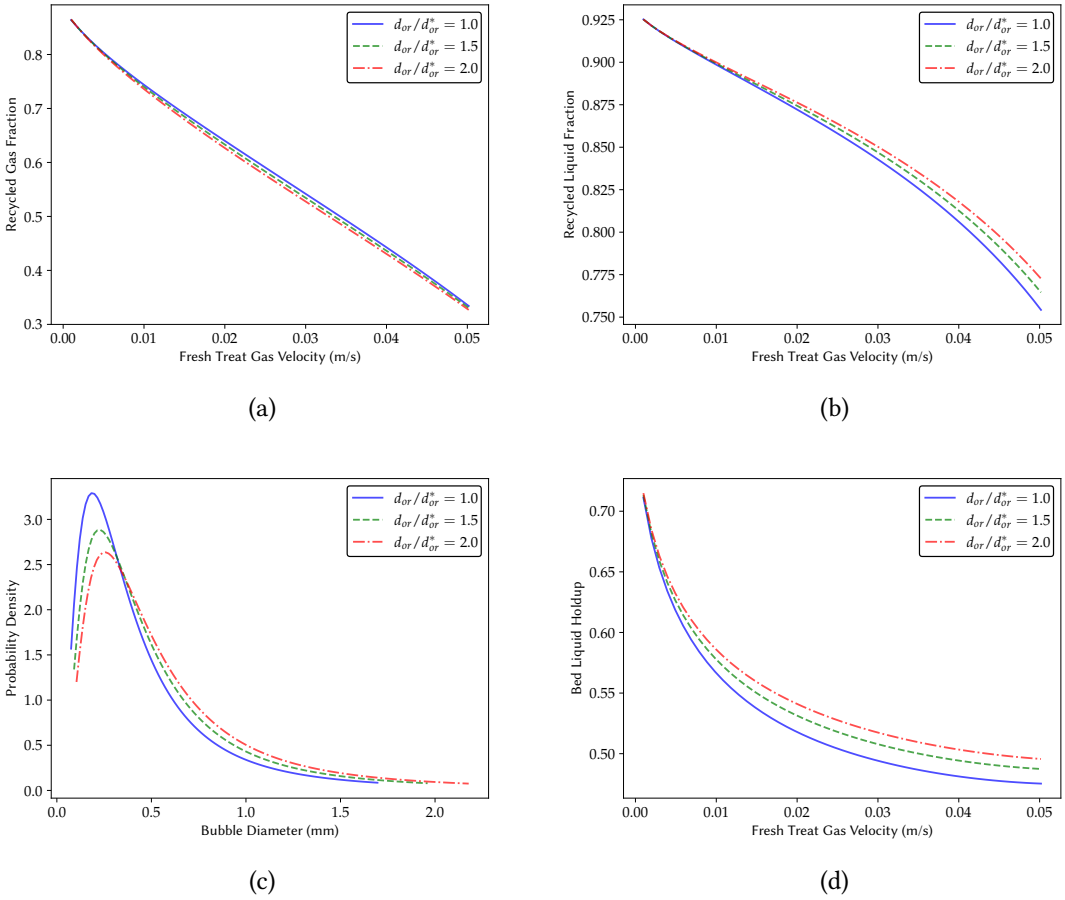

Figure 5.13: Effect of increasing outlet orifice diameter on (a) recycled gas flowrate, (b) recycled liquid flowrate, (c) bubble size distribution ($q_{g,treat} = 0.40\ m^3/s$) and (d) bed liquid holdup.

5.4 CONCLUSIONS

This study incorporates a new gas–liquid distributor model into an overall multiphase fluid dynamics model of a commercial ebullated bed hydroprocessor. New size distribution and drag models are coupled with an existing gas–liquid separation model to better predict recycle flow rates. A numerical framework utilizing fixed catalyst mass as an input to converge the model was implemented to determine the sensitivity of recycled gas and liquid flow rates, bubble size distribution, and bed liquid holdup to treat gas velocity, mass of the catalyst inventory, phase properties, and reactor internals. A 0.2 mm shift in bubble size distribution toward larger sizes was found to significantly improve gas–liquid separation and bed liquid holdup, suggesting that distributor modification/redesign could help improve the performance of the industrial unit. So far, the most promising way to achieve a significant performance improvement via distributor modification is by increasing the diameter of the outlet orifice without changing the fractional open area. Future work will attempt to couple this fluid dynamics model with models for phase equilibria and reaction kinetics to provide a comprehensive tool for optimizing the performance of the hydroprocessor.

ACKNOWLEDGEMENTS

The authors thank Syncrude Canada Ltd., Natural Sciences and Engineering Research Council of Canada (NSERC) and Ontario's Ministry of Colleges and Universities for financial support. The authors are also grateful to Chris D. Lane for his support during the initial stages of this project.

NOMENCLATURE

U_g	Superficial gas velocity, m/s

U_l	Superficial liquid velocity, m/s
ρ_g	Gas density, kgm^{-3}
ρ_l	Liquid density,kgm^{-3}
ρ_s	Solid density, kgm^{-3}
Ar_{L-S}	Liquid-solid Archimedes number
Re_{L-S}	Liquid-solid Reynolds number
Re_l	Liquid Reynolds number
Fr_g	Gas Froude number
μ	Mean of a lognormal random variable, m
$\mu*$	Dimensionless mean of a lognormal random variable
s	Standard deviation of a lognormal random variable
c_{bi}	Individual bubble chord length, m
d_{bi}	Individual bubble diameter, m
U_{lor}	Orifice-based superficial liquid velocity, m/s
U_{gor}	Orifice-based superficial gas velocity, m/s
μ_l	Liquid viscosity, $Pa.s$
g	Gravitational acceleration, m/s^2
E	Bubble aspect ratio
Eo	Eötvös number
σ	Surface tension, N/m
ε_s	Solids holdup, $m^3_{solids}/m^3_{reactor}$
U_{lbed}	Bed superficial liquid velocity, m/s
U_{gbed}	Bed superficial gas velocity, m/s
k	Wall effect parameter
$u_{p\infty}$	Particle terminal velocity, m/s
d_v	Volume-equivalent particle diameter, m
d_{horz}	Length of horizontal axis, m

d_{vert}	Length of vertical axis, m
d_c	Column diameter, m
n	Richardson-Zaki coefficient
$Re_{p\infty}$	Terminal particle Reynolds number
ϕ	Particle sphericity
ε_g	Freeboard gas holdup, $m^3_{bubbles}/m^3_{reactor}$
ε_{gbed}	Bed gas holdup, $m^3_{bubbles}/m^3_{reactor}$
ε_{lbed}	Bed liquid holdup, $m^3_{liquid}/m^3_{reactor}$
m_{cat}	Catalyst mass, kg
ρ_p	Particle density, kgm^{-3}
h_{bed}	Bed height, m
f_1, f_2	Empirical friction factors
$\varepsilon_{g,grid}$	Grid gas holdup, $m^3_{bubbles}/m^3_{reactor}$
$\varepsilon_{l,grid}$	Grid liquid holdup, $m^3_{liquid}/m^3_{reactor}$
ε_l	Freeboard liquid holdup, $m^3_{liquid}/m^3_{reactor}$
$h_{recycle}$	Height of recycle line, m
Re_{mf}	Minimum Reynolds number (Gas-liquid-solid fluidization)
Ar_p	Archimedes number (Gas-liquid-solid)
α_{mf}	Gas holdup at minimum fluidization, $m^3_{bubbles}/m^3_{reactor}$
ε_{mfo}	Void fraction at minimum fluidization (Liquid-Solid), $m^3_{liquid}/m^3_{reactor}$
ε_{mf}	Void fraction at minimum fluidization, $m^3_{liquid}/m^3_{reactor}$
U_{lmfo}	Minimum fluidization velocity (Liquid-solid), m/s
U_{lmf}	Minimum fluidization velocity (Gas-liquid-solid), m/s
Re_{mfo}	Minimum Reynolds number (Liquid-solid fluidization)
$u_{s,i}$	Individual bubble slip velocity, m/s
$\varepsilon_{g,i}$	Individual gas holdup, $m^3_{bubbles}/m^3_{reactor}$
$C^*_{D,i}$	Individual drag coefficient

Re_b	Bubble Reynolds number
p'	Dimensionless pressure
$P(d_{bi})$	Probability of a bubble class in the bed/freeboard regions
$P_{recycle}(d_{bi})$	Probability of entraining a bubble class with the liquid recycle
R	Recycle ratio
$q_{g,treat}$	Fresh treat gas flow rate, m^3/s
$q_{l,vr}$	Fresh bitumen flow rate, m^3/s
q_{gbed}	Bed gas flow rate, m^3/s
q_{lbed}	Bed liquid flow rate, m^3/s
U_{gt}	Fresh treat gas superficial velocity, m/s
n_{or}	Number of outlet orifices per riser
n^*_{or}	Number of outlet orifices per riser (industrial value)
d_{or}	Outlet orifice diameter, m
d^*_{or}	Outlet orifice diameter (industrial value), m
ΔP_{pump}	Pump's head, m
ΔP_{grid}	Grid's pressure drop,Pa
ΔP_{bed}	Bed pressure drop, Pa
$\Delta P_{freeboard}$	Freeboard pressure drop, Pa
ΔP_{pan}	Recycle pan pressure drop, Pa
$\Delta P_{recycle}$	Recycle line pressure drop, Pa
η_i	Separation efficiency of an individual bubble class
η	Overall separation efficiency
B_i	Correction for bubble size and pan design
k'	Liquid residence time in the recycle pan, s

[1] James G Speight. *Heavy and extra-heavy oil upgrading technologies*. Gulf Professional Publishing, 2013. ISBN 0124017479.

[2] Ramakanta Sahu, Byung Jin Song, Ji Sun Im, Young Pyo Jeon, and Chul Wee Lee. A review of recent advances in catalytic hydrocracking of heavy residues. *J. Ind. Eng. Chem.*, 27:12–24, 2015. ISSN 22345957. doi: 10.1016/j.jiec.2015.01.011.

[3] Craig A. McKnight, Larry P. Hackman, John R. Grace, Arturo Macchi, Darwin Kiel, and Jonathan Tyler. Fluid Dynamic Studies in Support of an Industrial Three-Phase Fluidized Bed Hydroprocessor. *Can. J. Chem. Eng.*, 81(3-4):338–350, jun 2008. ISSN 0008-4034. doi: 10.1002/cjce.5450810302.

[4] Dominic Pjontek, Craig A. McKnight, Jason Wiens, and Arturo Macchi. Ebullated bed fluid dynamics relevant to industrial hydroprocessing. *Chem. Eng. Sci.*, 126:730–744, 2015. ISSN 00092509. doi: 10.1016/j.ces.2015.01.002.

[5] Peter M. Wilkinson, Arie P. Spek, and Laurent L. van Dierendonck. Design parameters estimation for scale-up of high-pressure bubble columns. *AIChE J.*, 38(4):544–554, 1992. ISSN 15475905. doi: 10.1002/aic.690380408.

[6] R. S. Ruiz, F. Alonso, and J. Ancheyta. Effect of high pressure operation on overall phase holdups in ebullated-bed reactors. *Catal. Today*, 98(1-2 SPEC. ISS.):265–271, 2004. ISSN 09205861. doi: 10.1016/j.cattod.2004.07.039.

[7] R. S. Ruiz, F. Alonso, and J. Ancheyta. Pressure and temperature effects on the hydrodynamic characteristics of ebullated-bed systems. *Catal. Today*, 109(1-4):205–213, 2005. ISSN 09205861. doi: 10.1016/j.cattod.2005.08.019.

[8] Veniamin G Levich. *Physiochemical Hydrodynamics*. Prentice Hall, Engelwood Cliffs, NJ, 1962.

[9] K. Malysa, M. Krasowska, and M. Krzan. Influence of surface active substances on bubble motion and collision with various interfaces. *Adv. Colloid Interface Sci.*, 114-115:205–225, 2005. ISSN 00018686. doi: 10.1016/j.cis.2004.08.004.

[10] Dominic Pjontek, Valois Parisien, and Arturo Macchi. Bubble characteristics measured using a monofibre optical probe in a bubble column and freeboard region under high gas holdup conditions. *Chem. Eng. Sci.*, 111:153–169, 2014. ISSN 00092509. doi: 10.1016/j.ces.2014.02.024.

[11] Mike Safoniuk, John R. Grace, Larry Hackman, and Craig A. McKnight. Use of dimensional similitude for scale-up of hydrodynamics in three-phase fluidized beds. *Chem. Eng. Sci.*, 54 (21):4961–4966, 1999. ISSN 00092509. doi: 10.1016/S0009-2509(99)00218-3.

[12] Arturo Macchi, Hsiaotao Bi, John R. Grace, Craig A. McKnight, and Larry Hackman. Dimensional hydrodynamic similitude in three-phase fluidized beds. *Chem. Eng. Sci.*, 56(21-22): 6039–6045, 2001. ISSN 00092509. doi: 10.1016/S0009-2509(01)00207-X.

[13] Arturo Macchi, Hsiaotao Bi, John R. Grace, Craig A. McKnight, and Larry Hackman. Effect of Gas Density on the Hydrodynamics of Bubble Columns and Three-Phase Fluidized Beds. *Can. J. Chem. Eng.*, 81(3-4):846–852, jun 2008. ISSN 0008-4034. doi: 10.1002/cjce.5450810368.

[14] C. D. Lane, C. A. McKnight, J. Wiens, K. Reid, and A. A. Donaldson. Parametric analysis of internal gas separation within an ebullated bed reactor. *Chem. Eng. Res. Des.*, 105:44–54, 2016. ISSN 02638762. doi: 10.1016/j.cherd.2015.10.043.

[15] Chris D. Lane, Arturo Macchi, Craig A. Mcknight, Jason Wiens, and Adam A. Donaldson. Internal Gas-Liquid Separation in Industrial Ebullated Bed Hydroprocessors. *Ind. Eng. Chem. Res.*, 58(40), 2019. ISSN 15205045. doi: 10.1021/acs.iecr.9b02201.

[16] Chris D. Lane, Arturo Macchi, Dominic Pjontek, Craig A. McKnight, Jason Wiens, and Adam A. Donaldson. Modeling the Fluid Dynamics of a Commercial Ebullated Bed Hydroprocessor. *Ind. Eng. Chem. Res.*, 58(39):18387–18396, 2019. ISSN 15205045. doi: 10.1021/acs.iecr.9b02779.

[17] Richard M. Eccles. Residue hydroprocessing using ebullated-bed reactors. *Fuel Process. Technol.*, 35(1-2):21–38, 1993. ISSN 03783820. doi: 10.1016/0378-3820(93)90083-G.

[18] Jean Marc Schweitzer and Stéphane Kressmann. Ebullated bed reactor modeling for residue conversion. *Chem. Eng. Sci.*, 59(22-23):5637–5645, 2004. ISSN 00092509. doi: 10.1016/j.ces.2004.08.018.

[19] Eduard Manek and Juma Haydary. Investigation of the liquid recycle in the reactor cascade of an industrial scale ebullated bed hydrocracking unit. *Chinese J. Chem. Eng.*, 27(2):298–304, 2019. ISSN 10049541. doi: 10.1016/j.cjche.2018.06.023.

[20] Jacob Mach, Valois Parisien, Jason Wiens, Craig A. McKnight, and Arturo Macchi. Impact of plenum conditions and gas-liquid distributor on bubble column hydrodynamics. *Chem. Eng. Sci.*, 211:115296, 2020. ISSN 00092509. doi: 10.1016/j.ces.2019.115296.

[21] Jacob Mach, Jason Wiens, John Adjaye, and Arturo Macchi. Fluid Dynamics Scaling of a Gas–Liquid Distributor Applied to a Commercial Ebullated Bed Hydroprocessor. *Ind. Eng. Chem. Res.*, 59(44):19712 – 19725, 2020.

[22] Jacob Mach, Jason Wiens, John Adjaye, Adam A. Donaldson, and Arturo Macchi. Effect of pressure on the drag coefficient of individual bubbles in a contaminated polydisperse swarm. *Chem. Eng. Sci.*, 223:115728, 2020. ISSN 00092509. doi: 10.1016/j.ces.2020.115728.

[23] Alsarkhi Abdelsalam, Sarica Cem, and Pereyra Eduardo. New dimensionless number for gas-liquid flow in pipes. *Int. J. Multiph. Flow*, 81:15–19, 2016. ISSN 03019322. doi: 10.1016/j.ijmultiphaseflow.2015.12.008.

[24] E. Camarasa, C. Vial, S. Poncin, G. Wild, N. Midoux, and J. Bouillard. Influence of coalescence behaviour of the liquid and of gas sparging on hydrodynamics and bubble characteristics in a bubble column. *Chem. Eng. Process. Process Intensif.*, 38(4-6):329–344, 1999. ISSN 02552701. doi: 10.1016/S0255-2701(99)00024-0.

[25] M. Simonnet, C. Gentric, E. Olmos, and N. Midoux. Experimental determination of the drag coefficient in a swarm of bubbles. *Chem. Eng. Sci.*, 62(3):858–866, 2007. ISSN 00092509. doi: 10.1016/j.ces.2006.10.012.

[26] R. M. Wellek, A. K. Agrawal, and A. H.P. Skelland. Shape of liquid drops moving in liquid media. *AIChE J.*, 12(5):854–862, 1966. ISSN 15475905. doi: 10.1002/aic.690120506.

[27] J. P. Zhang, N. Epstein, and J. R. Grace. Minimum fluidization velocities for gas-liquid-solid three-phase systems. *Powder Technol.*, 100(2-3):113–118, 1998. ISSN 00325910. doi: 10.1016/S0032-5910(98)00131-4.

[28] Donghyun Lee, Norman Epstein, and John R. Grace. The variable-voidage effect on modeling the minimum liquid fluidization velocity of gas-liquid fluidized beds. *J. Chem. Eng. Japan*, 36 (9):1111–1115, 2003. ISSN 00219592. doi: 10.1252/jcej.36.1111.

[29] Ari Hamdani, Tomonori Ihara, Nobuyoshi Tsuzuki, and Hiroshige Kikura. Experimental study of bubbly swirling flow in a vertical tube using ultrasonic velocity profiler (UVP) and wire mesh sensor (WMS). *J. Mech. Sci. Technol.*, 30(9):3897–3905, 2016. ISSN 1738494X. doi: 10.1007/s12206-016-0801-6.

[30] Ting Yee Chan and James Harvey Colvert. Liquid degaser in an ebullated bed process, 1989.

6

CONCLUSIONS AND RECOMMENDATIONS FOR FUTURE WORK

6.1 CONCLUSIONS

The performance of industrial ebullated bed hydroprocessors is dependent on the fluids distribution system and internal liquid recycle pan. A uniform distribution of the fluids into the bed is essential for proper hydrogenation and prevents the formation of mesophase and coke, which can deposit on the distributor, and further hinder the distribution. Given that bubbles do not readily coalesce in the bed, the original bubble size distribution produced at the distributor impacts gas-liquid separation at the recycle pan. Excessive gas entrainment in the liquid recycle is a major challenge to reactor performance, as entrained gas increases bed gas holdups at the expense of liquid holdup and product yield. The aim of this project was to investigate the impact of gas-liquid distribution system on resulting bubble properties and dynamics at industrially relevant conditions and incorporate a distributor sub-model into the overall fluid dynamics model of the industrial unit.

Initial study investigated the interactions between plenum conditions and gas-liquid distributor at ambient pressure and temperature. Plenum conditions tested had negligible impact on resulting bubble properties. However, the resulting mean bubble sizes correlated well with distributor power dissipation and gas-liquid velocity ratio to the power of -0.4 and 0.6, respectively, in agreement with theory on the turbulent breakup of bubbles in dense dispersions. The bubble sizes were found to also depend on distributor geometry, where bubble cap distributor produced larger bubbles than perforated plate distributor. The effect of distributor geometry was attributed to possible bubble

re-coalescence in lower power dissipation zones of the distributor.

Although it is possible to scale a gas-liquid distributor via power dissipation and gas-liquid velocity ratio, it requires prior knowledge of local distributor pressure drops and fluids residence times through the distributor, which can be challenging to acccurately predict. In a follow up work, an alternate scaling approach, using dimensional analysis and similitude for which fluids velocities and physical properties can be known beforehand, was proposed. Geometric scaling was based on matching distributor fractional open area and ratios of various critical dimensions. Dynamic similarity was based on matching three dimensionless groups (gas-liquid density ratio, liquid Reynolds number and gas Froude number) and bubble coalescence behaviour. Two geometrically similar distributors with one and three smaller bubble caps were used to experimentally evaluate the scaling approach. A good agreement between resulting bubble size distributions was found for the two distributors, suggesting that the scaling approach works. Resulting bubble size distributions were then correlated to the dimensionless groups to enable the estimation of bubble size distributions at industrial conditions.

Fluid dynamics modeling of commercial ebullated bed hydroprocessor relies on drag models to predict bubble rise velocities and resulting phase holdups. Although there are numerous drag models in literature, there were few that investigated the effect of pressure on the drag coefficient of individual bubbles in a contaminated poydisperse swarm. This effect was recently investigated and quantified by the author, who found individual bubble drag coefficients to decrease with pressure at constant gas holdup. This effect was attributed to bubble size distributions, which shifted towards smaller sizes with increasing pressure. These smaller bubbles induce lower liquid phase perturbations and could potentially dampen existing turbulence, leading to reduced drag. A novel drag coefficient model was proposed to incorporate the effect of pressure.

A gas-liquid distributor sub-model, including bubble size distribution and drag models previously developed, was incorporated into an overall multiphase fluid dynamics model of the ebullated bed hydroprocessor. The bubble size distribution model was also coupled with existing gas-liquid separation sub-model to better predict recycled gas and liquid fractions. The overall model was used to study the sensitivity of recycle gas flow rate, recycle liquid flow rate, bubble size distribution and bed liquid holdup to changes in fresh treat gas flow rate, catalyst mass, phase physical properties and reactor internals. To simulate the effect of an improved gas-liquid distributor, the bubble size distribution was positively shifted by 0.2 mm. This shift significantly improved the gas-liquid separation efficiency and increased bed liquid holdup, suggesting that distributor modification/redesign could help improve the performance of the industrial unit. Both number and diameter of outlet orifices on the bubble cap riser were also modified numerically, without changing the distributor fractional open area, to determine their impact on separation efficiency and bed liquid holdup. The number of outlet orifices was found to have negligible impact on both separation efficiency and bed liquid holdup. However, an increase in outlet orifice diameter resulted in higher separation efficiency and bed liquid holdup.

One of the main outcomes of this work is the fluid dynamic simulator, which can be a tool for determining the impact of changes in operating conditions before they are implemented. For instance, the hydrocracking catalyst is replenished regularly to maintain catalytic activity. The impact of geometrical changes (e.g., shape and size) to the hydrocracking catalyst on reactor fluid dynamics can thus be investigated using the simulator before the new catalyst is introduced into the reactor. Moreover, once the reaction and interphase transport models have been explicitly re-coupled with the fluid dynamics, the resulting simulator could serve as a tool for designing new efficient hydroprocessors. Although the work was motivated by challenges encountered in operating commercial ebullated bed hydroprocessors, the results and conclusions drawn are also directly applicable to the design, operation and modelling of bubble columns.

The assumptions and limitations of this work were discussed in prior chapters. However, one assumption that has not been explicitly mentioned is the treatment of bitumen residue as a Newtonian fluid. Bazyleva et al. [1] studied the rheological properties of Athabasca bitumen at various temperatures. They found that Athabasca bitumen behaves as a solid up to a temperature of 260 – 280 K, as a non-Newtonian shear-thinning fluid up to a temperature of 310 – 315 K and as a Newtonian fluid at higher temperatures. Since the industrial unit is operated at much higher temperatures ($\sim$ 713 K), the bitumen can be considered as a Newtonian fluid.

6.2 FUTURE WORK

Drag coefficient models for dense bubbly flows often encountered in industrial applications are extended from single bubble drag models using a swarm correction factor. One of the factors affecting the swarm correction factor is gas holdup. Ideally, local gas holdup is needed to correlate experimentally determined drag coefficients. As the optical probe could not close the mass balance in a liquid contaminated with surface active compound, the new drag coefficient model was based on global gas holdups measured with differential pressure transducer, which is a more reliable technique. With an improved optical probe capable of closing mass balance, it may be worthwhile to determine if the swarm correction factor is also dependent on radial position. Alternatively, the current optical probe may be used to determine the dependence of swarm correction factor on radial position in tap water, where there is lower uncertainty in probe-measured local gas holdup.

Due to the lack of reliable bubble size estimates, previous fluid dynamics models of ebullated bed hydroprocessors manipulated the mean bubble size to match commercial operating data for freeboard gas holdup and recycle pan efficiency. This approach resulted in models that are suitable for the particular operating conditions and reactor geometries, but that are not extensible to other operating conditions and geometries. Furthermore, these models implicitly accounted for reaction

kinetics and phase equilibria. To rectify this, the author proposed a distributor sub-model capable of predicting resulting bubble size distributions based on fluids velocities, phase properties, and distributor geometrical parameters. The new distributor sub-model was incorporated into the overall fluid dynamics model, enabling the decoupling of reaction kinetics and phase equilibria. Future work could thus look into explicitly re-coupling the fluid dynamics model with reaction kinetics and interphase mass transport models to provide a comprehensive reactor model for design, training, and simulating the effects of changes in operating conditions. It is worth noting that vaporization of lighter hydrocarbons, which has been shown to significantly influence fluid dynamics, may be one of the greatest challenges in such an exercise. It is not clear if vaporized hydrocarbons form independent bubbles, due to nucleation events, or if they only increase the size of existing bubbles in ratios proportional to individual bubble surface areas.

A sensitivity analysis performed with the fluid dynamics model revealed that increasing the size of outlet orifices, without changing distributor fractional open area, could help increase bed liquid holdup and product yield. Future work could explore other means through which bubbles sizes and rise velocities can be simultaneously increased. The use of multiphase computational fluid dynamics to do exploratory studies may be worthwhile to identify candidate distributor designs, which can then be tested experimentally.

REFERENCES

[1] Ala B. Bazyleva, MD. Anwarul Hasan, Michal Fulem, Mildred Becerra, and John M. Shaw. Bitumen and heavy oil rheological properties: Reconciliation with viscosity measurements. *Journal of Chemical & Engineering Data*, 55(3):1389–1397, 2010. doi: 10.1021/je900562u.